Benchmark simulations of underwater explosion gas bubble dynamics and interactions

Malcolm J. Smith
DRDC – Atlantic Research Centre

Defence Research and Development Canada

Abstract

The results of a series of benchmark simulations in one, two and three dimensions are presented to illustrate the capabilities of the Eulerian blast code Chinook (version 195) in simplified underwater explosion (UNDEX) scenarios. Attention in this study is focussed on the behaviour of the underwater explosion gas bubble. 2D and 3D simulation results for a 1.1 g charge detonated in the free field agree well with empirical formulas for gas bubble radius and period for the first bubble pulse, whereas 1D simulation results fall short of the expected accuracy. Results for UNDEX near a free surface also agree well with empirical formulas in 2D and 3D, and realistic gas bubble jetting behaviour is predicted. Fluid-structure interaction simulations with a circular-plate target structure were simulated using Chinook coupled with the finite element program LS-Dyna. The predicted gas bubble behaviour is realistic for rigid target models, but unrealistic when the target plate is flexible. Of the two different coupling schemes used, Chinook's small deformation coupling scheme was more reliable; the large deformation coupling scheme worked consistently with rigid target models in 2D, but is prone to numerical problems in 3D.

Significance to defence and security

Simulation of underwater explosions and their effect on target structures is an important tool for improving the survivability of naval platforms to underwater weapons. The present work is part of a long-term effort by DRDC to validate the Chinook and LS-Dyna software tools for predicting the response and damage of naval platforms in close-proximity underwater explosion scenarios.

Résumé

On présente les résultats d'une série de simulations de référence unidimensionnelles (1D), bidimensionnelles (2D) et tridimensionnelles (3D) afin d'illustrer les capacités du logiciel eulérien Chinook pour la simulation d'explosions (version 195) dans des scénarios simplifiés d'explosions sous-marines (UNDEX). Dans la présente étude, on accorde une attention particulière au comportement de la bulle de gaz créée par une explosion sous-marine. Les résultats des simulations 2D et 3D pour une charge de 1,1 g qui explose en champ libre concordent avec les formules empiriques pour le rayon de la bulle de gaz et la période de la première impulsion de la bulle. Les résultats des simulations 1D sont toutefois inférieurs à l'exactitude prévue. Les résultats des UNDEX près d'une surface libre concordent également avec les formules empiriques en 2D et 3D, ce qui permet de prévoir le comportement réaliste de jets de bulles de gaz. Pour les simulations d'interaction fluide-structure à l'aide d'une structure cible, laquelle consiste en une plaque circulaire, le logiciel Chinook a été utilisé et jumelé au programme de calcul par éléments finis LS-Dyna. Le comportement prévu des bulles de gaz est réaliste pour les modèles de cibles rigides, mais irréaliste quand la plaque cible est flexible. De ces deux méthodes, le couplage des déformations légères de Chinook a offert la plus grande fiabilité; le couplage des déformations importantes a fonctionné de façon constante avec les modèles de cibles rigides en 2D, mais avait tendance à éprouver des problèmes numériques en 3D.

Importance pour la défense et la sécurité

La simulation d'explosions sous-marines et de leurs effets sur les structures cibles constitue un outil important pour améliorer la surviabilité des plates-formes navales lorsque des armes sous-marines sont utilisées. La présente étude fait partie d'un effort à long terme déployé par RDDC afin de valider l'utilisation des logiciels Chinook et LS-Dyna pour prévoir la réaction des plates-formes navales et les dommages subis dans des scénarios d'explosions sous-marines proches.

Table of contents

List of figures

List of tables

This page intentionally left blank.

1 Introduction

Underwater explosions that are in close proximity to a hull structure are of interest in the study of both the vulnerability of naval platforms and the lethality of underwater munitions. The physical processes are quite complex, and broadly consist of (1) a shock wave that propagates through the water and interacts with the structure; (2) rarefaction waves generated by reflection of the shock at free and responding surfaces, creating regions of cavitation in the surrounding water; (3) a gas bubble containing the explosion products which goes through cycles of expansion and contraction, generating acoustic pulses at the minima; (4) a high velocity water jet formed as a spheroidal gas bubble collapses to a toroidal shape. All of these processes contribute to the damage inflicted on a naval platform. Many modern examples naval vessels damaged by sea mines are described by Webster [1]. The damage to the South Korean patrol vessel ROKS Cheonan inflicted by a torpedo is described in detail by Yoon et al [2].

Simulation of all of the physical processes and the resulting damage is a complex undertaking. Compressible hydrodynamics methods are generally required for the shock wave and acoustic pulse and their interactions with the structure and the surrounding fluid. These processes are rapid, and typically require numerical simulations with small grid cells and small time steps. The expansion and contraction of the gas bubble is a comparatively slow process, except near the minima of the bubble radius, when the surface of the bubble moves very rapidly. Compressible hydrodynamic methods offer the most general utility for simulating the full range of loading and response processes. Since Mader [3] first used a particle-in-cell method to simulate bubble collapse in 2D, coupled Eulerian-Lagrangian (CEL) and arbitrary Lagrangian Eulerian (ALE) methods [4] have become the preferred methods for gas bubble simulations involving fluid-structure interaction. A number of researchers have had success with modelling the interactions of a gas bubble with a nearby structure using incompressible hydrodynamic methods, originally applied by Blake et al [5] to transient cavities and by Best [6] to explosion bubbles. However, incompressible methods are inherently unable to assess the combined damage effects from the shock and the gas bubble, which is of interest in most military applications.

Defence Research and Development Canada (DRDC) has invested considerable effort in the simulation of close-proximity underwater explosion (UNDEX) effects on naval platforms, as part of its collaboration under a Project Arrangement under the Canada/Netherlands/Sweden Memorandum of Understanding (MOU). Central to this work is the accurate prediction of the loading on and response of targets in small-scale experiments. DRDC uses the Eulerian blast code Chinook, developed by the Applied Technology group of Lloyd's Register (formerly Martec Limited), and LS-Dyna, a commercial finite element analysis (FEA) code developed by Livermore Software Technology Corporation, for its close-proximity UNDEX simulations. These two codes, when run in coupled mode, provide a CEL solution method in which the Eulerian code Chinook computes the blast pressures and associated fluid motions, and the Lagrangian code LS-Dyna computes the target response.

The coupled Chinook/LS-Dyna method has been used in recent years to simulate UNDEX experiments involving both submerged, and floating targets [7]–[14]. The main focus of these simulations has been predicting the response of the target and the behavior of the explosion gas bubble. These simulations have shown a number of inconsistencies with what is observed in the experiments, especially in the loading and the behaviour of the gas bubble. For example, in

simulations of floating box experiments [15], the gas bubble predicted for 1.1 g nitroamine (RDX) detonator charges had a significantly smaller radius and period than what was observed in experiments. Bubble collapse and jetting behaviour often differed from the experiments, as well. Better agreement with experiment has been achieved in a recent study of the same floating box experiments, however [16].

Because of the earlier inconsistencies, a series of benchmark test problems were created for testing the function of Chinook and LS-Dyna in simplified UNDEX scenarios. These simulations allow basic characteristics of the explosion gas bubble, like radius and period, to be compared with empirical or measured values. This allows the adequacy of grids used with Chinook to be evaluated in 1D, 2D and 3D, as well as the effectiveness of mapping field variables from 1D to 3D grids, or 2D to 3D grids to increase accuracy and reduce computations. Included in these benchmarks are simulations involving UNDEX in close-proximity to a simple axisymmetric target plate with varying levels of rigidity and restraint applied to the model.

For all the simulations, Chinook Version 195 [17] and LS-Dyna Version 971 (single precision) [18] were used. Chinook simulations were typically run in parallel mode with 30 processors. Most of the simulations were run on a Dell Precision T7600 workstation running 64-bit Windows 7 or on an IBM 80-core shared-memory server running CentOS 6.2.

The objectives of the present work are to (1) determine grid cell sizes needed to give accurate radius and period data for the explosion gas bubble; (2) identify modelling deficiencies in Chinook through comparison of results over a range of similar problems with identical material and modelling parameters; and (3) to establish a series of standard problems for benchmarking future versions of Chinook.

The organization of the report is as follows. Section 2 provides an overview of the theory of explosion gas bubbles. Section 3 describes the 1D benchmark simulations. Section 4 describes all of the 2D simulations; including free-field, free surface and fluid-structure interaction (FSI) simulations. Section 5 describes all of the 3D simulations including free-field, free surface and FSI cases. A discussion of the results and of the strengths and weaknesses of the software is given in Section 6. Final conclusions and recommendations are provided in Section 7.

2　Theory of explosion gas bubbles

The products of an underwater explosion initially remain trapped in a gas bubble, unless the explosion occurs so close to the surface that the explosion products are immediately vented to the atmosphere. The initial high pressure of the explosion products causes the bubble to expand and displace the surrounding water. As the bubble expands, the pressure inside the bubble drops and eventually falls below the ambient pressure in the water due to the inertia generated in the surrounding water. In the free field, away from the free surface, seabed, and solid objects, the maximum radius attained by the nearly spherical bubble during the first pulse, A_1^*, is given by the similitude formula [19]:

$$A_1^* = K_6 \frac{W^{1/3}}{Z_1^{1/3}} \tag{1}$$

where W is the charge mass; $Z_1 = 10.1 + d_1$ is the hydrostatic pressure head in metres of the bubble at maximum expansion; d_1 is the depth of the bubble in metres at maximum expansion; and K_6 is an empirical constant. An asterisk (*) is used to distinguish empirical quantities from the numerical predictions of the same quantities presented in the following sections of this report.

Once maximum expansion is reached, the bubble begins to collapse during which time its shape may become less spherical, due to instabilities in the contracting bubble surface [20]. At minimum extent, the bubble may have a highly distorted shape. At this time it radiates an impulsive pressure wave to the surrounding fluid with an associated loss of energy from the bubble. For bubbles in the free field, this occurs at time

$$T_1^* = K_5 \frac{W^{1/3}}{Z_1^{5/6}} \tag{2}$$

where K_5 is an empirical constant [19]. For gas bubbles near the free surface, a correction to the bubble period is necessary. Snay [21] gives the following formula for the nth bubble period:

$$T_n^* = 0.374\,\tau \frac{(r_n Q W)^{1/3}}{Z_n^{5/6}} \left(1 - \alpha \frac{A_n^*}{d_n}\right) \tag{3}$$

where τ is a dimensionless reduced period; r_n is the fraction of energy retained in the bubble during the nth pulse; Q is the energy per unit mass of the explosive; Z_n is the hydrostatic pressure head for the nth pulse; A_n^* is the maximum bubble radius in the nth pulse; d_n is the depth of the nth bubble pulse; and α is a surface correction factor. Snay gives a value of α of 0.2.

Adapting Snay's equation for T_1^* using (1) and (2) gives the following form, in which K_5 is used in place of $0.374\,\tau(r_1 Q)^{1/3}$:

$$T_1^* = K_5 \frac{W^{1/3}}{Z_1^{5/6}} \left(1 - \alpha \frac{A_1^*}{d_1}\right) \tag{4}$$

The empirical formula for bubble radius (1) does not require a surface correction. Where multiple bubble pulses are generated by a single UNDEX event, the maximum radius of each successive pulse is given by Snay as

$$A_n^* = 1.733 \, a_m \frac{(r_n QW)^{1/3}}{Z_n^{1/3}} \tag{5}$$

where a_m is a dimensionless reduced maximum radius and the other terms are the same as for (3). Comparing this equation with (1) gives

$$K_6 = 1.733 \, a_m (r_1 Q)^{1/3} \tag{6}$$

With this result, (5) can be rewritten to express the bubble radii of successive pulses in terms of the energy ratio r_n/r_1:

$$A_n^* = K_6 \left(\frac{r_n}{r_1}\right)^{1/3} \frac{W^{1/3}}{Z_n^{1/3}} \tag{7}$$

Using (3), the ratio of the nth to the first bubble period can be derived as [20]

$$\frac{T_n^*}{T_1^*} = \left(\frac{r_n}{r_1}\right)^{1/3} \left(\frac{Z_1}{Z_n}\right)^{5/6} \frac{\left(1 - \alpha \frac{A_n^*}{d_n}\right)}{\left(1 - \alpha \frac{A_1^*}{d_1}\right)} \tag{8}$$

Similarly, using (5) or (7), the ratio of the nth to the first bubble radius can be derived as

$$\frac{A_n^*}{A_1^*} = \left(\frac{r_n}{r_1}\right)^{1/3} \left(\frac{Z_1}{Z_n}\right)^{1/3} \tag{9}$$

These formulas take into account energy losses due to the bubble pulse and other dissipation mechanisms, r_n, the effect of bubble migration, Z_n, and the surface effect, α. Theoretical values for the energy ratios determined by Snay [21] are $r_2/r_1 = 0.35$ and $r_3/r_1 = 0.185$ for a non-migrating free-field bubble.

The simulations undertaken in this study all involve 1.1 g RDX detonator charges, for which the values of the empirical constants are $K_5 = 2.232$ and $K_6 = 3.740$ in SI units, based on unpublished data obtained from Naval Surface Warfare Center Carderock Division. Table 1 summarizes empirical values calculated with the above formulas for the first three bubble pulses. Results are given for the "free field" case in which surface effects are neglected, and the "free surface" case, in which the surface correction factor is included.

Table 1: Empirical values for bubble radii and periods.

	Free field	Free surface
Bubble depth (m)	0.0	0.3
A_1^* (m)	0.179	0.177
A_2^* (m)	0.126	0.125
A_3^* (m)	0.102	0.101
T_1^* (ms)	33.7	28.7
T_2^* (ms)	23.7	21.2
T_3^* (ms)	19.2	17.5

3　1D benchmark cases

3.1　Grids

The objective of the 1D benchmark simulations is to determine the grid cell size and modelling parameters needed for one-dimensional simulations of underwater explosion gas bubble pulsation. One-dimensional models are created using Chinook's internal grid generation capability (keyword *GRID_INTERNAL) in which the one-dimensional geometry is represented with a two-dimensional grid with a single cell in the second dimension. Spherical symmetry is imposed in Chinook by setting the "geom" parameter to 3. The generic geometry is shown in Figure 1, where the grid is comprised of a regular grid and an extended grid. The regular grid has a uniform cell size given by $\Delta X_R = X_R/N$, where X_R is the length of the regular grid, and N is the number of cells. The cell size in the extended grid is governed by an expansion factor ξ, such that

$$(\Delta X_E)_i = (1 + \xi)(\Delta X_E)_{i-1}, \qquad i = 1, 2, \ldots N_E \tag{10}$$

and where $(\Delta X_E)_0 = \Delta X_R$. The size of the ith cell in the extended grid is therefore determined by the geometric progression

$$(\Delta X_E)_i = (1 + \xi)^i \Delta X_R, \tag{11}$$

and the total length of the extended grid is given by the summation

$$X_E = \Delta X_R \sum_i (1 + \xi)^i = \Delta X_R \frac{(1 + \xi)^{N_E} - 1}{\xi} \tag{12}$$

The 1D grids are therefore completely determined by defining the four parameters: X_R, N, ξ, N_E.
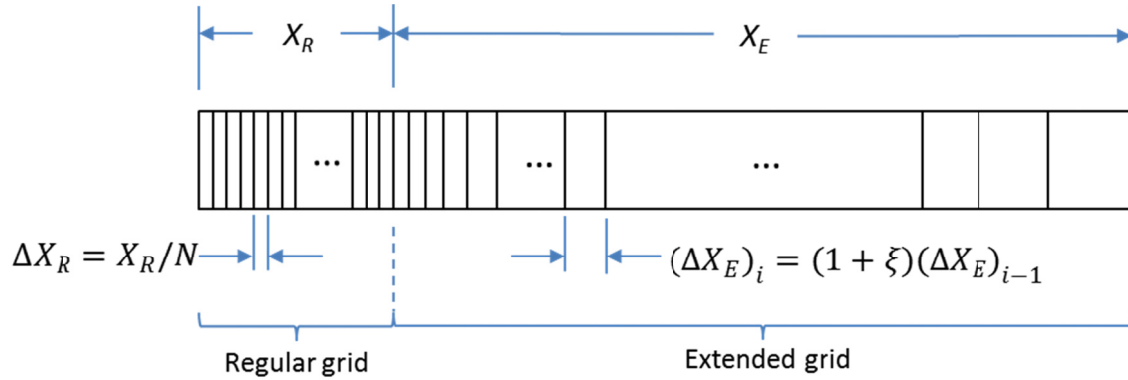
Figure 1: One dimensional grid geometry.

The 1D grids used in this benchmark investigation are listed in Table 2. These grids are intended for determining the gas bubble properties of a 1.1 g RDX detonator charge centred at $X = 0$. Each grid series consists of seven grids with a fixed regular grid cell size and variable mesh expansion factor ξ. The size of the regular domain has been fixed at $X_R = 0.25$ m in all grid series. The total

grid size $X_R + X_E$ is approximately 100 m for grid series 1, 2 and 3, and about 30 m for grid series 4. The total grid size was selected so that reflections from the end of the grid will not influence the bubble behaviour in the time duration of interest. The overall grid dimension was reduced for grid series 4 to reduce the number of grid cells.

Table 2: 1D benchmark grids for 1.1 g RDX detonator.

Grid	Regular grid			Extended grid			Total grid	
	X_R (m)	N	Cell size ΔX_R (mm)	ξ	N_E	X_E	$X_R + X_E$	$N+N_E$
1a	0.25	1250	0.2	0.1	113	104.66	104.91	1363
1b	0.25	1250	0.2	0.05	207	102.19	102.44	1457
1c	0.25	1250	0.2	0.02	465	101.77	102.02	1715
1d	0.25	1250	0.2	0.01	860	100.01	100.26	2110
1e	0.25	1250	0.2	0.005	1569	100.60	100.85	2819
1f	0.25	1250	0.2	0.002	3460	100.64	100.89	4710
1g	0.25	1250	0.2	0.001	6220	100.13	100.38	7470
2a	0.25	2500	0.1	0.1	120	101.98	102.23	2620
2b	0.25	2500	0.1	0.05	221	101.17	101.42	2721
2c	0.25	2500	0.1	0.02	500	101.77	102.02	3000
2d	0.25	2500	0.1	0.01	925	100.36	100.61	3425
2e	0.25	2500	0.1	0.005	1707	100.13	100.38	4207
2f	0.25	2500	0.1	0.002	3805	100.30	100.55	6305
2g	0.25	2500	0.1	0.001	6915	100.38	100.63	9415
3a	0.25	5000	0.05	0.1	128	109.30	109.55	5128
3b	0.25	5000	0.05	0.05	235	100.15	100.40	5235
3c	0.25	5000	0.05	0.02	535	101.77	102.02	5535
3d	0.25	5000	0.05	0.01	995	100.70	100.95	5995
3e	0.25	5000	0.05	0.005	1847	100.66	100.91	6847
3f	0.25	5000	0.05	0.002	4151	100.14	100.39	9151
3g	0.25	5000	0.05	0.001	7605	100.08	100.33	12605
4a	0.25	10000	0.025	0.1	122	30.85	31.10	10122
4b	0.25	10000	0.025	0.05	225	30.74	30.99	10225
4c	0.25	10000	0.025	0.02	509	30.41	30.66	10509
4d	0.25	10000	0.025	0.01	944	30.31	30.56	10944
4e	0.25	10000	0.025	0.005	1744	30.11	30.36	11744
4f	0.25	10000	0.025	0.002	3900	30.32	30.57	13900
4g	0.25	10000	0.025	0.001	7100	30.20	30.45	17100

3.2   Material properties

The 1.1 g RDX detonator is modelled as a sphere of detonated explosion products occupying the same volume as the undetonated explosive. Assuming a density of 1659 kg/m³ for RDX, the diameter of the charge is 10.83 mm; in the 1D grids, it occupies the leftmost grid cells in the range $0 \leq X \leq 5.415$ mm. The initialized state of a regular grid is shown in Figure 2. The detonated explosive products are modelled using the Jones-Wilkins-Lee (JWL) equation of state [22]–[24], in which pressure P is related to specific volume $v = \rho_0/\rho$ as follows:

$$P = \begin{cases} Ae^{-R_1 v} + Be^{-R_2 v} + \dfrac{C}{v^{1+\omega}} & , \quad P > 2 \times 10^{11} \text{ Pa} \\[2ex] A\left(1 - \dfrac{\omega}{R_1 v}\right)e^{-R_1 v} + B\left(1 - \dfrac{\omega}{R_2 v}\right)e^{-R_2 v} + \dfrac{\omega \rho_0 E}{v} & , \quad P \leq 2 \times 10^{11} \text{ Pa} \end{cases}$$

where A, B, C, R_1, R_2 and ω are constants whose values for RDX are given in Table 3.

The surrounding water is assumed to be fresh water and is modelled with the Tait equation, in which the pressure and density ρ are related as follows [25]:

$$P = P_0 + B((\rho/\rho_0)^n - 1)$$

where P_0 and ρ_0 are the reference pressure and density in the fluid, and where B and n are constants for which values are given in Table 3.
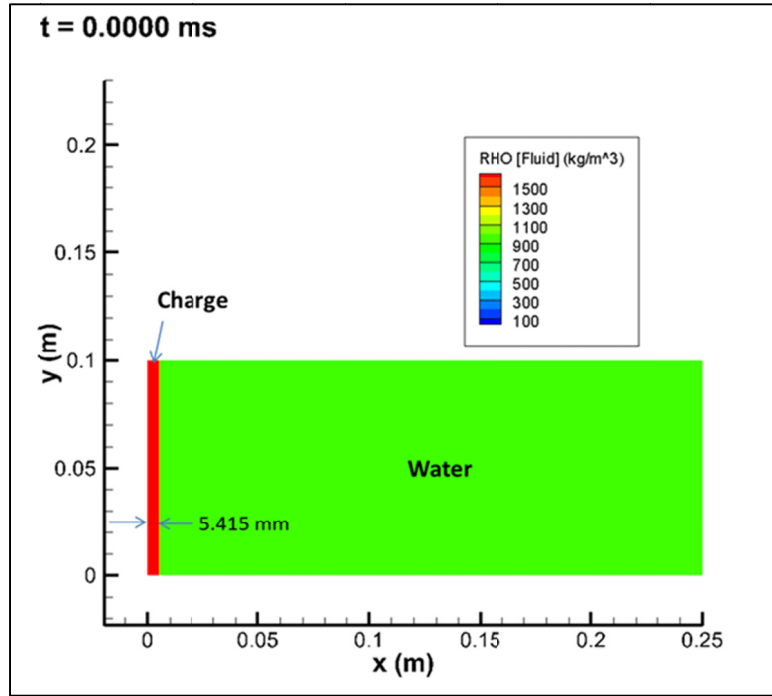
Figure 2: Initial material state for grid 4g. Only the regular grid is shown.

Table 3: Equation of state parameters.

Tait equation (water) [25]		JWL (RDX explosive) [26]	
ρ_0	1000.0 kg/m^3	ρ	1659 kg/m^3
P_0	101,325 Pa	A	495.1 GPa
B	3000 atm	B	7.21 GPa
n	7.14	C	1.62 GPa
m	5.00	R_1	4.387
α_c	0.05	R_2	0.9954
E_0	354 kJ/kg	ω	0.3469
		E_0	5877.9 kJ/kg

Note that the Tait and JWL parameters in Table 3 were not determined under the same conditions as empirical constants K_5 and K_6 introduced in the similitude formulas in Section 2, and this could be a minor source of discrepancy.

3.3 Other control parameters

Several parameters are used to control the Chinook solver, determine the time step size, and control Chinook's multimaterial calculations. These are summarized in Table 4 and Table 5. All the Chinook simulations in this report use the values given in these two tables.

Table 4: Chinook solver parameters.

Parameter	Value
Solver type	2 (HLLC)
Time marching method	0 (Single stage, first-order accurate)
Spatial order of accuracy	1 (Second-order accurate approximation)
Gradient type	0 (Green-Gauss)
Compression limiter	0 (First-order accurate space)

Table 5: Chinook time step and multimaterial parameters.

Parameter	Value
Courant number	0.5
Tolerance	1×10^{-8}
Maximum number of iterations	200
Pressure cutoff	1000.0 Pa
Scale factor	2.0

3.4   Results

Explosion simulations were performed for each of the grids in Table 2 with a surrounding hydrostatic pressure of 1 atm, consistent with a detonation at a shallow depth. The time duration simulated in each case was about 40 ms, which is sufficient time for one complete expansion and collapse of the gas bubble to occur.

For each simulation the maximum gas bubble radius is determined from contour plots of density, which are saved to disk at 0.5 ms intervals. Because Chinook uses a mixed cell method, in which explosion products and water can occupying the same cell, there is no clear boundary between explosion products and water in the simulations. The boundary of the bubble is instead characterized by a transition zone of mixed gas and water with density increasing in the radially outward direction. The gas bubble boundary is taken to be the 500 kg/m^3 density contour, i.e., the average of the densities of the gas and the water; this is used to determine the bubble radius A_1 as shown in Figure 3.

The bubble period, T_1, is the time from detonation ($t = 0$) to the first bubble collapse ($t = T_c$) as determined from pressure time histories at a monitor point a distance of R_m from the charge centre. An example time history is shown in Figure 4. A small correction factor is applied to account for the propagation of the pressure pulse to the monitor point: $T_1 = T_c - R_m/c$, where c is the sound speed in water.
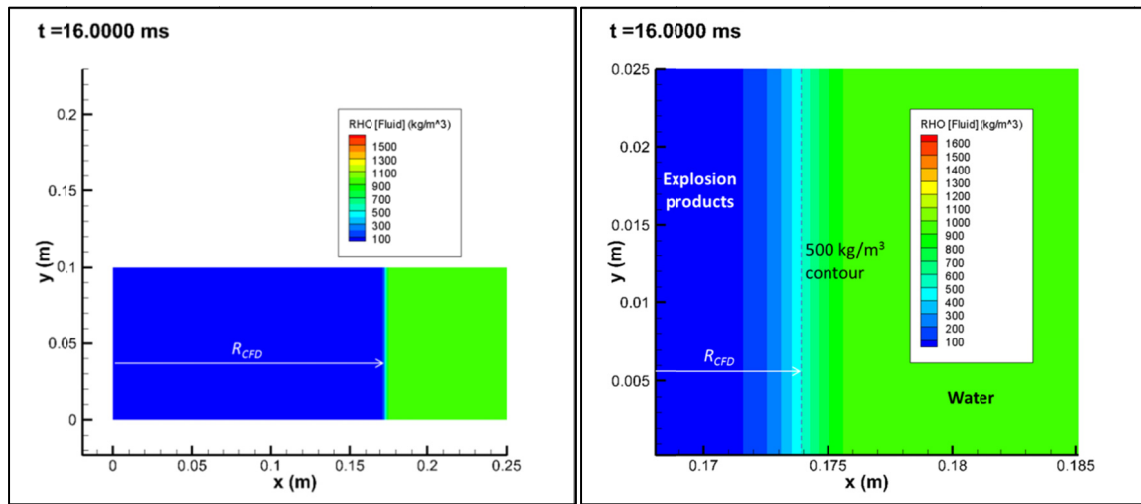
Figure 3: Density plot showing gas bubble near full expansion: full view (left); detailed view showing transition zone at the boundary of the bubble (right).

DRDC-RDDC-2016-R171
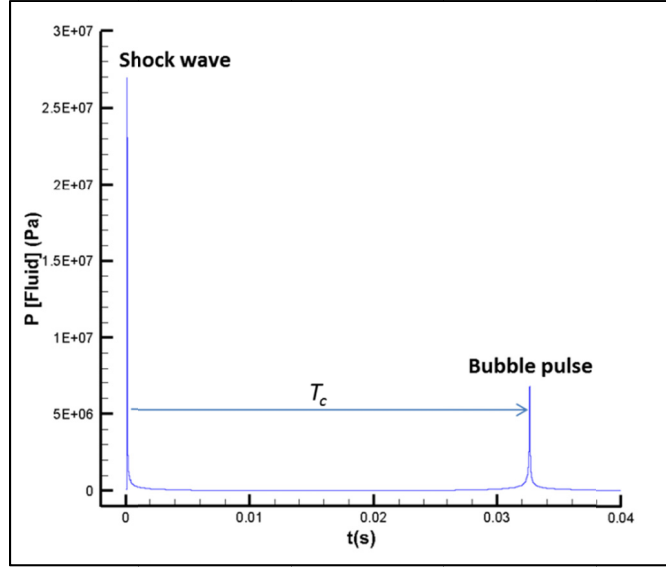
Figure 4: Pressure time history at a monitor point 0.18 m from the charge centre.

Figure 5 plots the ratio of the computed and reference bubble radii as a function of cell size and expansion factor, ξ; while Figure 6 plots the same for bubble period. Both the radius and period converge slowly, and very small elements are needed over a large portion of the grid to obtain a converged result. For the most refined model (Grid 4g), the 17,100 grid cells are needed, with a cell size of 0.025 mm in the part of the grid occupied by the gas bubble. If extended to three dimensions, a similar level of refinement would result in 10^{12} grid cells, far beyond the capabilities of existing computational tools.

Furthermore, with the material models and constants used in these simulations, the converged values for radius and period are about 3% smaller than the empirical values given by the similitude equations.
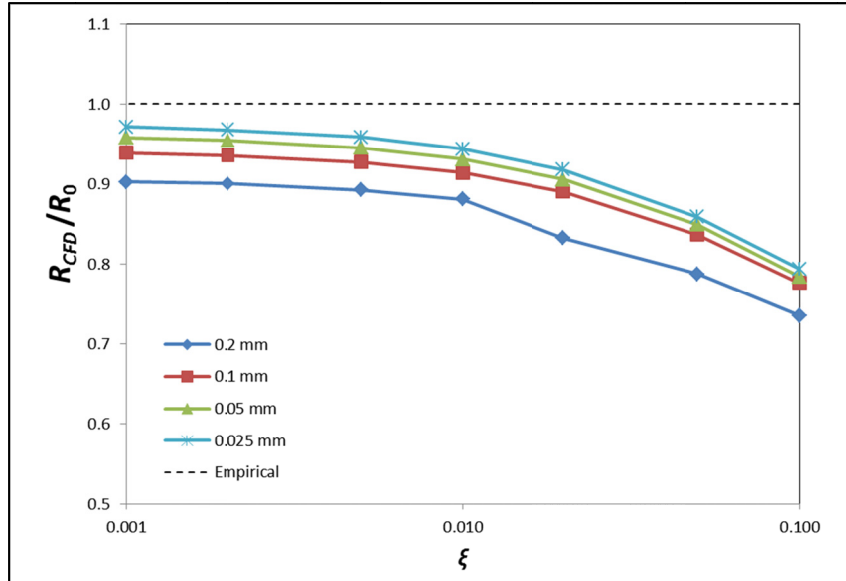
Figure 5: Ratio of gas bubble radii: 1D models.
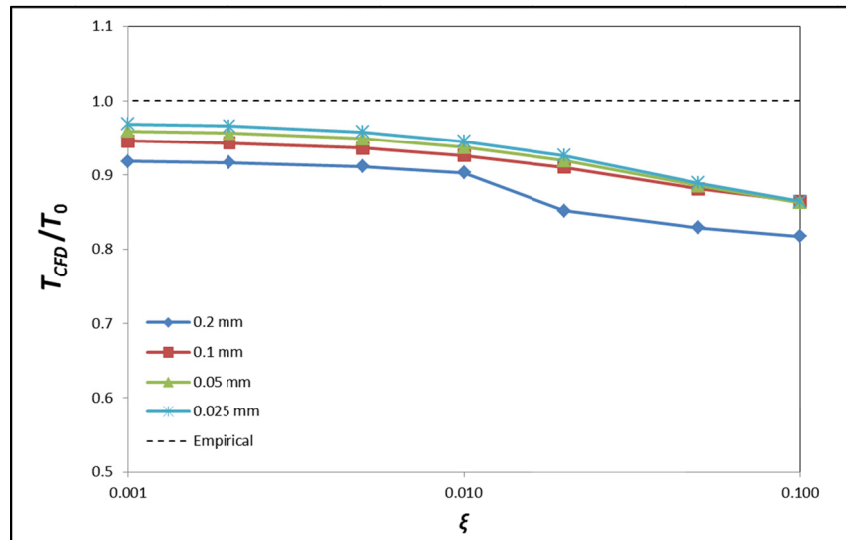
Figure 6: Ratio of gas bubble periods: 1D models.

4 2D benchmark cases

4.1 Free field models

The first series of two dimensional benchmarks are performed for a gas bubble pulsating in a free field. The basic layout of the fluid models is shown in Figure 7. A quarter-model of the fluid domain is used, with axisymmetry about the vertical (y) axis and normal reflective symmetry about the horizontal (x) axis. Symmetry about the y axis is imposed in Chinook by setting the "geom" parameter of the *GRID_EXTERNAL keyword to 1. The 1.1 g detonator is modelled as a cylinder of radius R_c and half-height y_c, with axis of symmetry aligned along the y-axis. The surrounding water domain is a sphere of radius R_3. It is subdivided into an inner zone, which is large enough to contain the full expanded bubble, and an outer zone.
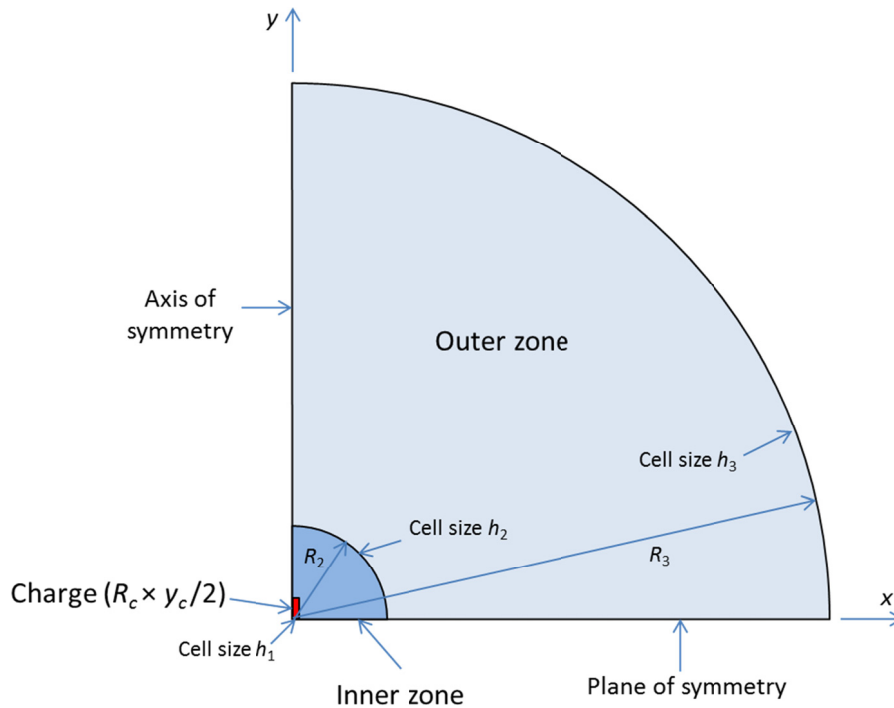
Figure 7: 2D free field model dimensions and cell size definitions.

Grids are generated with the Pointwise software [21], and these are then exported to CFD++ format from which they are converted to Chinook format. Three cell sizes are used to define the gridding: a uniform cell size for the charge (h_1); the cell size at the outer boundary of the inner zone (h_2); and the cell size at the outer boundary of the outer zone (h_3). The distribution of cell sizes along the radial boundaries of the inner and outer zones is determined using a hyperbolic tangent stretching function in the Pointwise software, limited by the cell sizes at the outer and inner boundaries. This defines the cell sizes on all of the boundaries of the inner and outer zones; the cell size throughout the inner and outer zones is determined by the gridding algorithm in Pointwise, using the boundary cell sizes and a boundary decay function. The parameter controlling the boundary decay function is selected to be a value close to 1.0, which creates a reasonably uniform transition of cell sizes

from inner to outer boundary. In total, five different grids were created and analyzed, with the dimensions and cell sizes listed in Table 6. The FF2 mesh is shown in Figure 8.

Table 6: Summary of 2D free field models.

Name	R_c (mm)	$y_c/2$ (mm)	R_2 (m)	R_3 (m)	h_1 (mm)	h_2 (mm)	h_3 (m)	No. cells
FF1	3.375	9.3	0.25	50	0.5	1	0.5	456,175
FF2	3.375	9.3	0.25	50	0.5	2	1	259,953
FF3	3.375	9.3	0.25	50	0.5	4	2	129,756
FF4	3.375	9.3	0.25	50	0.5	8	4	79,831
FF5	3.375	9.3	0.25	50	0.5	16	4	29,115
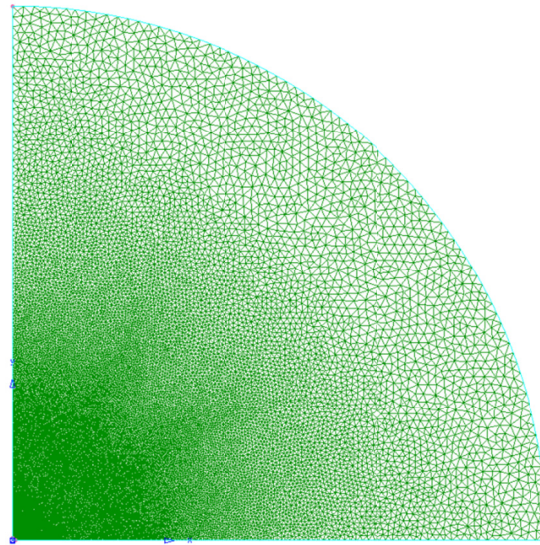
Figure 8: Free field model FF2.

The material properties for the RDX explosive and water are identical to those used for the one-dimensional analyses, and are listed in Table 3. An initial uniform ambient pressure of 1 atm is assumed in the volume of water. Gravity is not included.

Simulations are run for approximately 65 ms, sufficient time for the first two bubble collapses. Results for the maximum gas bubble radius in the horizontal (A_{1x}) and vertical direction (A_{1y}), as well as the average bubble radius $A_1 = (A_{1x} + A_{1y})/2$ and the bubble period (T_1) are summarized in Table 7 for the first bubble pulse. These values are also compared with the empirical values. The maximum bubble radius is determined along the two coordinate axes, using the 500 kg/m3 contour as the surface of the bubble.

The average of the maximum radii is within 2.1% of the empirical radius, and the predicted bubble period is within 1.5% of the empirical value, for all five of the grids. Even the coarsest 2D grid, with only 29,115 cells, gives a more accurate result than the finest 1D grid used in Section 3. The maximum horizontal radius is always slightly larger than the maximum radius in the vertical direction, and this is likely due to the initial cylindrical charge shape.

Table 7: 2D free field model results for the first bubble pulse.

Grid	A_{1x}(m)	A_{1y} (m)	A_1/A_1^*	T_1 (ms)	T_1/T_1^*
FF1	0.1786	0.1753	0.989	33.51	0.996
FF2	0.1781	0.175	0.987	33.40	0.993
FF3	0.1781	0.1752	0.988	33.39	0.992
FF4	0.1781	0.1742	0.985	33.34	0.991
FF5	0.1768	0.1732	0.979	33.15	0.985

Table 8 gives the results for the second bubble pulse, where the average radius of the second pulse is $A_2 = (A_{2x} + A_{2y})/2$. The second pulse radius converges to a value that is slightly less than 80% of the first pulse, and for grid FF1 is approximately 10% greater than the empirical value A_2^*. For grid FF1, the second bubble period is close to 85% of the first bubble period, but is nearly 20% larger than the empirical value.

Table 8: 2D free field model results for the second bubble pulse.

Grid	A_{2x}(m)	A_{2y} (m)	A_2/A_1	A_2/A_2^*	T_2 (ms)	T_2/T_1	T_2/T_2^*
FF1	0.1385	0.1407	0.789	1.108	28.29	0.844	1.193
FF2	0.1351	0.1373	0.771	1.081	27.86	0.834	1.175
FF3	0.1336	0.1362	0.764	1.070	27.72	0.830	1.169
FF4	0.1313	0.1341	0.752	1.053	27.44	0.823	1.157
FF5	0.1258	0.1281	0.725	1.007	26.72	0.806	1.127

Figure 9 gives a sequence of images showing the gas bubble expansion and contraction during the first bubble pulse. The bubble is seen to maintain a nearly spherical shape throughout its first expansion and collapse, and only at the bubble minimum, near 33.5 ms, can a significant distortion from the spherical shape be noted. The second bubble pulse (Figure 10) is similar but with a smaller maximum radius. Figure 12 shows the pressure time history at the monitor point location shown in Figure 11. The pressure time history indicates the large reduction in the peak pressures between the first and second collapse.

Figure 9: Progression of the gas bubble during the first expansion and collapse: grid FF2. Colours indicate density in kg/m³.

Figure 10: Progression of the gas bubble during the second expansion and collapse: grid FF2. Colours indicate density in kg/m³.
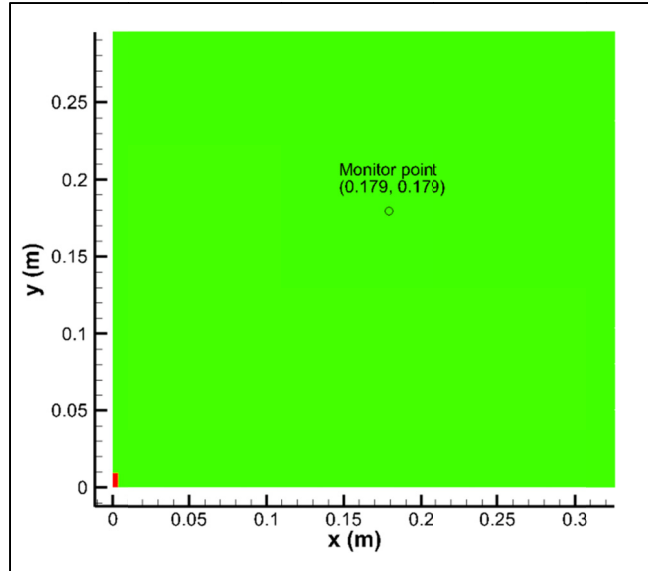
Figure 11: Monitor point location in 2D free-field grids.
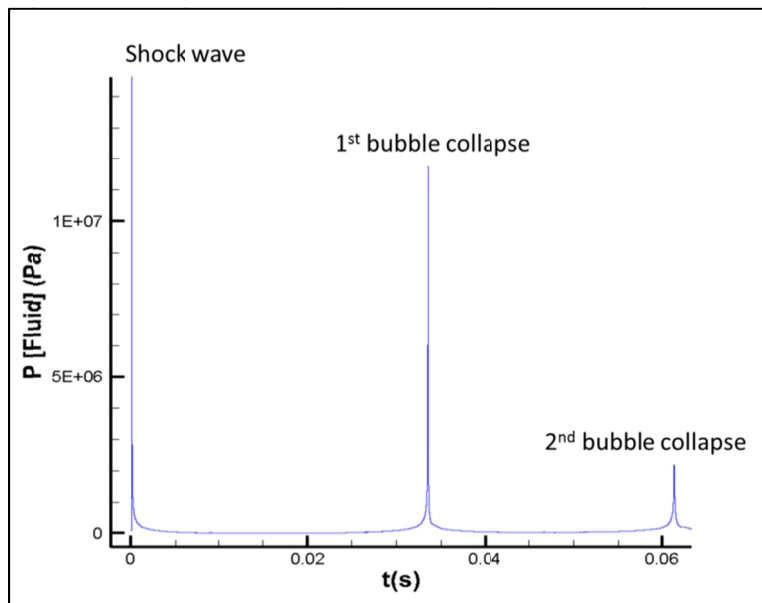
Figure 12: Pressure time history at the monitoring point: grid FF2.

4.2 Free surface models

A series of 2D simulations were performed with the model arrangement shown in Figure 13. These models are axisymmetric about the vertical axis and contain a small air volume above the free surface. The charge is located at a depth, *d*, such that the gas bubble will not breach the surface during the initial expansion. Acceleration of gravity is included in the model and the water volume is initialized with a hydrostatic pressure gradient.

18   DRDC-RDDC-2016-R171

Grids are generated in a manner similar to the free field models. A uniform cell size is prescribed for the charge (h_1), and boundary between the inner and outer zones (h_2) and the outer boundary of the outer zone (h_3). A fourth cell size (h_4) is used to control the expansion of the cell size in the region above the charge. Along the radial boundaries, and along the top boundary of the domain, the grid cell size is controlled using a hyperbolic tangent stretching function. The cell size in the interior of the domain is controlled using the Pointwise's boundary decay function, using a parameter value close to 1.0.
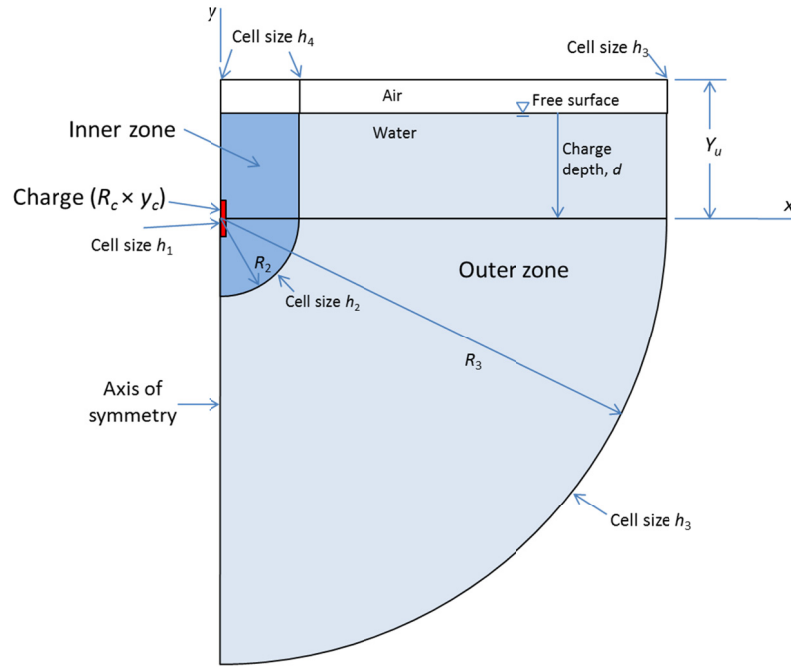
Figure 13: 2D free surface model dimensions and cell size definitions.

The grids generated for the free surface models are listed in Table 9. The charge dimensions are identical to those used in free field model, except that the full height of the charge (y_c) is now being modelled due to the absence of the horizontal symmetry plane. The material properties for the RDX explosive and water are identical to those used for the free field models and are listed in Table 3. The air is modelled as an ideal gas with properties given in Table 10. An example of a meshed grid is shown in Figure 14.

Table 9: Summary of 2D free surface models.

Name	R_2 (m)	R_3 (m)	Y_u (m)	d (m)	h_1 (mm)	h_2 (mm)	h_3 (m)	h_4 (mm)	No. cells
FS1	0.25	50	1.0	0.3	0.5	1	1	40	508,854
FS2	0.25	50	1.0	0.3	0.5	2	1	40	375,388
FS3	0.25	50	1.0	0.3	0.5	4	2	40	228,048
FS4	0.25	50	1.0	0.3	0.5	8	4	40	151,712
FS5	0.25	50	1.0	0.3	0.5	16	4	40	84,028
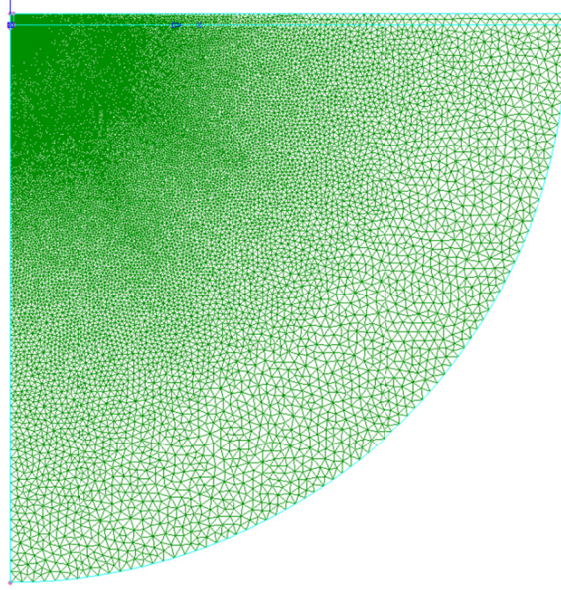
Figure 14: Free surface model FS2.

Table 10: Equation of state parameters for air.

Ideal gas properties for air	
ρ_0	1.177 kg/m^3
γ	1.4
E_0	215 kJ/kg

The simulations were run for 65 ms, sufficiently long for two complete bubble collapses. Field variables for the entire domain were stored at 0.5 ms intervals, while field variables at the two monitor points shown in Figure 15 were continuously recorded.

The pressure time history at a distance R_0 away from the charge is shown in Figure 16 for grid FS2. The pressure pulses generated by the bubble collapse are truncated by the reflection of the pulse in the free surface. This produces a region of near zero pressure immediately following the peak of the pressure pulse at 29.2 ms. The pressure pulse is effectively cut off by the reflection in the free surface. A similar effect can be seen in the 2nd pressure pulse at 55.6 ms. Figure 17 shows the progression of the bubble during its initial expansion and first collapse, showing the transition from a nearly spherical shape at maximum expansion (15 ms) to toroidal shape immediately after the bubble minimum at 29.3 ms. A water jet forms just prior to the bubble minimum and can be seen to fully penetrate the bubble at 30 ms. The sequence of images for the second bubble expansion and collapse (Figure 18) shows that the bubble retains its toroidal topology until the second collapse at 55.6 ms. After this time, the bubble reforms with a more complex geometry as seen in the contour at 60 ms.
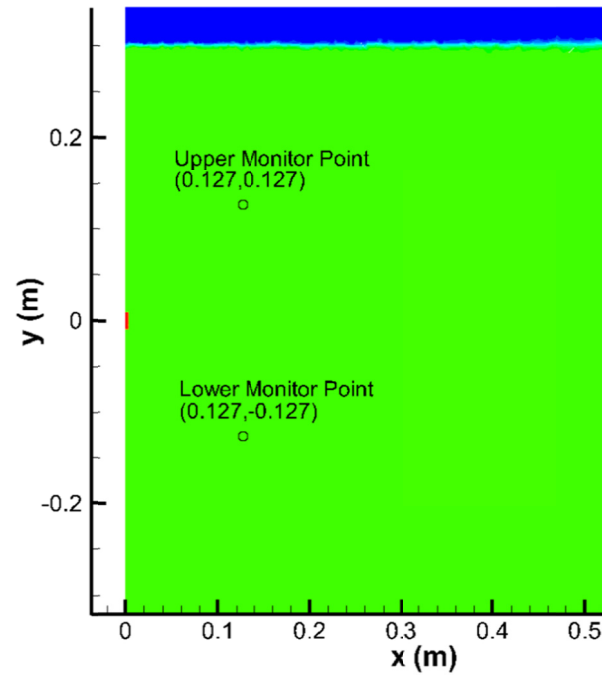
Figure 15: Monitor point locations for 2D free surface simulations.
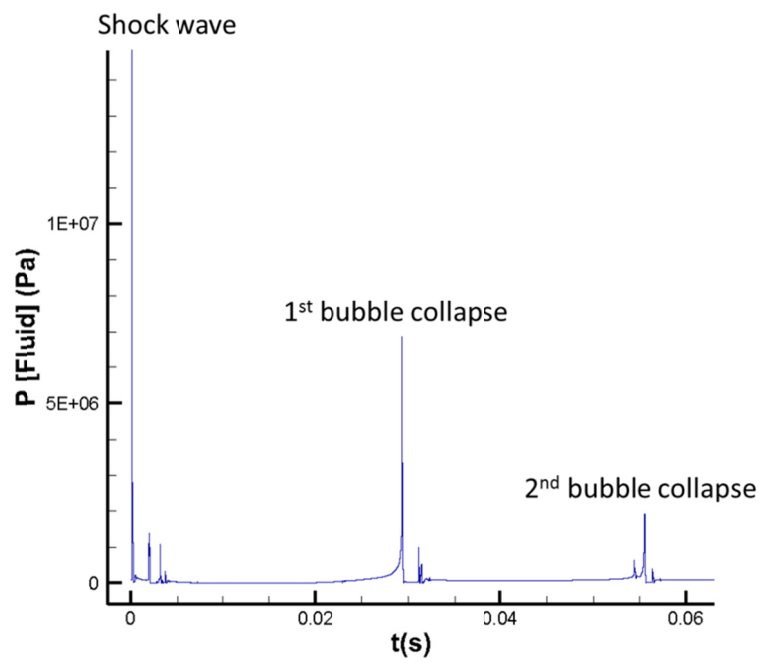
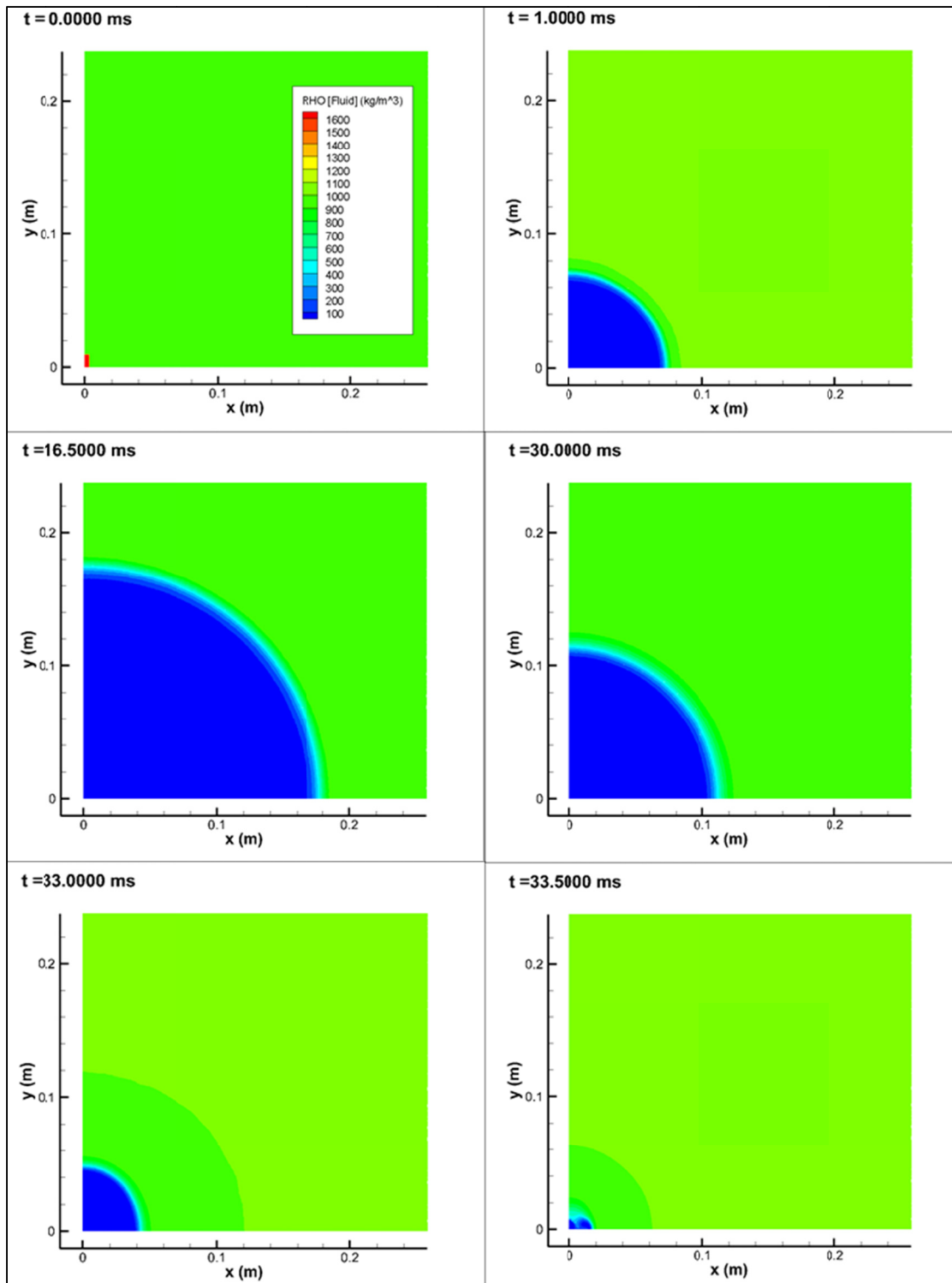*Figure 16: Pressure time history at the upper monitoring point: grid FS2.*
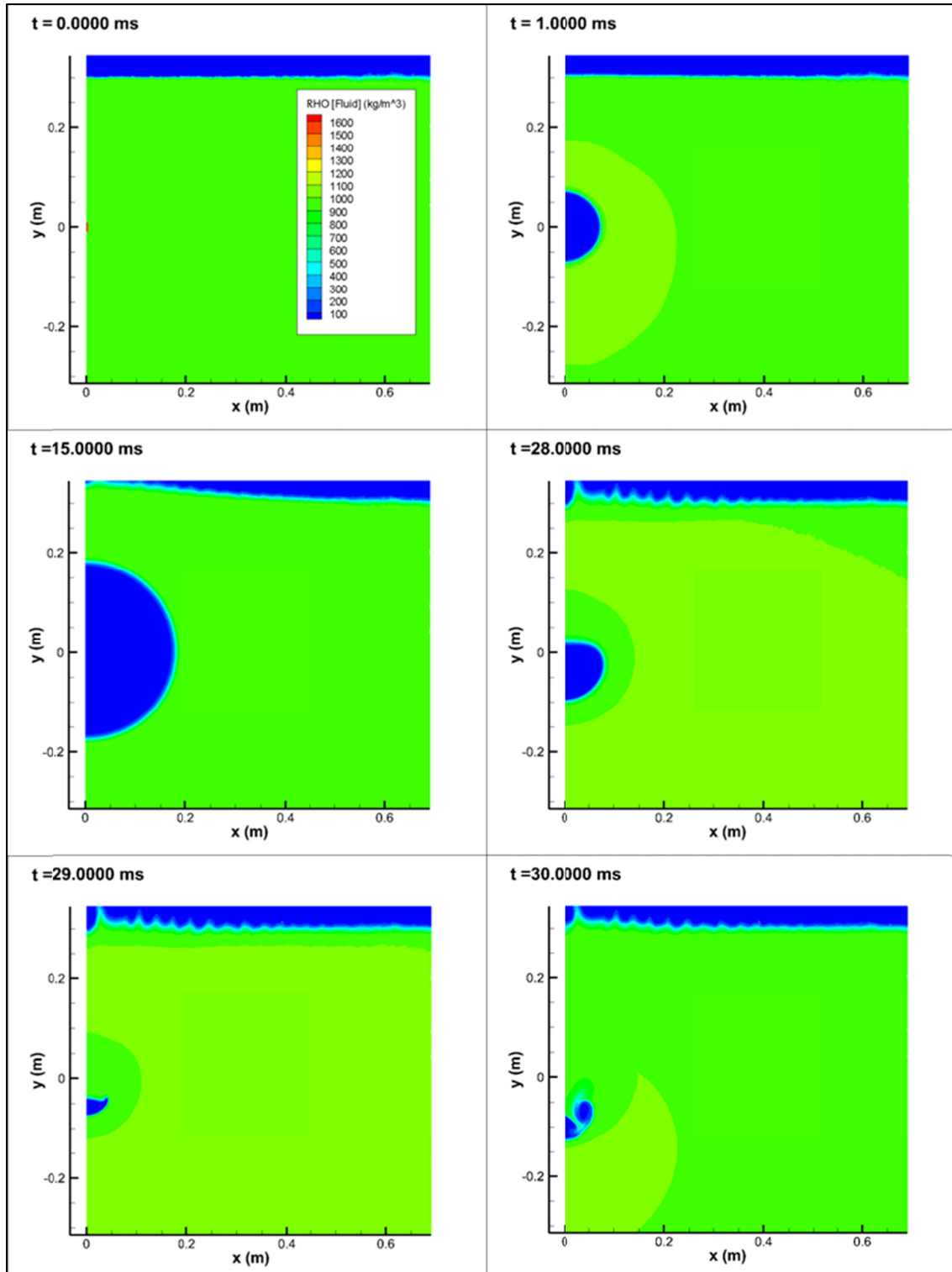
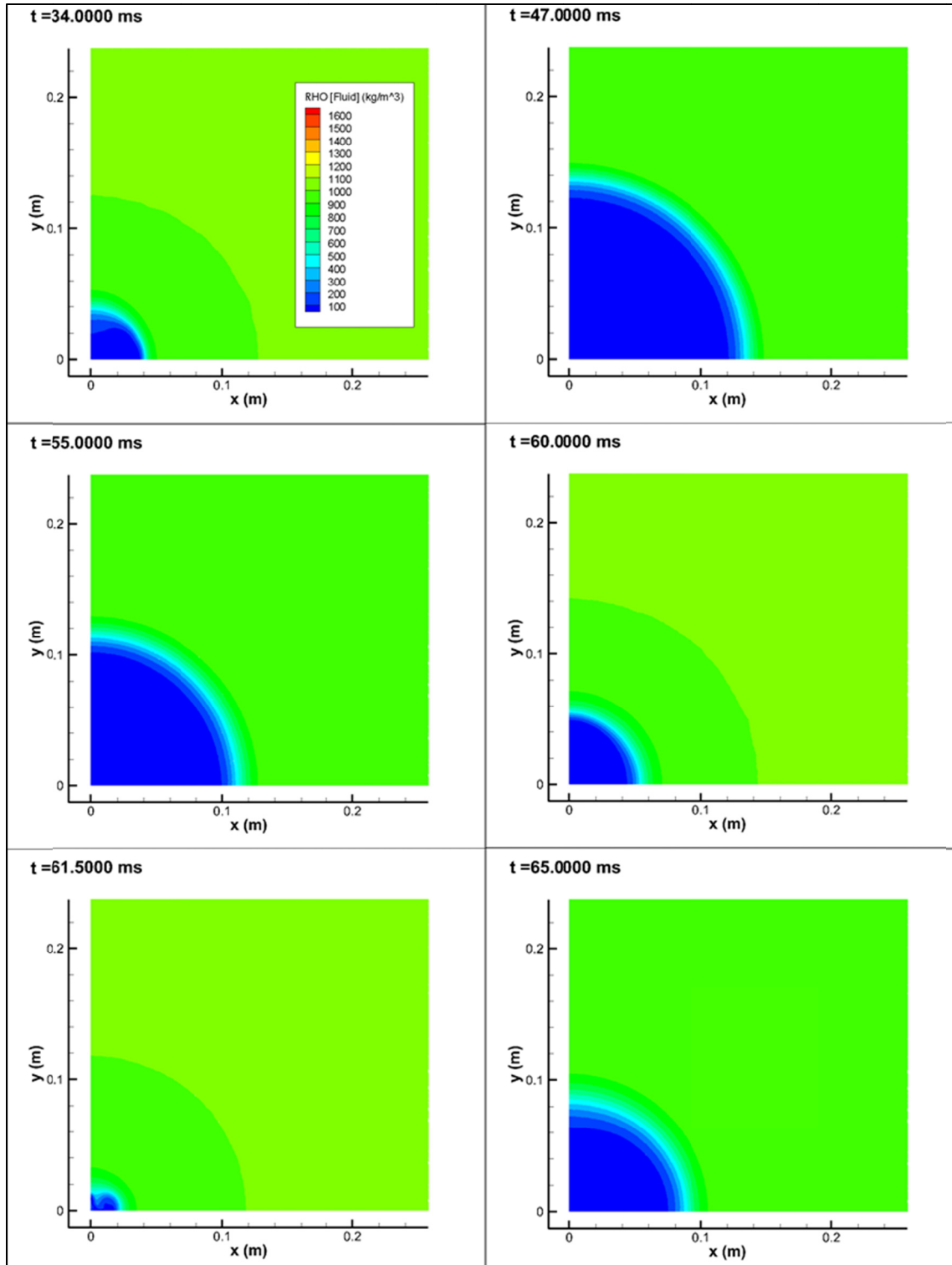*Figure 17: Progression of the gas bubble during first expansion and collapse: grid FS2. Colours indicate density in kg/m³.*
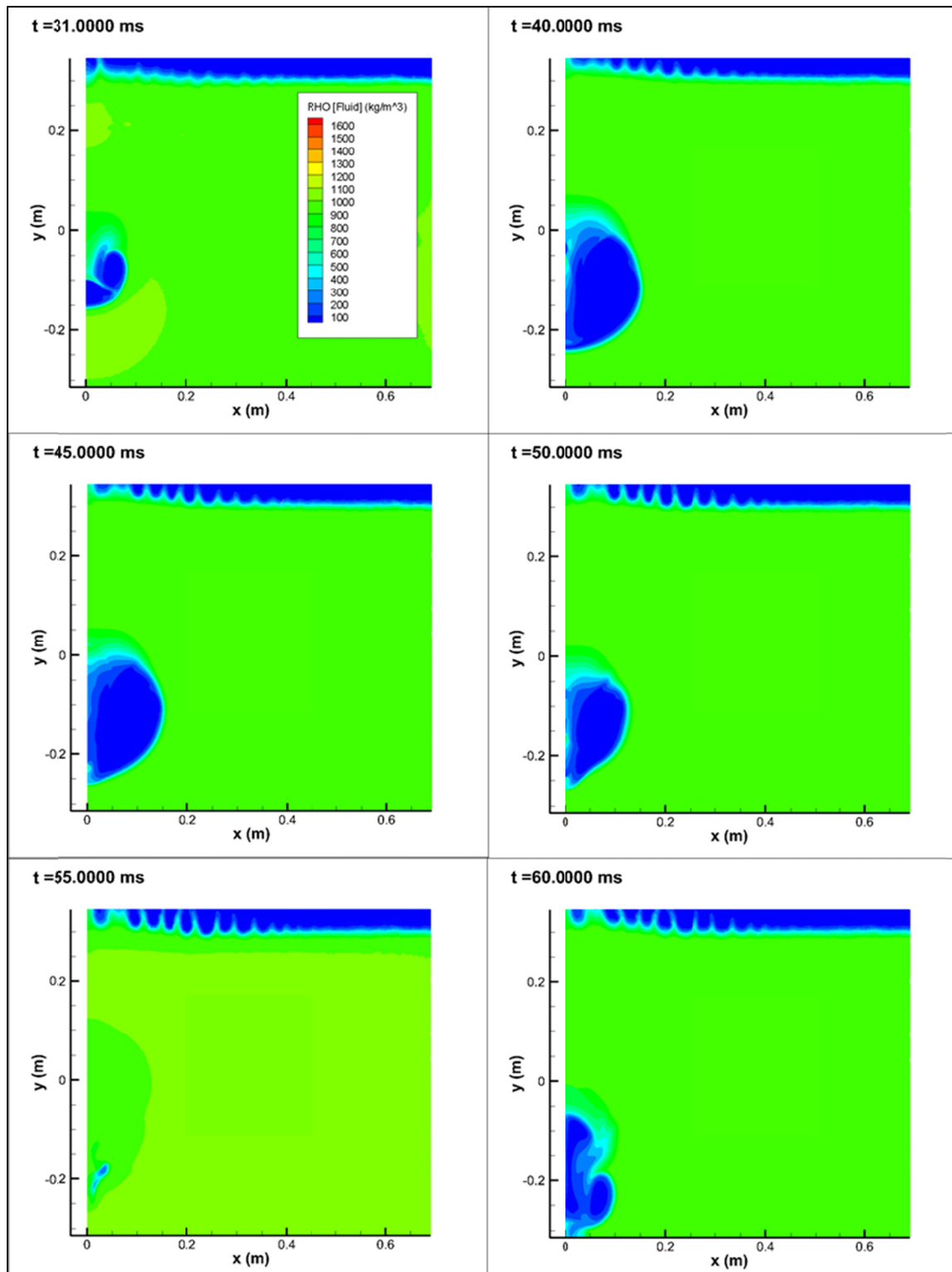
Figure 18: Progression of the gas bubble during second expansion and collapse: grid FS2. Colours indicate density in kg/m³.

The pressure pulse generated by the bubble collapse can be seen in Figure 19. The contour at 29.5 ms shows the pressure wave propagating away from the collapsed bubble. This pressure wave interacts with the free surface at the top of the frame. To maintain the pressure release condition at the free surface, a rarefaction wave is generated wherever the pressure wave contacts the free surface. This results in a low pressure zone (dark blue) initially at the free surface and behind the pressure pulse. By 30 ms, this has spread to surround the region of the re-expanding bubble.
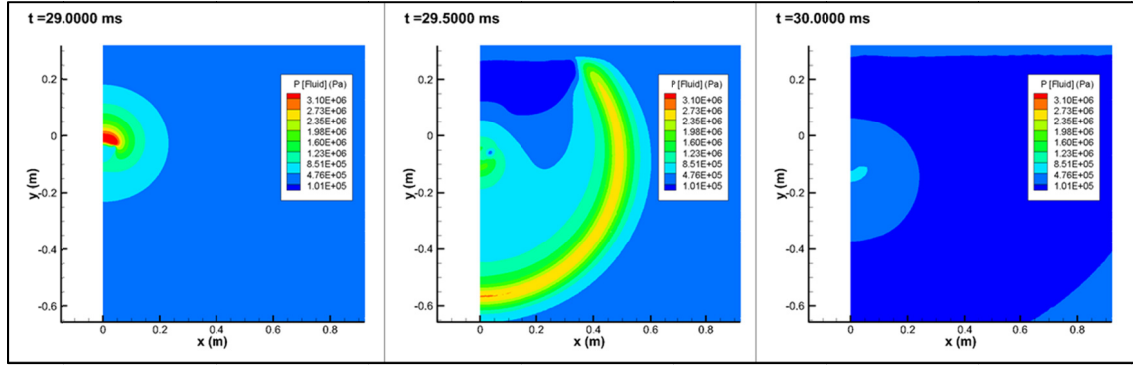
Figure 19: Fluid pressures during first bubble collapse. Colours indicate pressure in Pa.

The maximum horizontal and vertical bubble radii for the five free surface models are given in Table 11 for the first bubble pulse, along with the first bubble periods. The average radius agrees with the empirical value to within 2%, while the bubble period is within 1% of the empirical value for all five of the grids. The agreement in the bubble period confirms the importance of the free surface correction factor in (3) and (4).

Table 11: 2D free surface model results for first bubble cycle.

Grid	A_{1x}(m)	A_{1y} (m)	A_1/A_1^*	T_1 (ms)	T_1/T_1^*
FS1	0.1808	0.179	1.016	29.19	1.008
FS2	0.1809	0.1791	1.016	29.21	1.009
FS3	0.1803	0.1787	1.013	29.14	1.006
FS4	0.1799	0.1785	1.012	28.99	1.001
FS5	0.1776	0.1773	1.002	28.82	0.995

Table 12 gives the free-surface results for the second bubble pulse. The second pulse radius is the outer radius of the entire bubble, encompassing the toroidal structure. As a result, the horizontal radius is somewhat larger than the vertical radius, and the average radius is larger than it is in the free field case. Both the second pulse radii and the periods are considerably larger than the empirical values. Table 12 also reports the bubble depth at the time of maximum expansion, and from this it can be seen that from the first to the second pulse the bubble migrates from a depth of 0.3 to 0.41 m.

Table 12: 2D free surface model results for the second bubble pulse.

Grid	A_{2x}(m)	A_{2y} (m)	A_2/A_1	A_2/A_2^*	T_2 (ms)	T_2/T_1	T_2/T_2^*	d_2 (m)
FS1	0.1556	0.1384	0.817	1.178	26.49	0.907	1.249	0.414
FS2	0.1552	0.1359	0.809	1.166	26.27	0.899	1.238	0.412
FS3	0.1534	0.13565	0.805	1.158	26.10	0.896	1.230	0.413
FS4	0.1526	0.131	0.791	1.136	25.31	0.873	1.193	0.412
FS5	0.1410	0.115	0.721	1.026	24.80	0.860	1.169	0.402

4.3   2D FSI benchmark cases

The 2D free surface grids are now used to simulate the interaction of an explosion gas bubble with a target structure, using the fluid-structure interaction (FSI) capability in Chinook. In the latter, a Chinook simulation is run concurrently with an LS-Dyna analysis of the target structure. The two simulations are coupled using the *FSI keyword in Chinook, and the *USER_LOADING feature in LS-Dyna. In the coupling scheme, fluid forces calculated by Chinook are passed to the LS-Dyna analysis, and structure velocities computed by LS-Dyna are passed to Chinook.

In the present section, Chinook 2D axisymmetric grids are coupled with 3D target models, in such a way that the loading is applied axisymmetrically to the target structure. The basic target structure is a circular plate with diameter of 1.0 m attached to a cylindrical shell (Figure 20). In all of the FSI simulations, the entire structure is floated on the surface with the circular plate face down such that the centre of the circular plate is positioned exactly 0.179 m above the centre of the charge (Figure 21). The free surface is located at 0.3 m above the centre of the charge, giving the target a draft of 0.121 m. In all cases, the target is air-backed, and a hydrostatic pressure gradient is defined in the surrounding water volume, relative to the free surface.
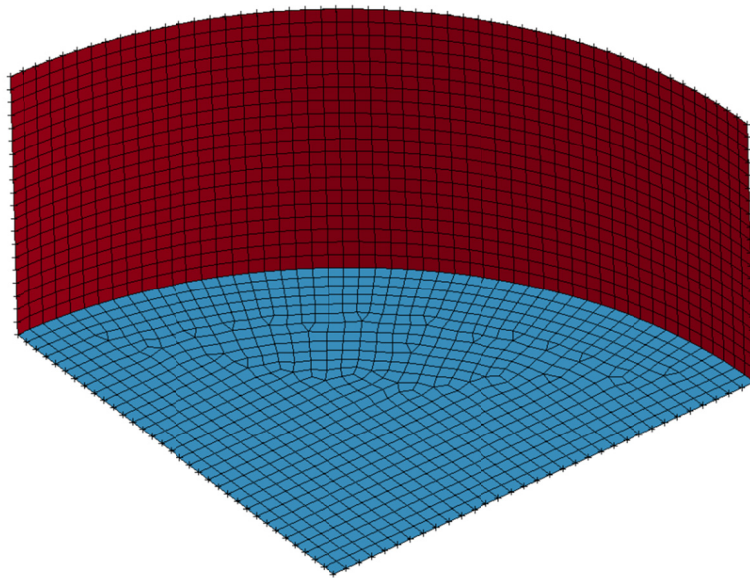
Figure 20: One-quarter model of target plate with cylindrical wall.
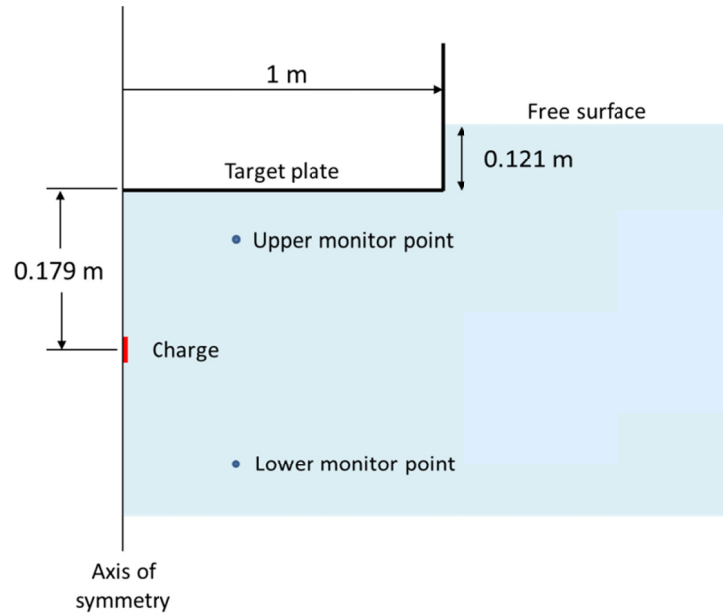
Figure 21: Configuration for FSI simulations.

Four different versions of the target structure are analysed, each representing a different level of rigidity and restraint of the target. These are listed in Table 13.

Table 13: Four variations of target model used in FSI simulations.

Name	Material	Thickness	Restraint
Rigid-Fixed	Rigid	N/A	Fixed
Rigid-Free	Rigid	N/A	Free
Fixed	Steel	4.76 mm	Fixed at top of cylinder
Free	Steel	4.76 mm	Free

4.3.1   Rigid-fixed target model

The rigid-fixed target model has all degrees-of-freedom restrained and is coupled to the Chinook analysis using the small deformation coupling scheme (velocity coupling only). The FS3 grid is used, with identical material properties as were used in Section 4.2. The simulation was run with a coupling interval of 0.5 µs and the total duration simulated was 65 ms.

Inspection of the LS-Dyna results confirmed that the structure did not move throughout the simulation. The behaviour of the gas bubble is illustrated in the pressure time-history at the centre of the plate (Figure 22). This shows that bubble collapse occurs at 34.97 ms, which is about 4% longer than the empirical free-field value for bubble collapse, and is considerably longer than the free field periods computed in Section 4.2. The pressure time histories at the upper monitor point (Figure 23) shows similar magnitude of pressure pulse as that seen on the plate surface.
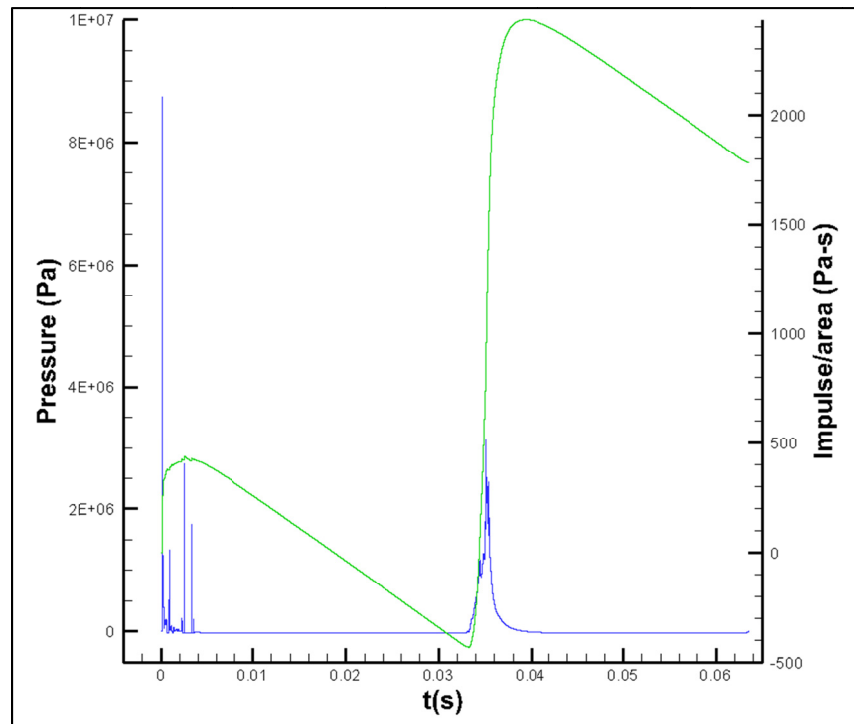
Figure 22: Pressure time history at centre of target plate: rigid-fixed model.
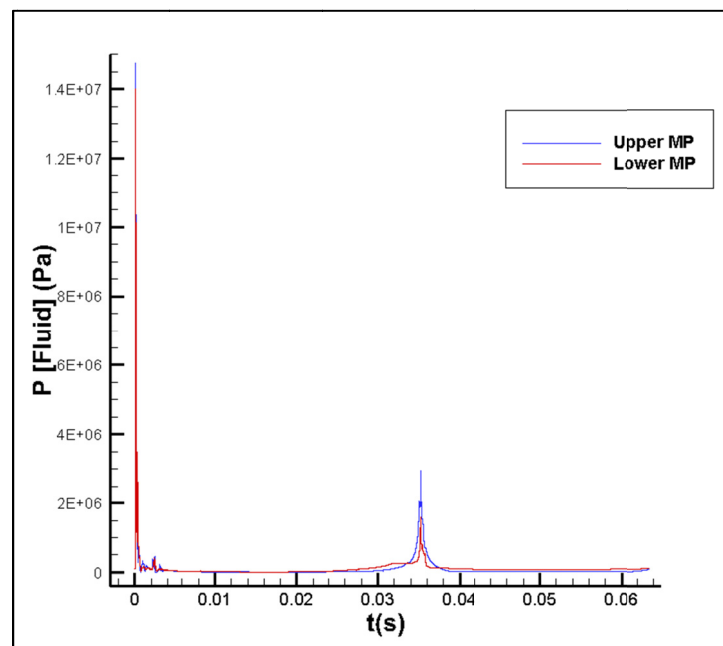
Figure 23: Fluid pressure time history at monitor points: rigid-fixed model.

The contour plots in Figure 24 shows the *y*-component fluid velocity (*v*) generated during the first bubble collapse. These velocities are strongly positive indicating that the jet is directed toward the target plate. This is as expected, and is opposite to the free surface case in which the jet was directed downwards. The half-width of the jet is approximately 40 mm. The complete evolution of the bubble through two pulses is shown in Figure 25 and Figure 26 in which the position of the target structure is indicated by the blue rectangle above the gas bubble. The gas bubble reaches maximum expansion at 16.5 ms, at which time the horizontal radius is 0.1795 m and the vertical radius is only 0.162 m. Considerable flattening of the bubble therefore occurs as a result of target; the upper surface of the bubble at maximum expansion is 30 mm away from the target surface. At the moment when the bubble jet appears to have fully penetrated the bubble (34 ms), the bubble is about 15 mm away from the surface of the plate. During the second expansion (Figure 26) the bubble is in contact with the target plate. The gas volume is now approximately toroidal but is divided into at least three distinct cells during this second expansion and exhibits some turbulent mixing of gas and water within the cells. The simulation ended before second collapse was complete.
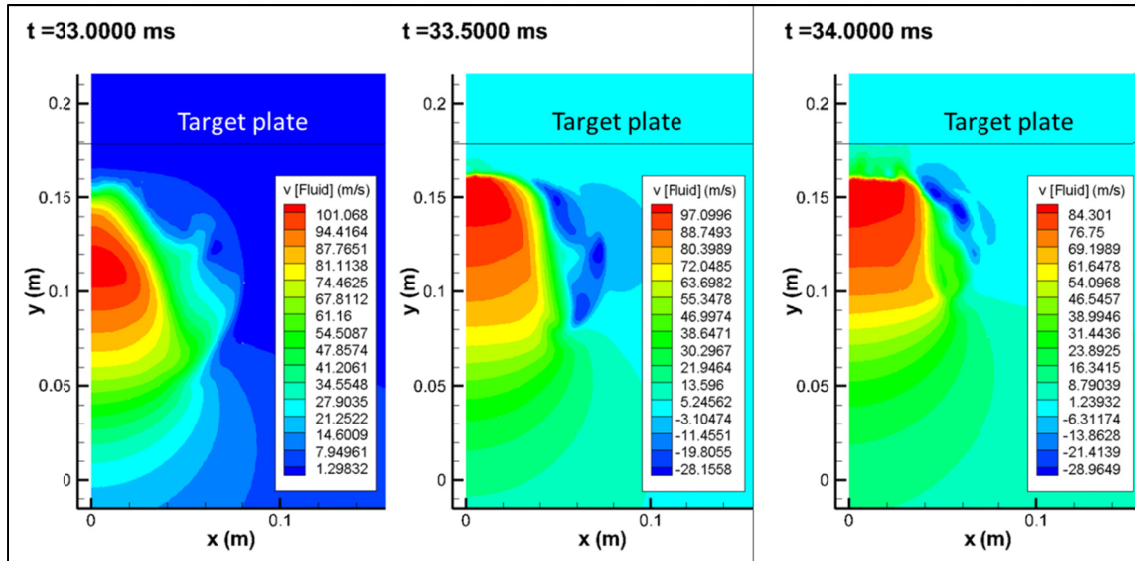
Figure 24: Fluid velocity during first water jet formation: rigid-fixed model.
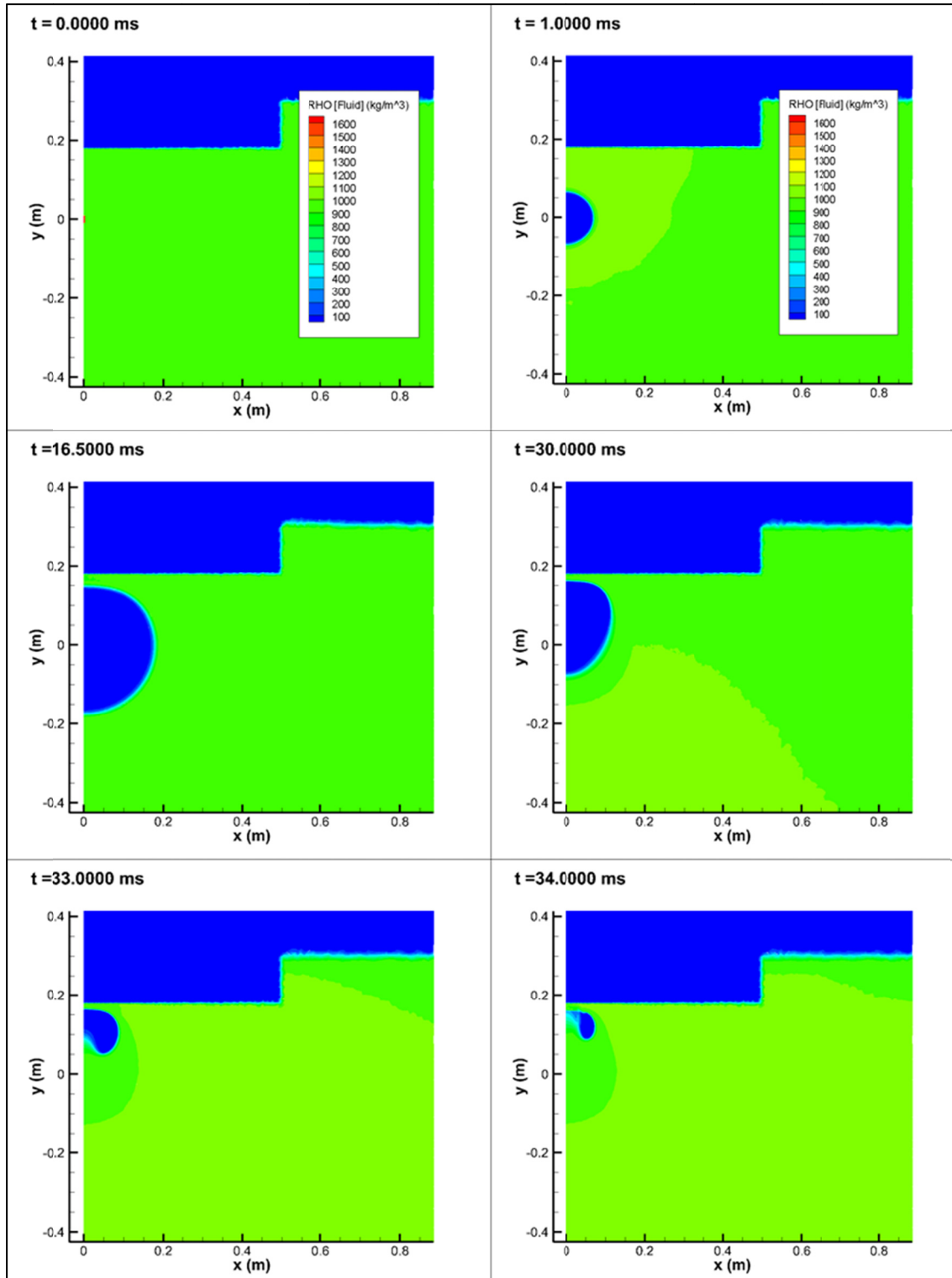
Figure 25: Progression of the gas bubble during first expansion and collapse: grid FS3 with rigid-fixed target. Colours indicate density in kg/m³.
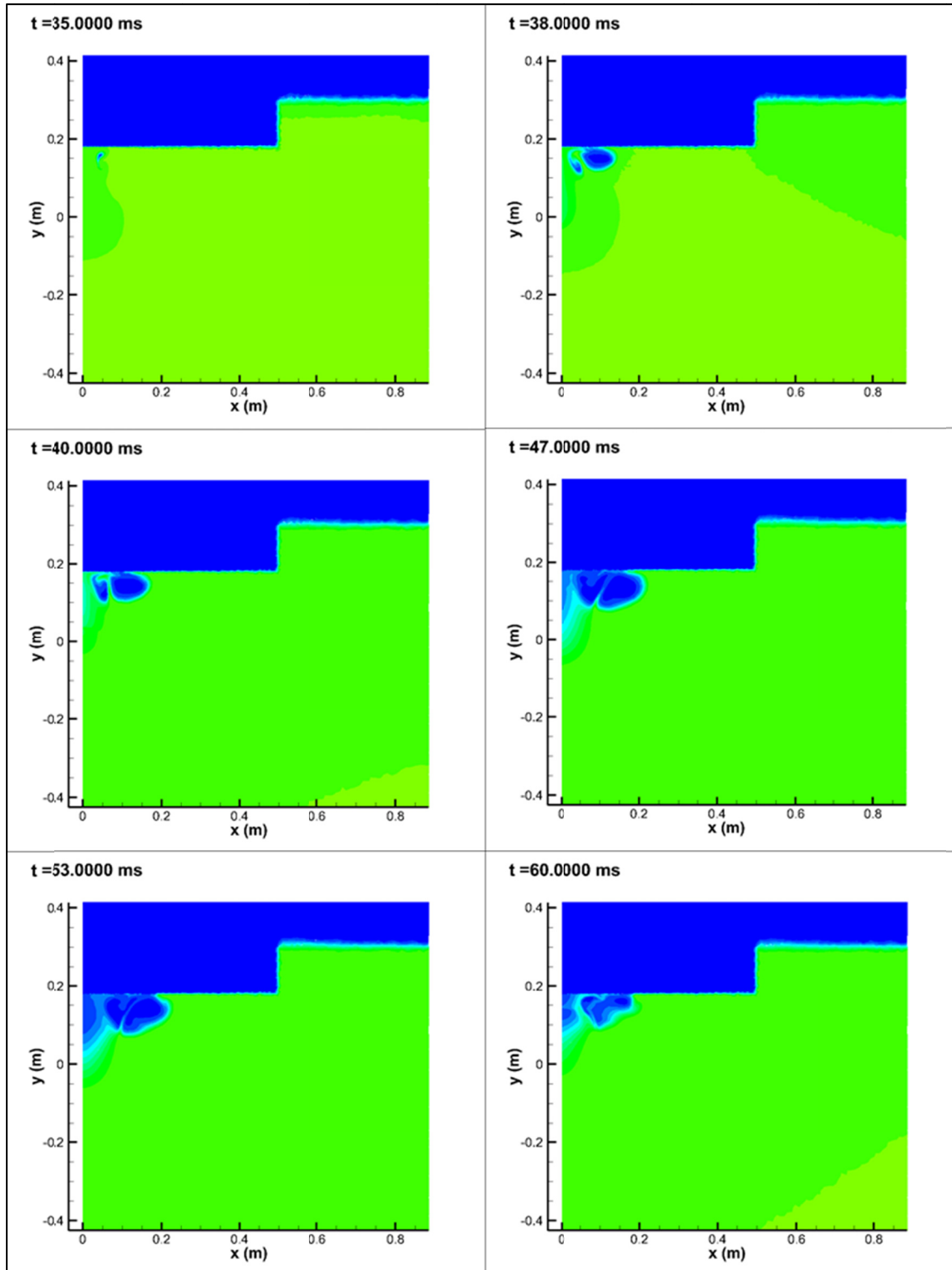
Figure 26: Progression of the gas bubble during second expansion and collapse: grid FS3 with rigid-fixed target. Colours indicate density in kg/m3.

4.3.2 Rigid-free target model

The rigid-free model uses a *MAT_RIGID material model in LS-Dyna, but is free to undergo rigid body motion. The target model is coupled to the Chinook analysis using both the small deformation coupling scheme, in which LS-Dyna velocities are passed to Chinook; and the large deformation coupling scheme, in which LS-Dyna velocities are passed to Chinook and the position of the fluid-structure interface is updated at regular intervals. A gravity load was applied to the target model during the LS-Dyna analysis to balance the hydrostatic forces acting on the partial submerged target. The simulations performed are summarized in Table 14.

Table 14: Summary of 2D rigid-free target FSI simulations.

Name	Coupling	Chinook grid	Coupling interval (µs)	Simulation duration (ms)
RF-S	Small	FS3	0.5	65.5
RF-L	Large	FS3	0.5	56.1

The pressure time history at the centre of the circular plate is shown in Figure 27 and Figure 28 for simulation RF-S and RF-L, respectively. These plots show that the peak pressure associated with the first collapse are similar for RF-S and RF-L; while for the second collapse, the peak pressures differ by more than a factor of 3. The time history of the impulse per unit area imparted to the target plate at the plate centre is also given in these two figures. The changes in impulse, differ somewhat for the first pulse, but are quite similar for the second pulse. The change in impulse is generally not well correlated with the peak pressure value. The results also show that significant differences in the loading experienced by the target plate can result from the different coupling schemes. For example, the total change in impulse over the two pressure pulses is about 3000 Pa-s greater for simulation RF-S.

The fluid velocity at the two collapse events is shown in Figure 29 and Figure 30. This shows that the velocities of the re-entrant jet during the first collapse are much larger than the subsequent water jetting at the second collapse. The half-width of the jet is in both cases about 20 mm, which is narrower than the one seen with the rigid-fixed target.
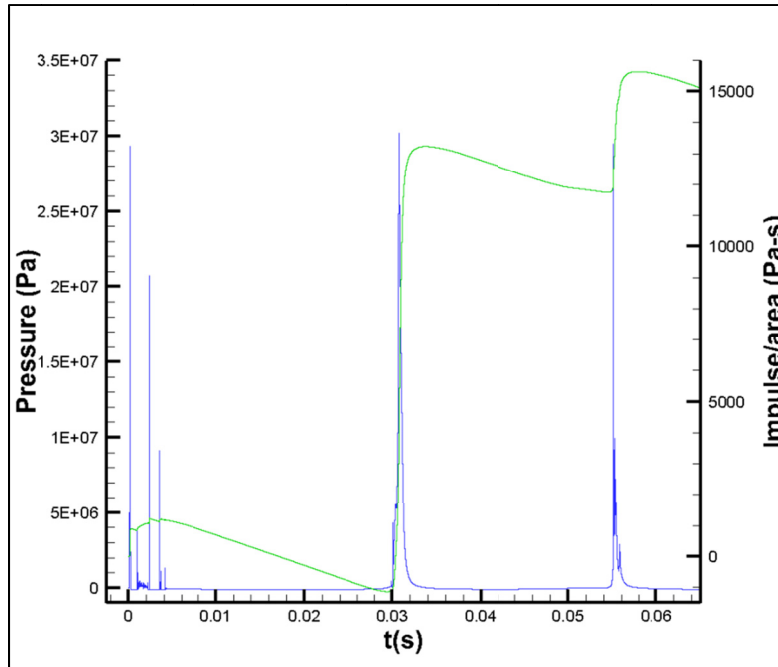
Figure 27: Pressure and impulse time histories at centre of target plate: rigid-free model, simulation RF-S.
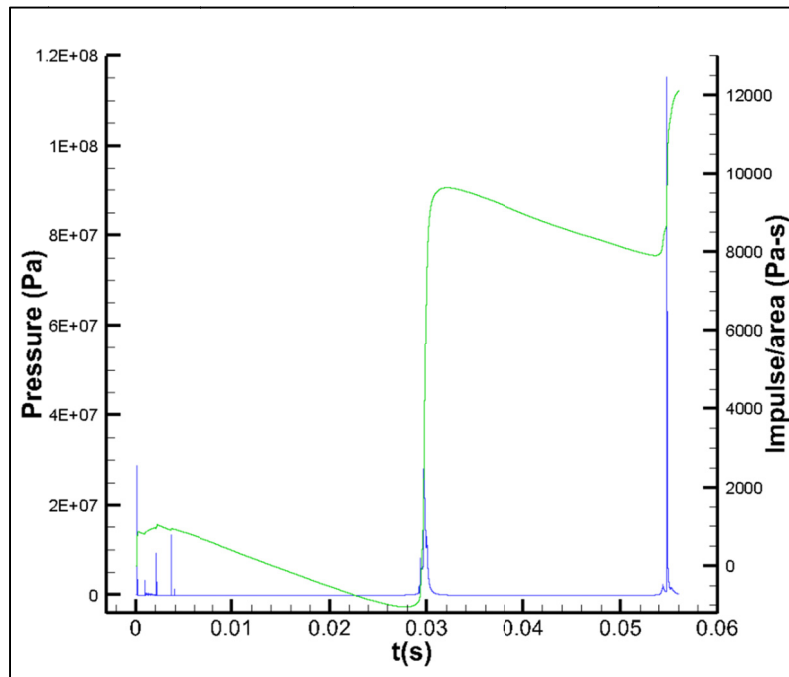
Figure 28: Pressure and impulse time histories at centre of target plate: rigid-free model, simulation RF-L.
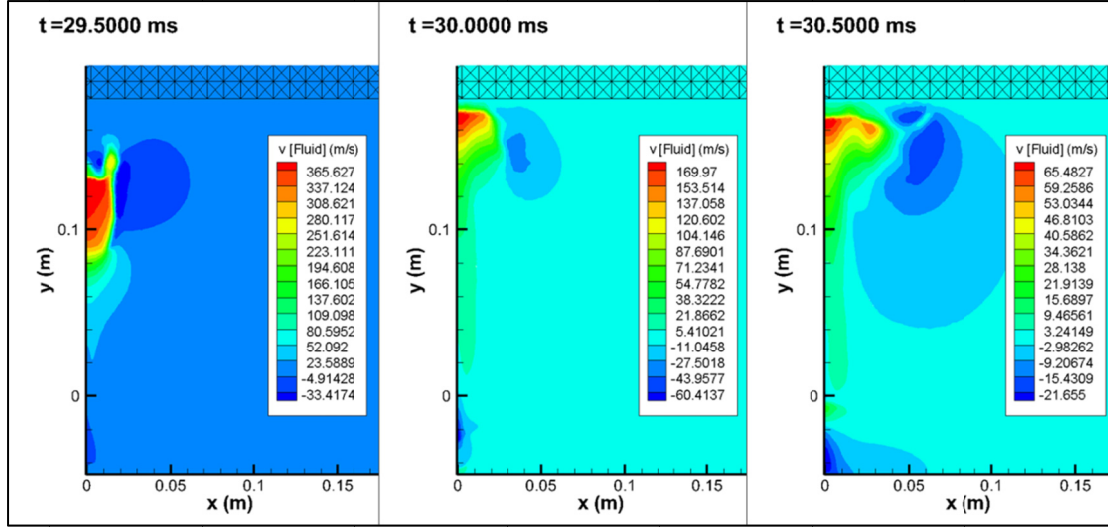
*Figure 29: Vertical (y) component of fluid velocity at first bubble collapse:
rigid-free target, simulation RF-L.*
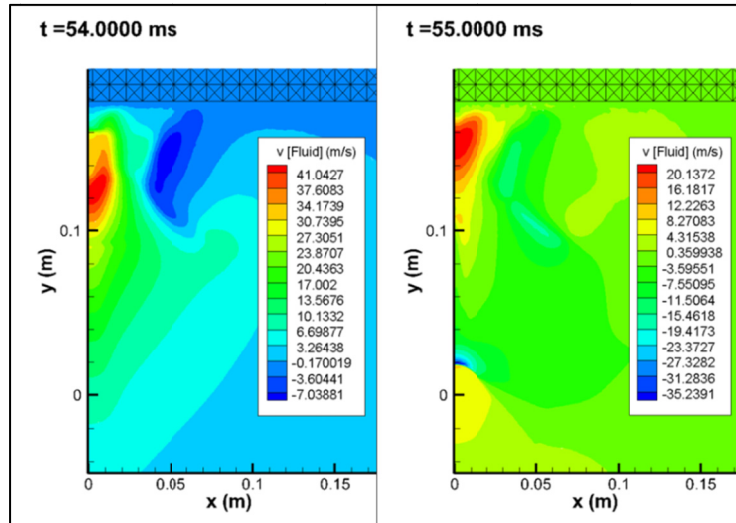
*Figure 30: Vertical (y) component of fluid velocity at second bubble collapse:
rigid-free target, simulation RF-L.*

The evolution of the gas bubble is shown in the density contour plots in Figure 31 and Figure 32. The gas bubble reaches maximum expansion at about 14.5 ms, at which time the horizontal radius is 0.1802 m and the vertical radius is 0.1705 m. The gap between the full expanded bubble and the target surface is about 30 mm. The target moves upward during bubble expansion and moves downward during bubble contraction. The first collapse of the bubble takes place at 29.71 ms. In the sequence of images in Figure 31, the bubble can be seen to collapse from the sides and from below, but the formation of a water jet is not as clearly apparent as it is for the rigid-fixed case. The bubble elongates vertically during collapse, and during the re-expansion phase shown in Figure 32, this elongated form re-emerges, along with a small toroidal structure next to the target surface. The second collapse occurs with a very high peak pressure (115 MPa) at 54.82 ms.
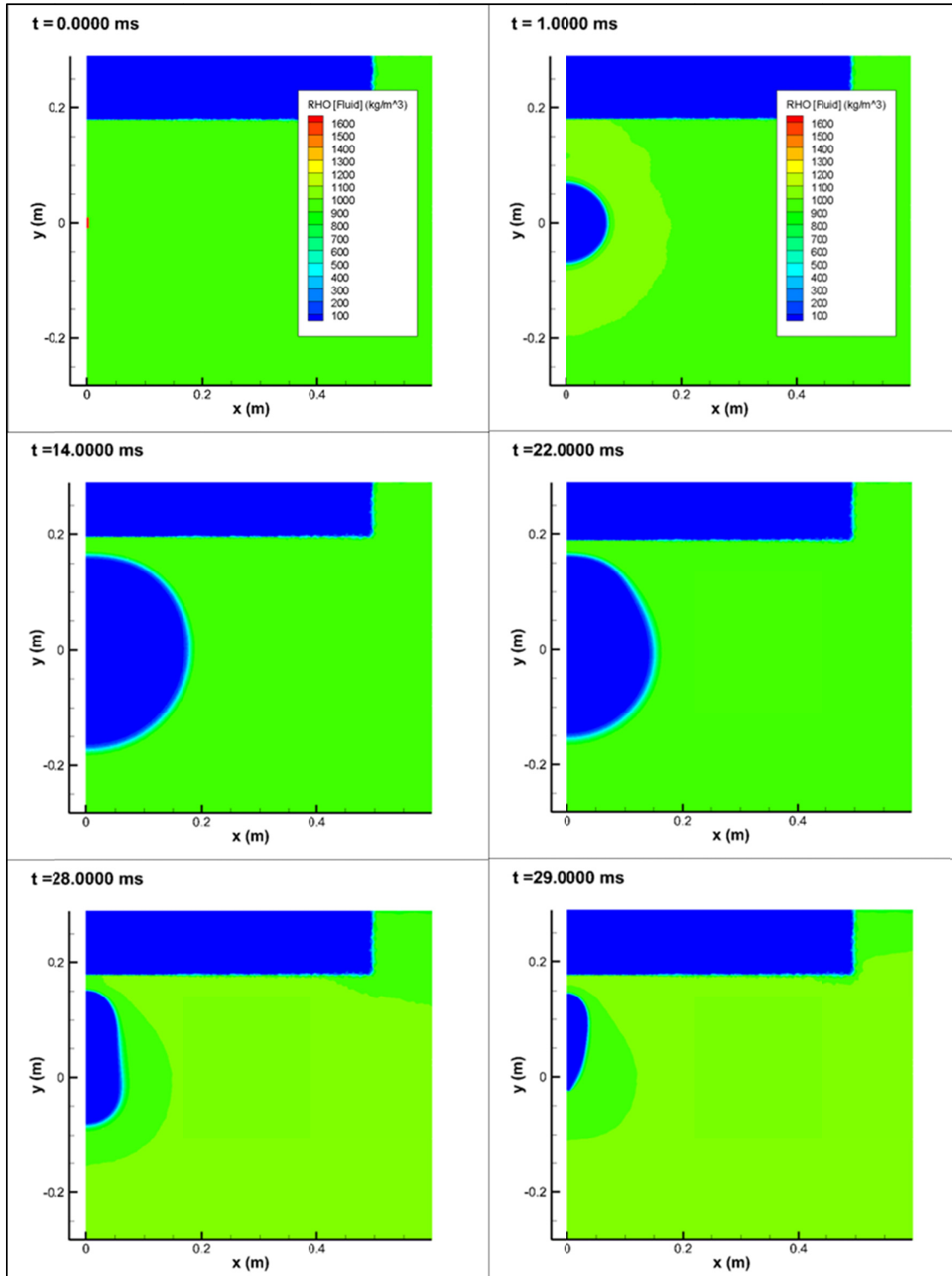
Figure 31: Progression of the gas bubble during first expansion and collapse: grid FS3 with rigid-free target, simulation RF-L.
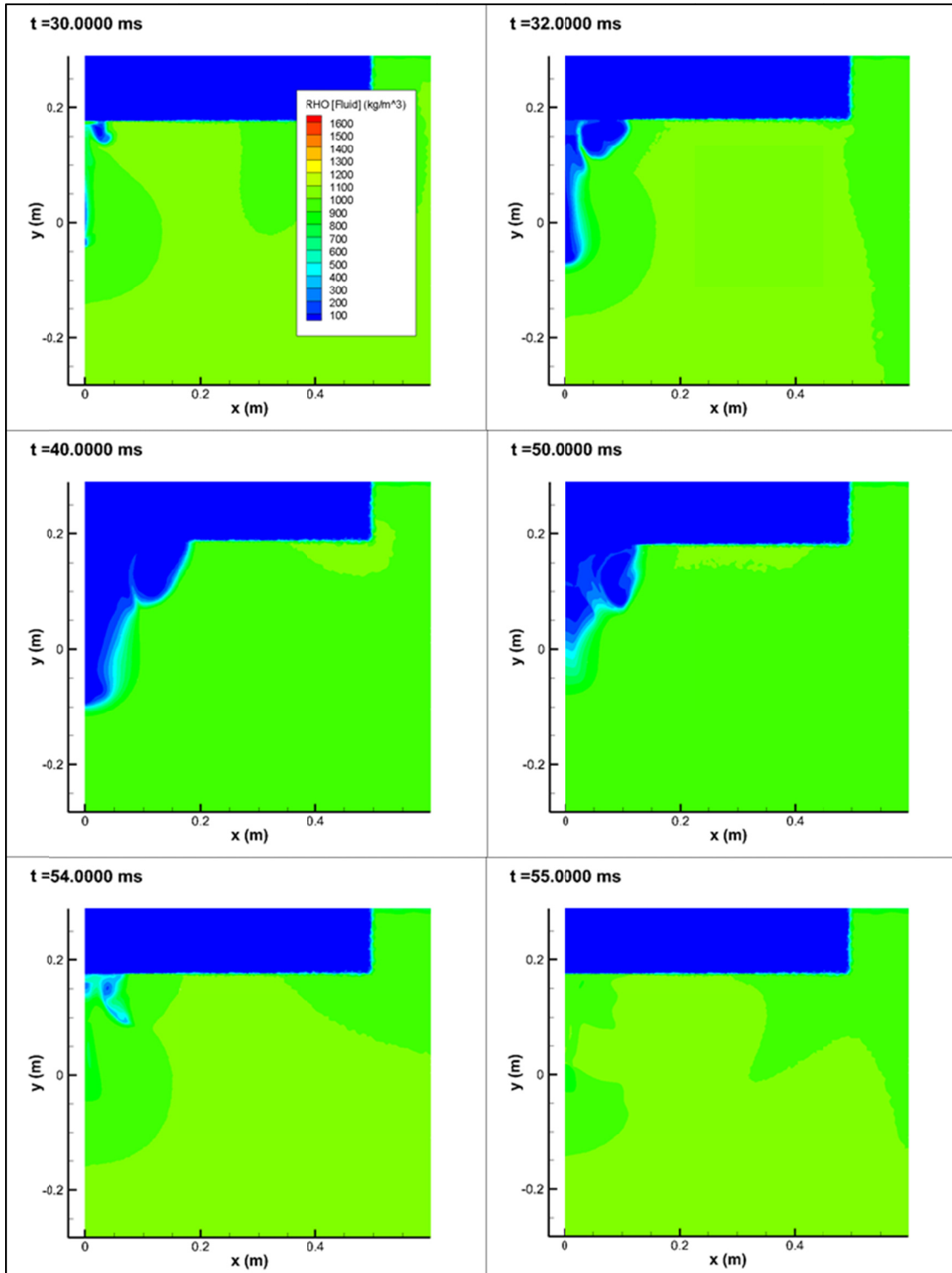
Figure 32: Progression of the gas bubble during second expansion and collapse: grid FS3 with rigid-free target, simulation RF-L.

The time history of the vertical (*y*) displacement at the centre of the plate is shown in Figure 33. Since the target is a rigid body, all nodes will have the same vertical displacement response. Two phases of the response are clearly identifiable: the first peak is due to the combined effect of the shock and the expanding bubble; the second peak is due to the bubble collapse. The displacement response is similar for the two coupling schemes, with the small-deflection coupling (RF-S) predicting a slightly larger displacement. This is consistent with the larger impulse loading seen for that simulation in Figure 27 and Figure 28.
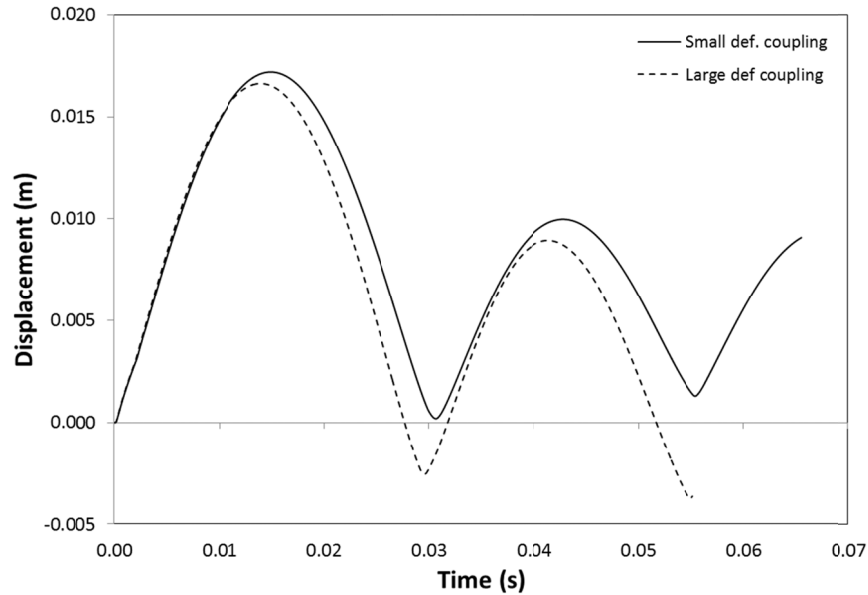
Figure 33: Displacement at the centre of the target plate: rigid-free case.

4.3.3   Fixed target model

In this case the top edge of the target cylindrical shell is fully restrained, and apart from the symmetry constraints the target plating is free to deform. The target model was coupled to the Chinook FS3 grid using both the small and the large deformation coupling scheme. The Chinook modelling parameters for the FS3 grid are identical to those used previously. A summary of the simulations performed is given in Table 15.

Table 15: Summary of 2D fixed target FSI simulations.

Name	Coupling	Chinook grid	Coupling interval (μs)	Simulation duration (ms)
FT-S	Small	FS3	0.5	54.13
FT-L	Large	FS3	0.5	15.28

The simulation with small deformation coupling was run until two collapse events were recorded. The fluid pressure time history at the two monitor points (Figure 34) shows that the pressure pulses due to bubble collapse are only visible at the lower monitor point. There, the first bubble pulse is recorded at 25.95 ms, and the second pulse at 44.85 ms. The peak shock pressure is similar at both monitoring locations. The pressure history on the surface of the plate (Figure 35) shows a number of large peaks which are not associated with the bubble collapse pulses. The density contour plots (Figure 36 and Figure 37) show that the bubble jets downward, away from the target. This is similar to the free surface simulations and is consistent with the shorter bubble period. Furthermore, large areas of cavitation form just below the target plate, starting at about 18 ms and persisting until nearly 34 ms. The closure of this cavitation region may be associated with the large pressure peaks seen at 34 ms in Figure 35.
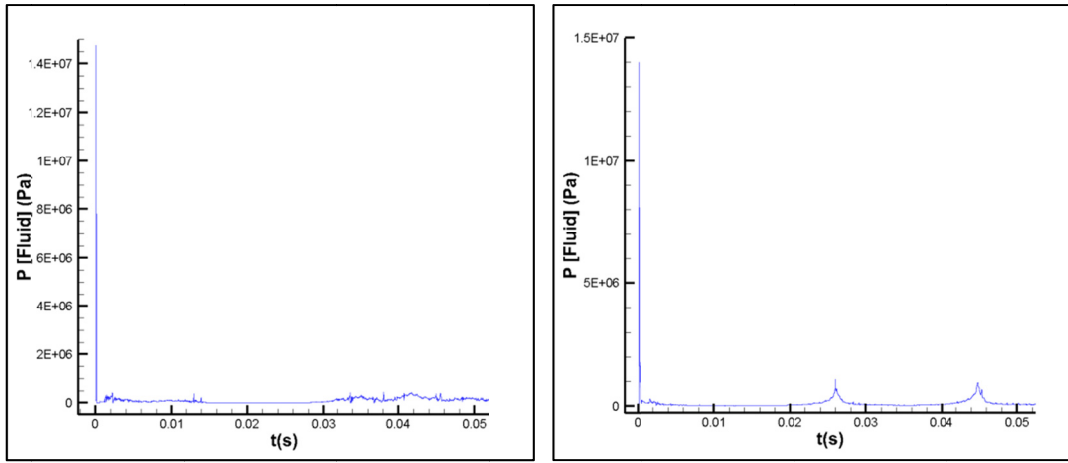
Figure 34: Pressure time histories at the upper (left) and
lower (right) monitoring points: simulation FT-S.
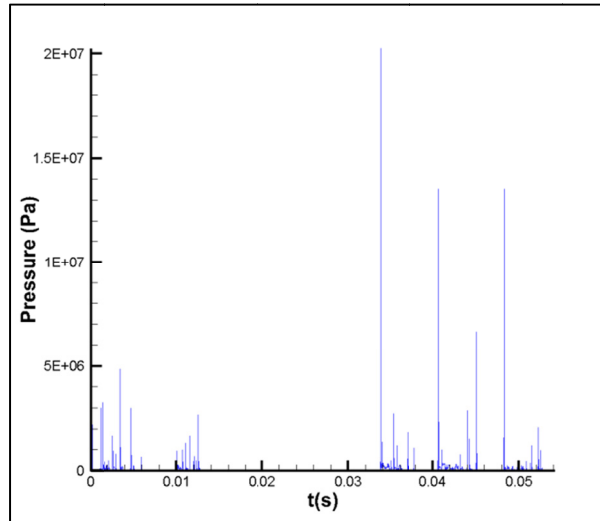
Figure 35: Pressure time histories at the centre of the target plate:
points: simulation FT-S.

Figure 36: Progression of the gas bubble during first expansion and collapse: simulation FT-S.
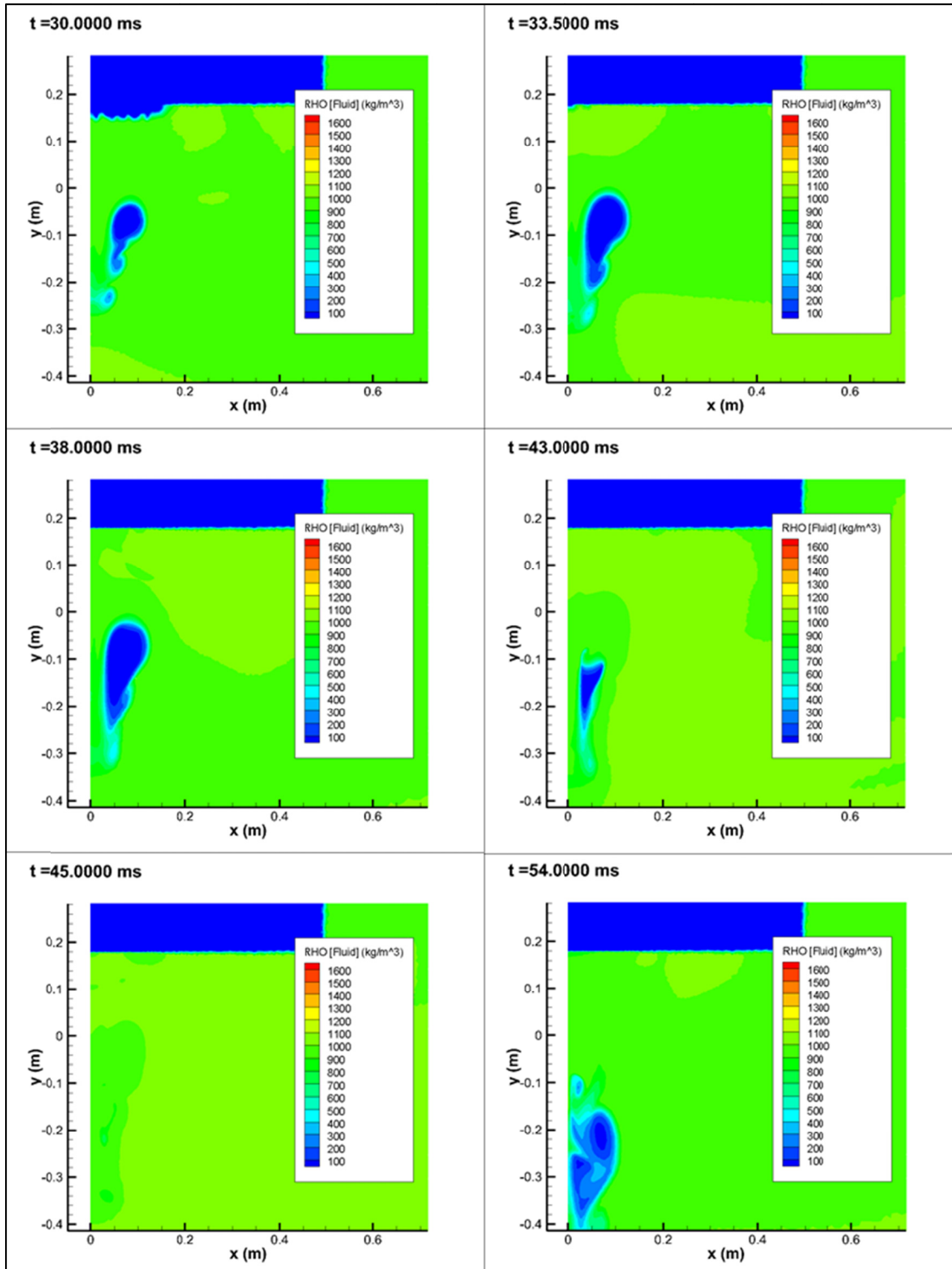
*Figure 37: Progression of the gas bubble during second expansion
and collapse: simulation FT-S.*

Figure 38 shows the fluid pressure at 7 ms after detonation, when the bubble is nearing maximum expansion, and shows the cavitation region between in the bubble and the target plate that appears and persists when the bubble is near maximum expansion. The simulation in Figure 38 was performed with a cavitation pressure fraction (α_c) set to 0.05 (i.e., the pressure at which cavitation occurs is 0.05 atm or about 5000 Pa). Two subsequent simulations were run with smaller values of α_c to determine if this affects the cavitation region. The colour scales in Figure 38 and Figure 39 have been adjusted so that the cavitating region always appears as dark blue. As indicated, the extent of the cavitation is little affected by α_c.
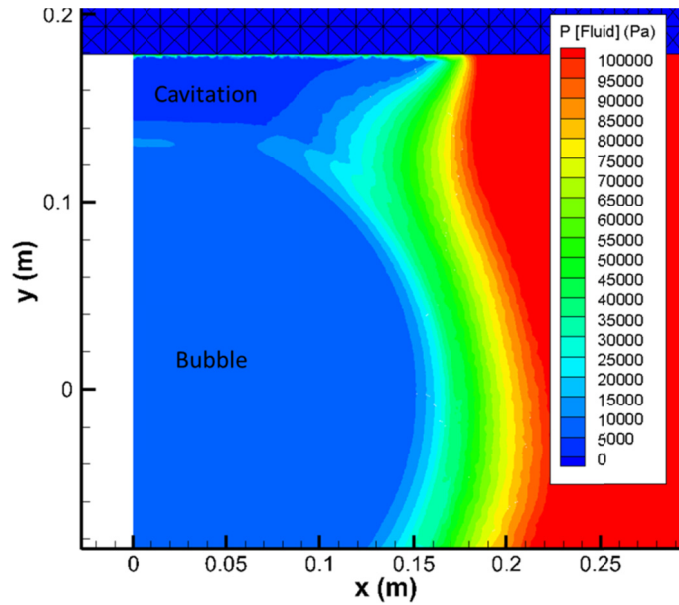
Figure 38: Pressure contours at t=7 ms, α_c = 0.05.
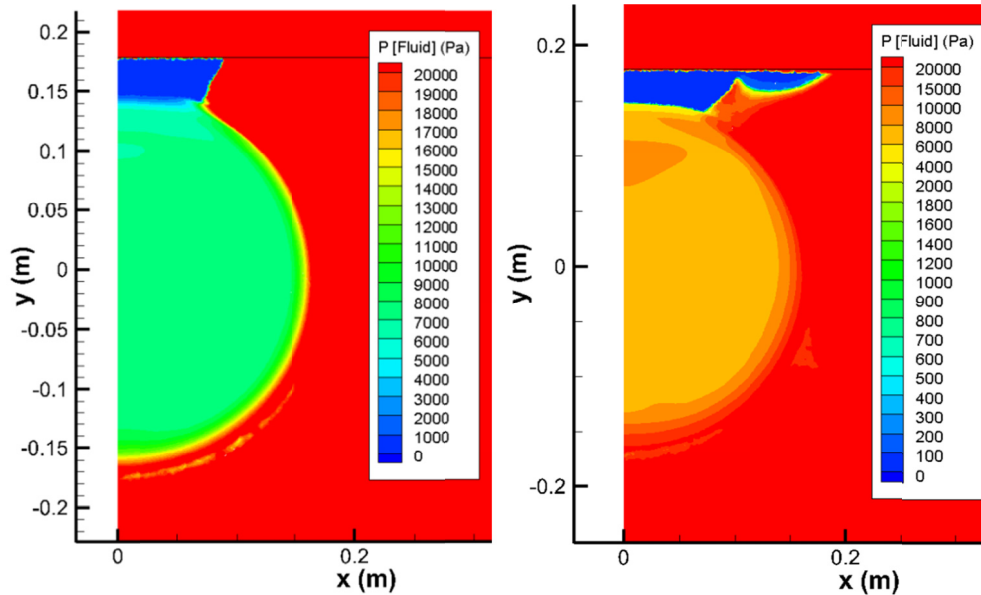
Figure 39: Pressure contours at t=7 ms: α_c= 0.01 (left); α_c = 0.001 (left).

The displacement at the centre of the bubble plate is shown in Figure 40. This figure compares the plate response predicted with the two coupling methods and shows that they are very close. Based on this comparison, it can be concluded that small deflection coupling is sufficient for predicting the shock response in this case. Differences in the gas bubble loading and response between the two coupling methods cannot be determined, however, due to the premature termination of FT-L simulation at 15.28 ms. The reasons for the premature termination, could not be determined. Neither LS-Dyna or Chinook produced an error message. Both applications remained active, but the simulation did not advance further than 15.28 ms.
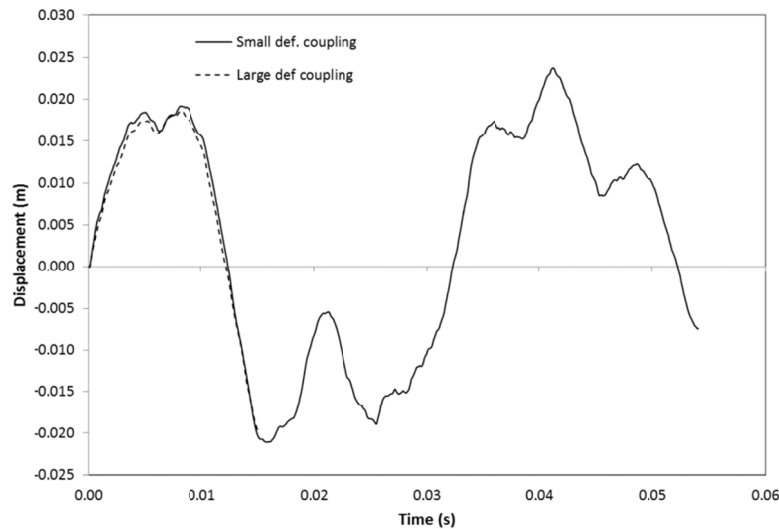
Figure 40: Normal displacement at the centre of the target plate: fixed target.

4.3.4   Free target model

In this case the target model was completely unrestrained except for the symmetry constraints. As with the rigid-free target model, a gravity load was applied to the target model during the LS-Dyna analysis to balance the hydrostatic forces acting on the partial submerged target. Four different coupled simulations were attempted, as summarized in Table 16. All three of the large deformation coupling runs terminated prematurely at the run times indicated in the table. The small deformation coupling simulation (T-S) terminated prematurely at 50.65 ms, which was long enough to capture the first bubble collapse event but not the second collapse.

Table 16: Summary of 2D free target FSI simulations.

Name	Coupling	Chinook grid	Coupling interval (µs)	Simulation duration (ms)
T-S	Small	FS3	0.5	50.65
T-L1	Large	FS2	0.5	12.55
T-L2	Large	FS3	0.5	12.33
T-L3	Large	FS4	0.5	12.58

The pressure time histories at the two monitor points are shown in Figure 41. The peaks due to the shock and the first bubble collapse have similar amplitudes. The first bubble collapse occurs at 29.26 ms, which is consistent with the free surface simulation. The peak bubble collapse pressure at the centre of the target plate (Figure 42) is considerably higher than the free field. Also note that the impulse per unit area imparted to the target by the bubble collapse is about 10,000 Pa-s, which is comparable to the rigid-free case (Figure 27 and Figure 28).
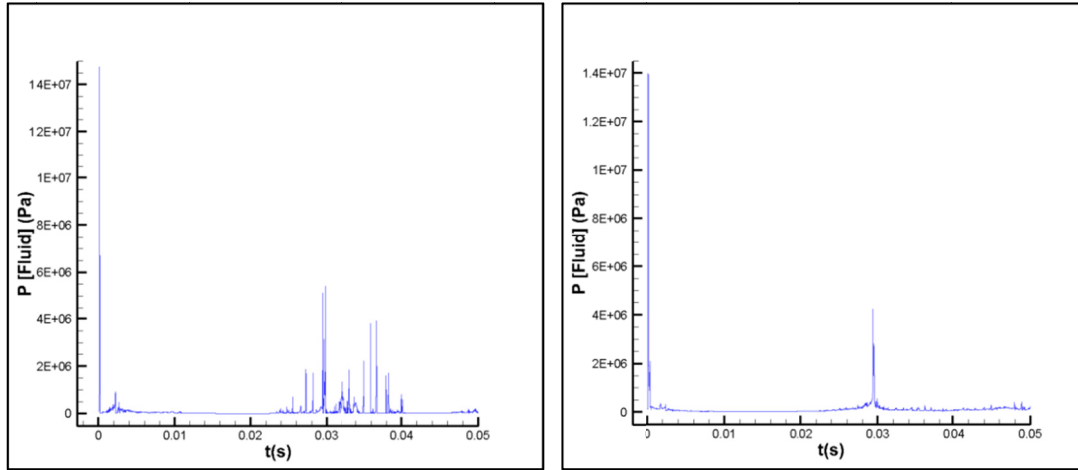
Figure 41: Fluid pressure at two monitoring points for simulation T-S: upper (left); lower (right).
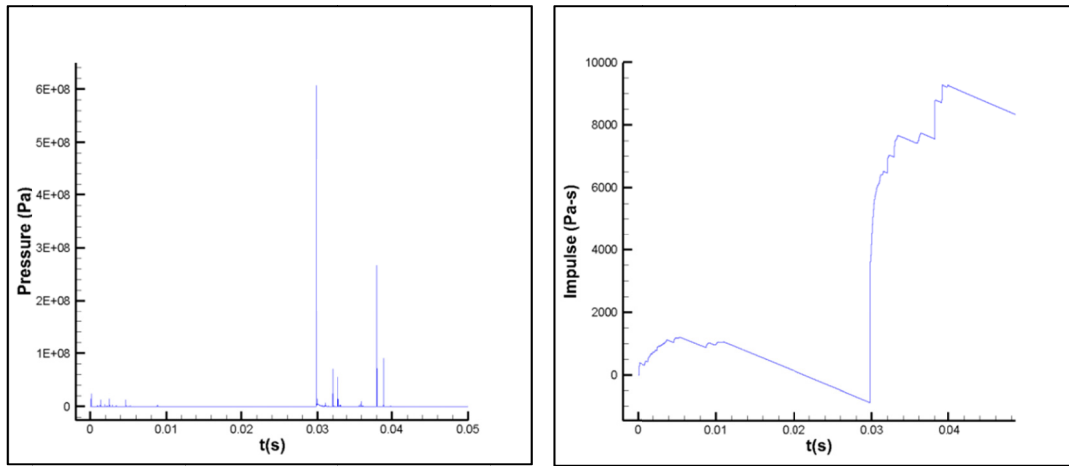
Figure 42: Pressure (left) and impulse per unit area (right) recorded at the centre of the plate for simulation T-S.

Density contour plots for simulation T-S are given in Figure 43 and Figure 44. These show that shortly after bubble reaches maximum expansion (15 ms), a gaseous region, which is likely cavitation, develops just under the target surface, and the bubble begins to collapse from above. A clearly defined water jet develops from above and fully penetrates the bubble by 27 ms. The bubble reaches a minimum at 29.5 ms, at which time the cavitation region near the target is approaching closure. The bubble then re-expands in an elongated and distorted shape. By 48 ms, a second collapse has begun and a cavitation region near the target plate has reappeared.
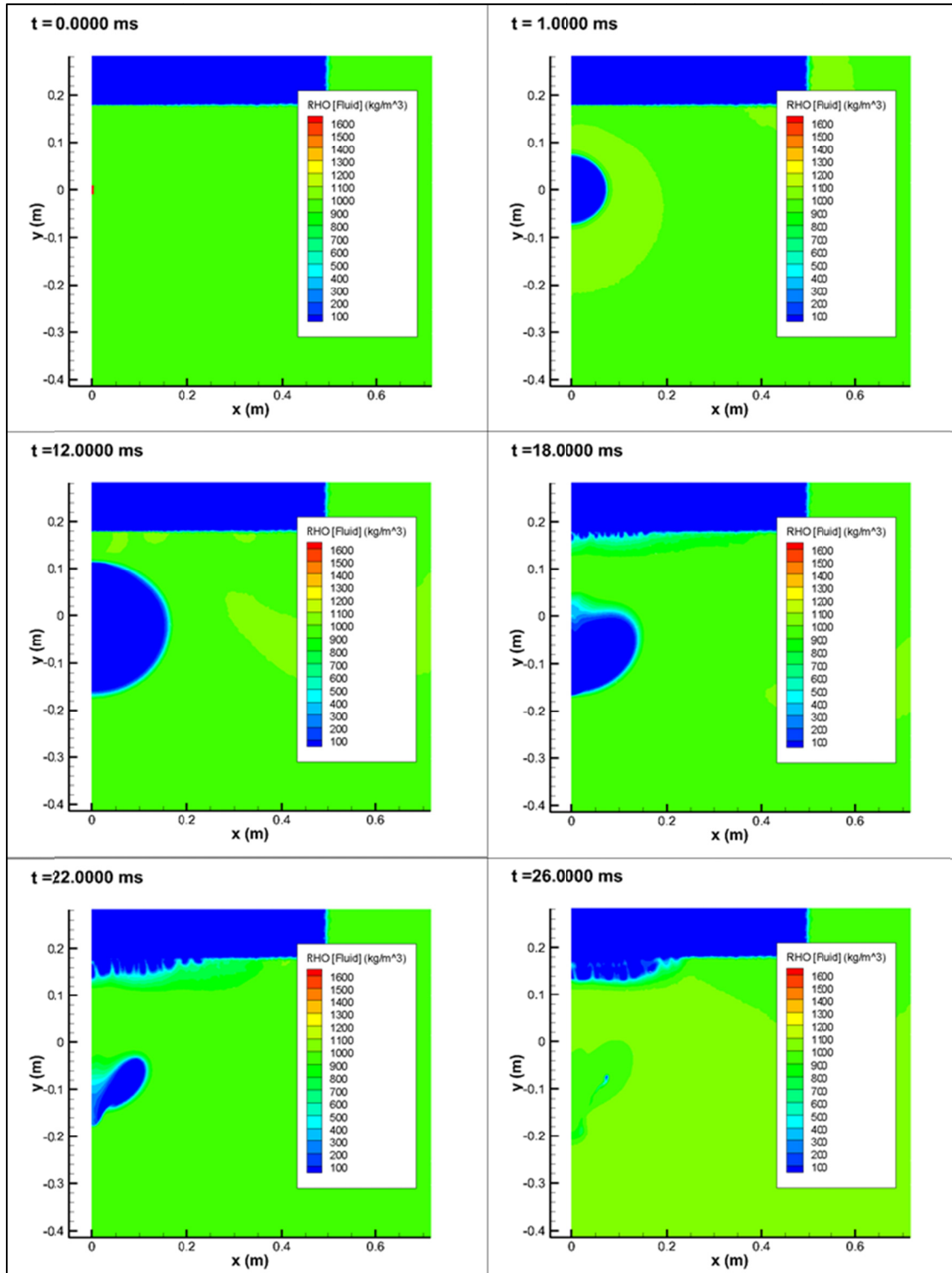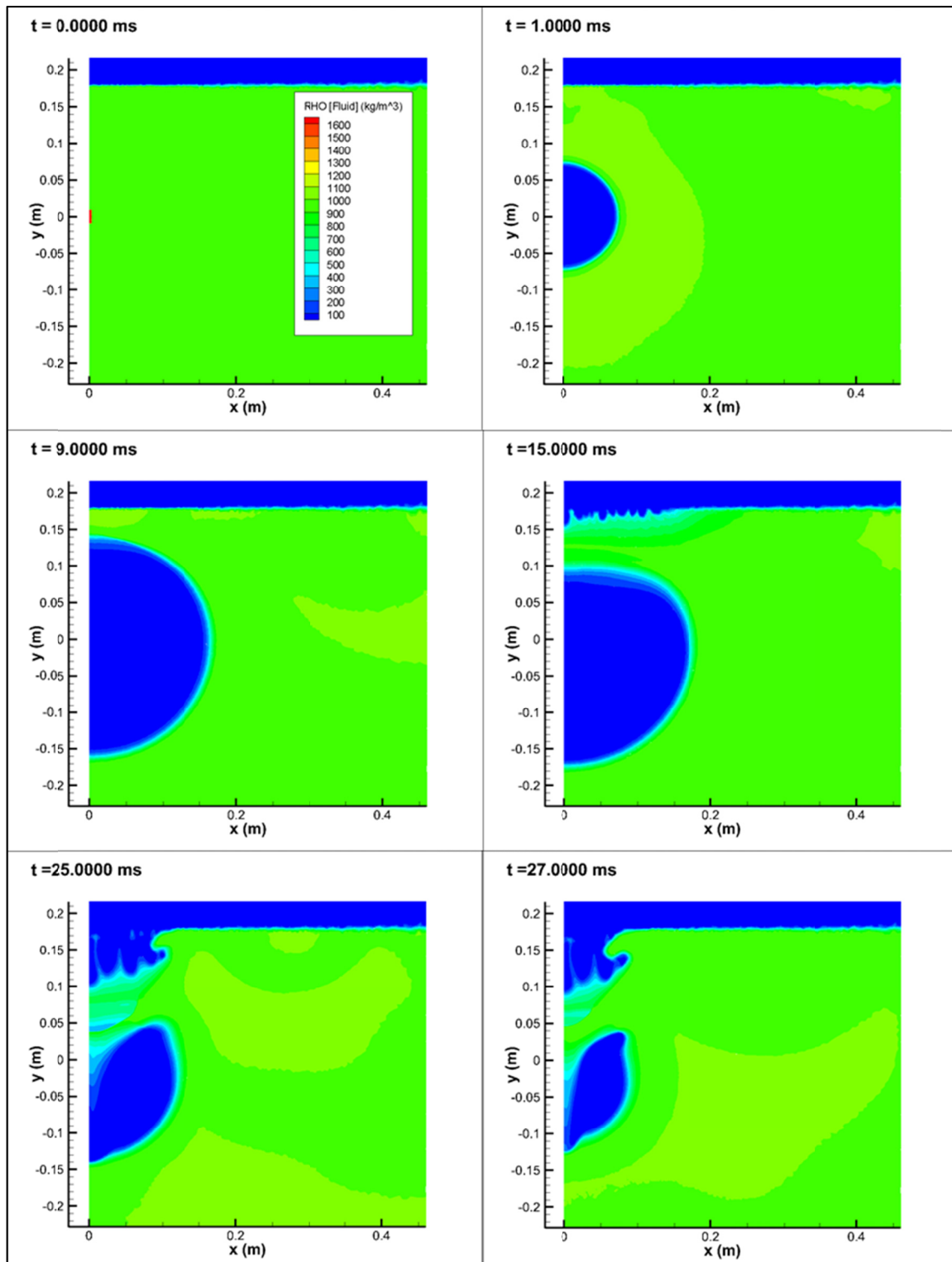
Figure 43: Progression of the gas bubble during first expansion and collapse: simulation T-S.
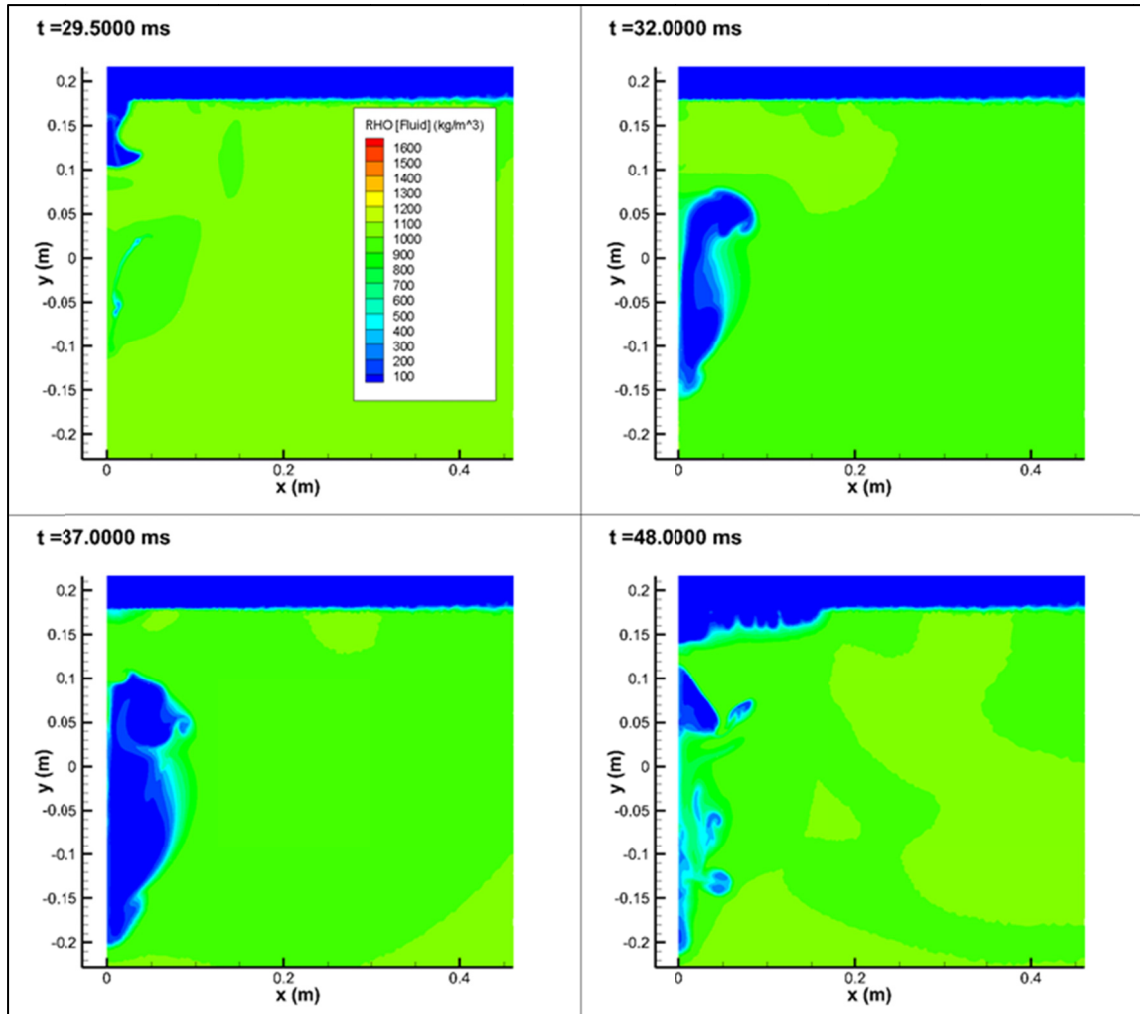
Figure 44: Progression of the gas bubble after first collapse: simulation T-S.

The displacement at the plate centre is shown in Figure 45. This figure compares the results of simulation T-S and the large deformation coupling simulations T-L2. The displacements over the first 12 ms are very similar and it can be concluded that large deformation coupling is not needed, at least for predicting the early-time response to the shock wave.
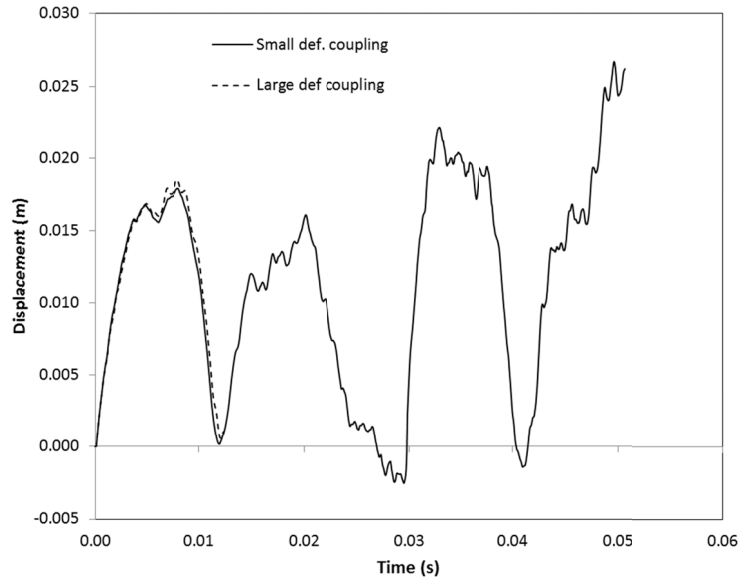
Figure 45: Vertical displacement at the centre of the target plate: free target.

4.3.5 Summary

Table 17 summarizes the first bubble pulse radius and period results in four FSI simulations. With the exception of the rigid-free case, the bubble radius is predicted with much less accuracy than was obtained in the free surface simulations. Much greater variability in the bubble period occurs in the FSI simulations as well. For the rigid-fixed case, the period is much longer than expected, while in the fixed case it is much shorter. It is expected that the presence of the target alters both the radius and period from the free surface values in a more consistent manner than observed in these simulations. The behaviour of the gas bubble overall seems to be very sensitive to the amount of restraint and rigidity of the target, since all other modelling parameters are identical.

Table 17: Summary of the properties of the first bubble pulse in 2D FSI simulations.

Case	Coupling	A_{1x}(m)	A_{1y} (m)	A_1/A_1^*	T_1 (ms)	T_1/T_1^*
Rigid-fixed	Small	0.1795	0.1620	0.964	34.97	1.208
Rigid-free	Small	0.1819	0.1681	0.988	30.64	1.058
Rigid-free	Large	0.1802	0.1705	0.990	29.59	1.022
Fixed	Small	0.1632	0.1483	0.879	25.83	0.892
Free	Small	0.1656	0.1511	0.894	29.26	1.010

5   3D benchmark cases

5.1   Free-field models

These models are similar to the 2D free field models but have been extended to three dimensions, with the basic layout shown in Figure 46. The *xy*, *xz* and *yz* coordinate planes are all planes of symmetry so that only 1/8th of the explosive charge and the surrounding fluid domain are modelled.
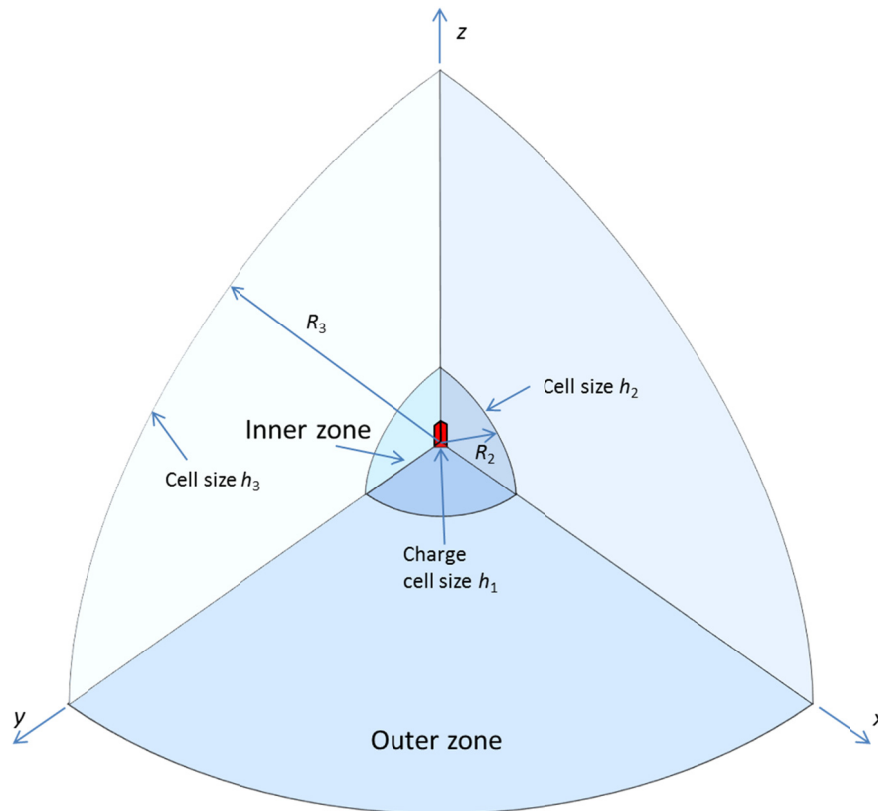
Figure 46: 3D free field model dimensions and cell size definitions.

Grids are generated with the Pointwise software, and these are then exported to CFD++ format from which they are converted to Chinook format. Similar to the gridding procedure used for the 2D models, grid sizes are specified for the charge, and for the outer boundaries of the inner and outer zones. Unstructured gridding methods are used with tetrahedral grid cells throughout the fluid volume, and with a smooth variation in the cell size from the origin to the outer boundary. An example grid is shown in Figure 47.

With this approach, three grids were generated using the cell size parameters given in Table 18. The total number of cells in FF3-1 was too large to analyse (estimated run time is about 1 month). However, simulations were carried out using grids FF3-2 and FF3-3. The run time for FF3-2 was six days and four hours.
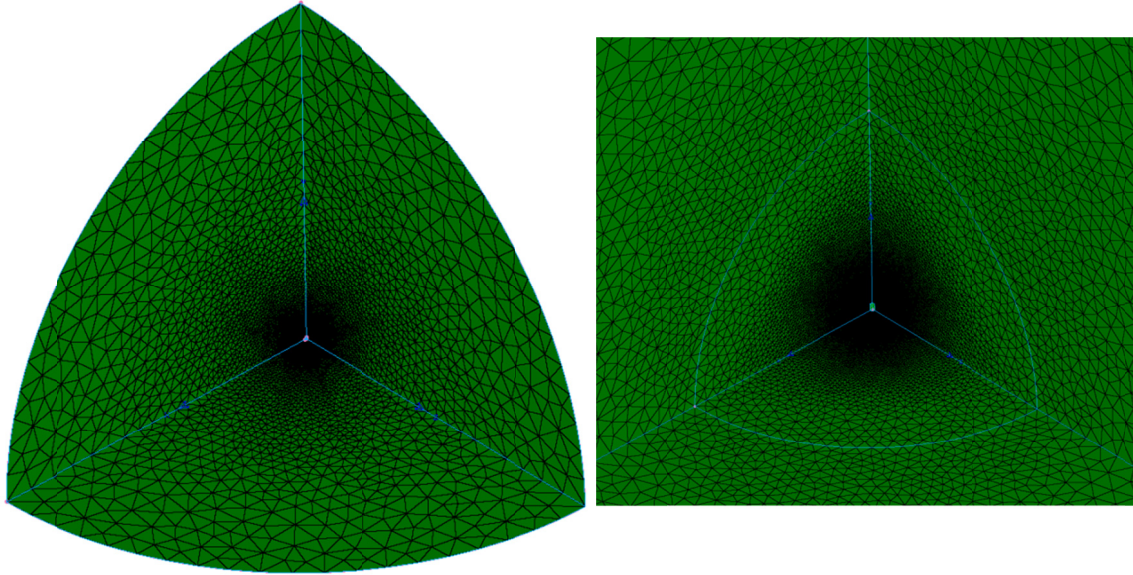
Figure 47: 3D free field grid FF3-3 showing the outer zone (left) and inner zone (right).

Table 18: Summary of 3D free field grids.

Name	R_2 (m)	R_3 (m)	h_1 (mm)	h_2 (mm)	h_3 (m)	No. cells
FF3-1	0.25	50	0.5	4	4	6,494,985
FF3-2	0.25	50	0.5	8	4	2,269,646
FF3-3	0.25	50	0.5	16	4	1,264,047

Alternatively, 3D models may be analysed by mapping the field variables from a simulation in a lower dimension to the 3D grid. In this way, a 3D simulation can be started a short time after detonation, when the shock wave has already travelled a distance and the bubble has partially expanded. This avoids the necessity of having to use very small cells in a 3D grid to prevent dispersion of the shock wave as it propagates through the fluid medium. Computationally this has the double advantage of a reduced number of cells and a smaller number of time steps.

Mapping to 3D is performed in Chinook using the *RESTART2 keyword. For mapping from 2D to 3D, Chinook automatically populates the 3D grid with the results of the 2D analysis. When the domains of the 2D and 3D grids are the same, this mapping occurs seamlessly in Chinook. Field variables in the 2D grid are swept about the axis of symmetry, thereby initializing the field variables in the 3D cells.

For the free field simulations presented here, the mapping is performed 1 ms after detonation using restart files generated for the 2D FF1 grid. The five restart grids used are listed in Table 19. The inner zone of the restart grid FFR-3 is shown in Figure 48, showing that a uniform cell size has been used throughout the inner zone.

Table 19: Summary of 3D free field restart grids.

Name	R_2 (m)	R_3 (m)	h_2 (mm)	h_3 (m)	No. cells
FFR-1	0.25	50	4	4	2,730,807
FFR-2	0.25	50	6	4	1,832,633
FFR-3	0.25	50	8	4	1,249,898
FFR-4	0.25	50	12	4	752,490
FFR-5	0.25	50	16	4	379,750
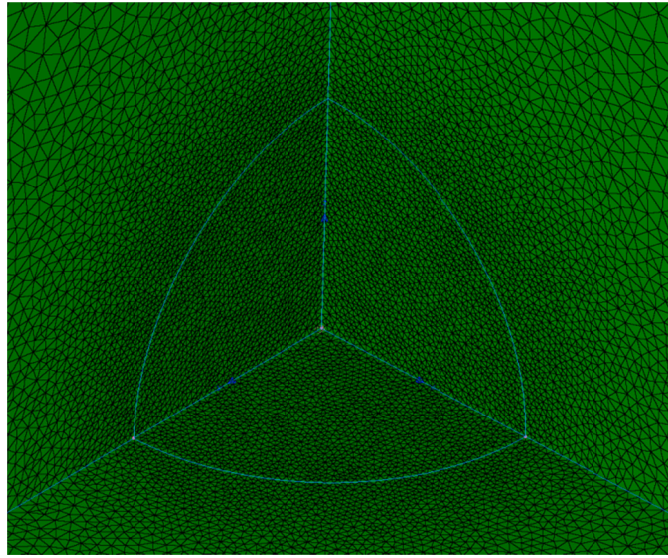
Figure 48: View of inner zone of the restart grid FFR-3.

Table 20 summarizes the maximum bubble dimensions and bubble period during the first bubble pulse. The results show that average gas bubble radius converges to within 2% of the empirical value for all of the restart grids. The bubble period is also predicted to within 2% for most of the restart grids. Slightly larger errors occur for the simulations that are started directly from detonation. Chinook's restarting capability appears to be effective for simulations of gas bubble pulsation, and results compare well with direct simulations in 3D. Furthermore, predictions of gas bubble pulsation are little improved with cell sizes smaller than 8 mm. More refined grids are needed when the propagation of the shock wave is to be simulated, however.

Table 20: 3D free field results for first bubble cycle.

Grid	Start time (ms)	A_{1x} (m)	A_{1y} (m)	A_{1z} (m)	A_1/A_1^*	T_1 (ms)	T_1/T_1^*
FF3-2	0	0.1741	0.171	0.1741	0.965	32.65	0.974
FF3-3	0	0.1717	0.1692	0.1719	0.956	32.49	0.969
FFR-1	1	0.1784	0.1746	0.1777	0.989	33.12	0.988
FFR-2	1	0.1783	0.1747	0.1777	0.989	33.12	0.984
FFR-3	1	0.1783	0.1746	0.1777	0.989	33.12	0.984
FFR-4	1	0.1780	0.1720	0.1766	0.981	32.95	0.979
FFR-5	1	0.1762	0.1741	0.1757	0.980	32.88	0.977

5.2   Free surface models

The configuration for 3D free surface models, shown in Figure 49, is an extension of the 2D free surface configuration used in Section 4.2. Explicit modelling of the explosive charge is omitted since, as was shown in Section 5.1, restart simulations gave adequate results.
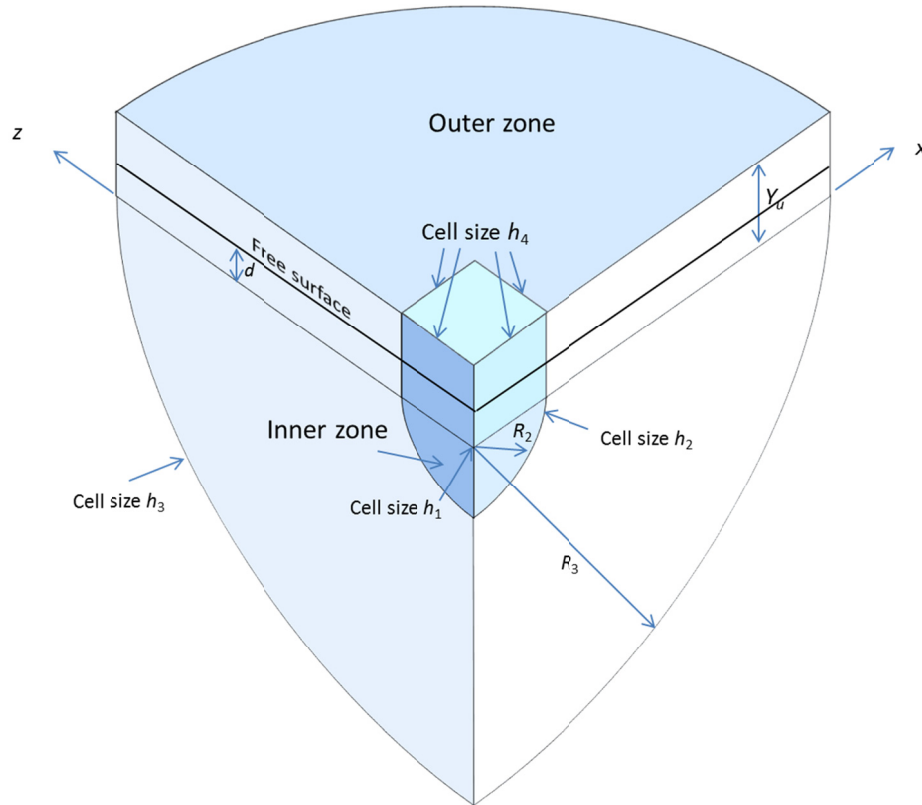
Figure 49: 3D free surface model dimensions and cell sizes.

Table 21 lists the restart grids created for the 3D free surface analyses using a procedure similar to the one described in Section 5.1. The grid refinement is controlled by the four cell sizes h_1, h_2, h_3, and h_4. The charge cell size h_1 controls the cell size at the original detonation point. Sometimes this will need to be different from h_2, even when mapping is used, as will be seen in the 3D FSI simulations. The outer boundary of the inner zone is controlled by the cell size h_2 and by h_4 at the upper surface. In the outer zone, the cell size transitions from between h_2 to h_4 on the inner boundary to h_3 on the outer boundary. The free surface is located a distance d above the centre of the charge. The FS3-2 grid is shown in Figure 50. The FS3-1 and FS3-2 grids are very similar except for the value of cell size parameter h_1.

Table 21: Summary of 3D free surface models.

Grid name	R_2 (m)	R_3 (m)	Y_u (m)	d (m)	h_1 (mm)	h_2 (mm)	h_3 (m)	h_4 (mm)	No. cells
FS3-1	0.25	50	1.0	0.3	2	8	4	40	2,223,618
FS3-2	0.25	50	1.0	0.3	8	8	4	40	2,001,290
FS3-3	0.25	50	1.0	0.3	12	12	4	40	1,258,533
FS3-4	0.25	50	1.0	0.3	16	16	4	40	685,707
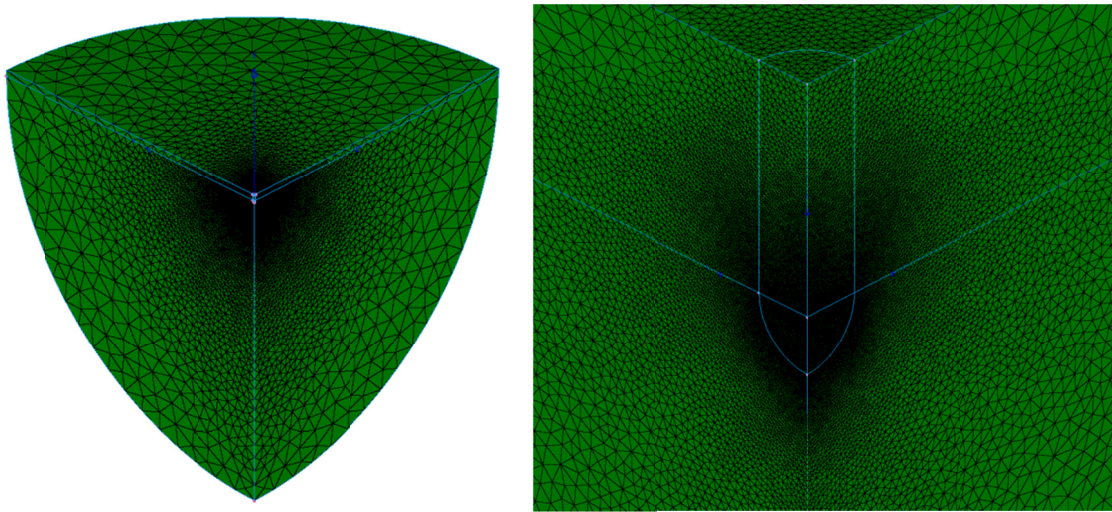
Figure 50: 3D free surface grid FS3-2 (left); view of inner zone (right).

The 3D simulations conducted with the above grids are listed in Table 22, which gives the grid, the simulation start time (when mapping from 2D to 3D is performed), and the total duration of the simulation. Simulation 0.1-1 took approximately 4 days to run using 30 cores on an IBM multicore server.

The reason for using the more refined FS3-1 grid with the 0.1 ms start time (i.e., Simulation 0.1-1) is illustrated in Figure 51. This shows the nascent gas bubble for two of the 3D grids, just at the moment that mapping has been performed and the 3D simulations begun. At this time, the gas bubble is still quite small. With grid FS3-1, the radius of the nascent gas bubble is spanned by about 11 cells, giving satisfactory resolution of the bubble; whereas with grid FS-2, the radius is spanned by only 3 or 4 cells, resulting in much less satisfactory resolution.

Table 22: Summary of 3D free surface simulations.

Simulation	Grid name	Start time (ms)	Duration (ms)
0.1-1	FS3-1	0.1	59.77
0.1-2	FS3-2	0.1	65.5
0.1-3	FS3-3	0.1	65.5
1.0-1	FS3-2	1	57.2
1.0-2	FS3-3	1	65.5
1.0-3	FS3-4	1	65.5
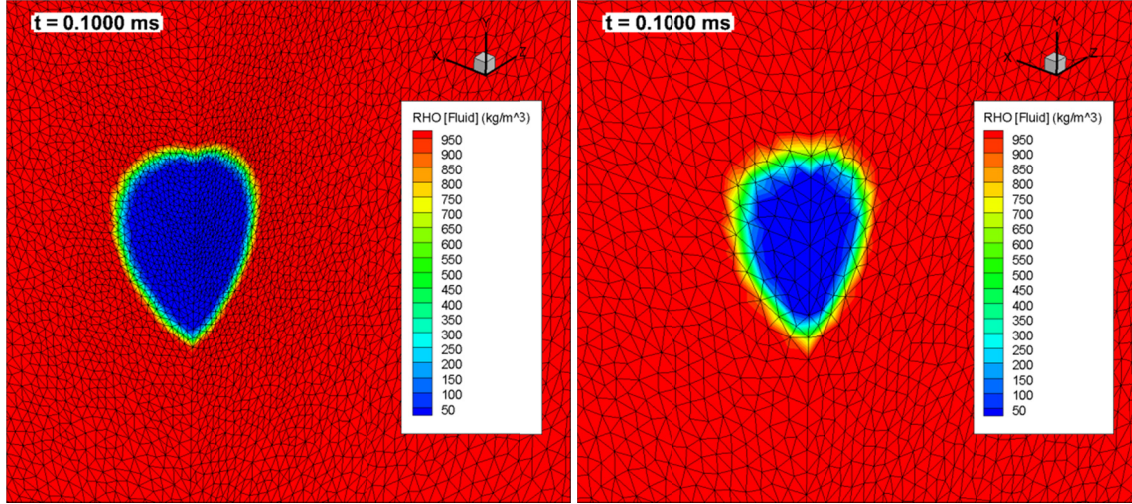
Figure 51: Density contours at the time of mapping to 3D: grid FS3-1 (left); grid FS3-2 (right).

Table 23 summarizes the maximum bubble dimensions and bubble period during the first bubble pulse. The results show that for all simulations with mapping at 1 ms, the average gas bubble radius converges to within 2% of the empirical value. When mapping is performed at 0.1 ms, a slight reduction in bubble radius and period occurs. However, this is not significant when a sufficiently small cell size h_1 is used, as in grid FS3-1. The bubble period agrees well with the empirical value with the surface correction factor, and the first pulse period is consistent with bubble periods predicted in the 2D axisymmetric case (Table 11). Chinook's mapping and restart capability therefore appears to be effective for simulations of gas bubble pulsation near the free surface.

Table 23: 3D free surface results for the first bubble cycle.

Grid	A_{1x} (m)	A_{1y} (m)	A_{1z} (m)	A_1/A_1^*	T_1 (ms)	T_1/T_1^*
0.1-1	0.1759	0.1744	0.1755	0.990	28.94	1.003
0.1-2	0.1751	0.1730	0.1751	0.985	28.73	0.996
0.1-3	0.1717	0.1674	0.1700	0.958	28.26	0.980
1.0-1	0.1796	0.1766	0.1781	1.006	29.04	1.007
1.0-2	0.1783	0.1724	0.1769	0.993	28.87	1.001
1.0-3	0.1775	0.1737	0.1760	0.992	28.70	0.995

Results for the second bubble pulse are summarized in Table 24. The largest radius in the second pulse occurs for the 0.1-1 grid, where the bubble radius is about 76% of the first pulse radius, and where the period is about 90% of the first period. The second pulse radius and period are both larger than the empirical values, indicating that the energy losses predicted by Chinook are less than expected.

Table 24: 3D free surface results for the second bubble cycle.

Grid	A_{2x} (m)	A_{2y} (m)	A_{2z} (m)	A_2/A_1	A_2/A_2^*	T_2 (ms)	T_2/T_1	T_2/T_2^*	d_2 (m)
0.1-1	0.1371	0.1279	0.1357	0.762	1.070	26.07	0.901	1.229	0.440
0.1-2	0.1283	0.1248	0.1277	0.728	1.017	25.17	0.876	1.187	0.422
0.1-3	0.1179	0.1272	0.1167	0.711	0.966	23.51	0.832	1.108	0.395
1.0-1	0.1338	0.1203	0.1337	0.726	1.036	25.40	0.875	1.197	0.444
1.0-2	0.1254	0.1174	0.1245	0.696	0.981	24.16	0.837	1.139	0.429
1.0-3	0.1183	0.1195	0.1225	0.683	0.962	23.46	0.818	1.106	0.409

Figure 52 gives the pressure time history at the two monitor points for the 1.0-1 simulation, showing that the peak pressure is about 30% higher at the lower monitor point. Such differences could arise due to differences in the fineness of the grid around the two monitor points, but the slight downward migration of the bubble (about 75 mm at the time of the first collapse) also contributes as it moves the source of the pressure pulse closer the lower monitor point.
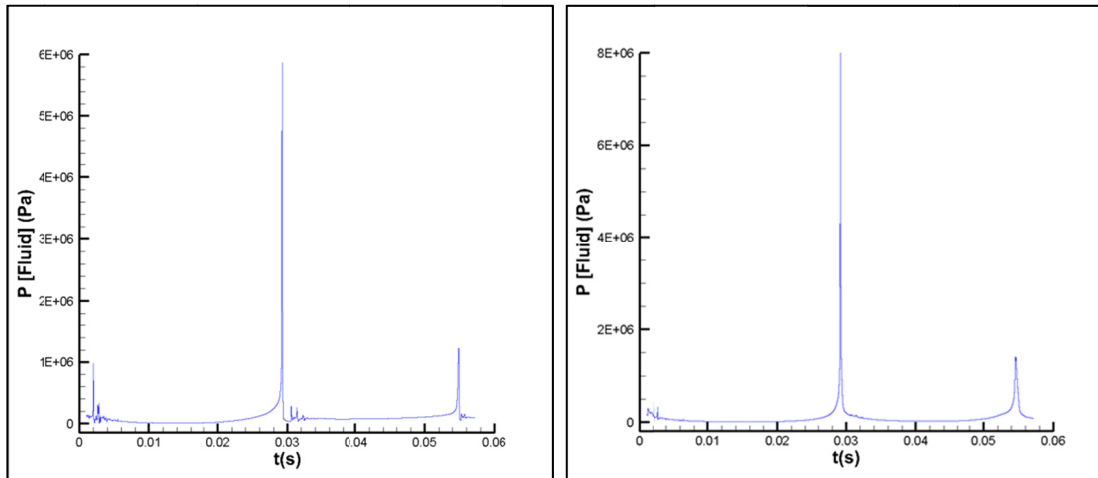
Figure 52: Fluid pressure at upper (left) and lower (right) monitor points, simulation 1.0-1.

Figure 53 shows the evolution of the gas bubble during the first bubble period. The results show the nearly spherical bubble collapsing to a point close to the original detonation point, where a downward directed water jet forms and downward migration occurs. The bubble rebounds in a toroidal form at a somewhat lower depth, as shown in Figure 54, and a second collapse follows at 54.5 ms. These results are very similar to the 2D axisymmetric case (Figure 17 and Figure 18).
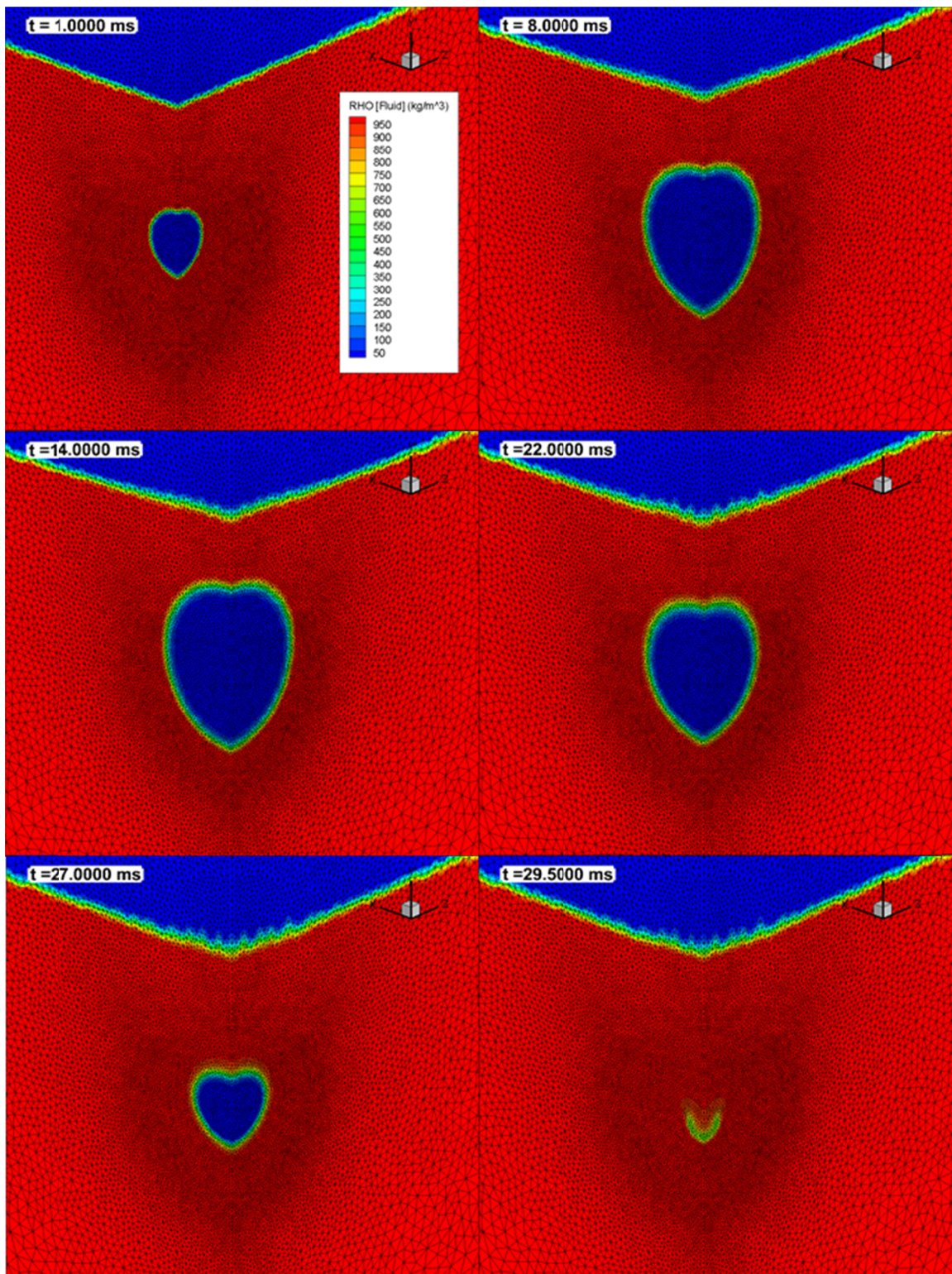
*Figure 53: Progression of the gas bubble up to first collapse: simulation 1.0-1.
Colours are density in kg/m³.*
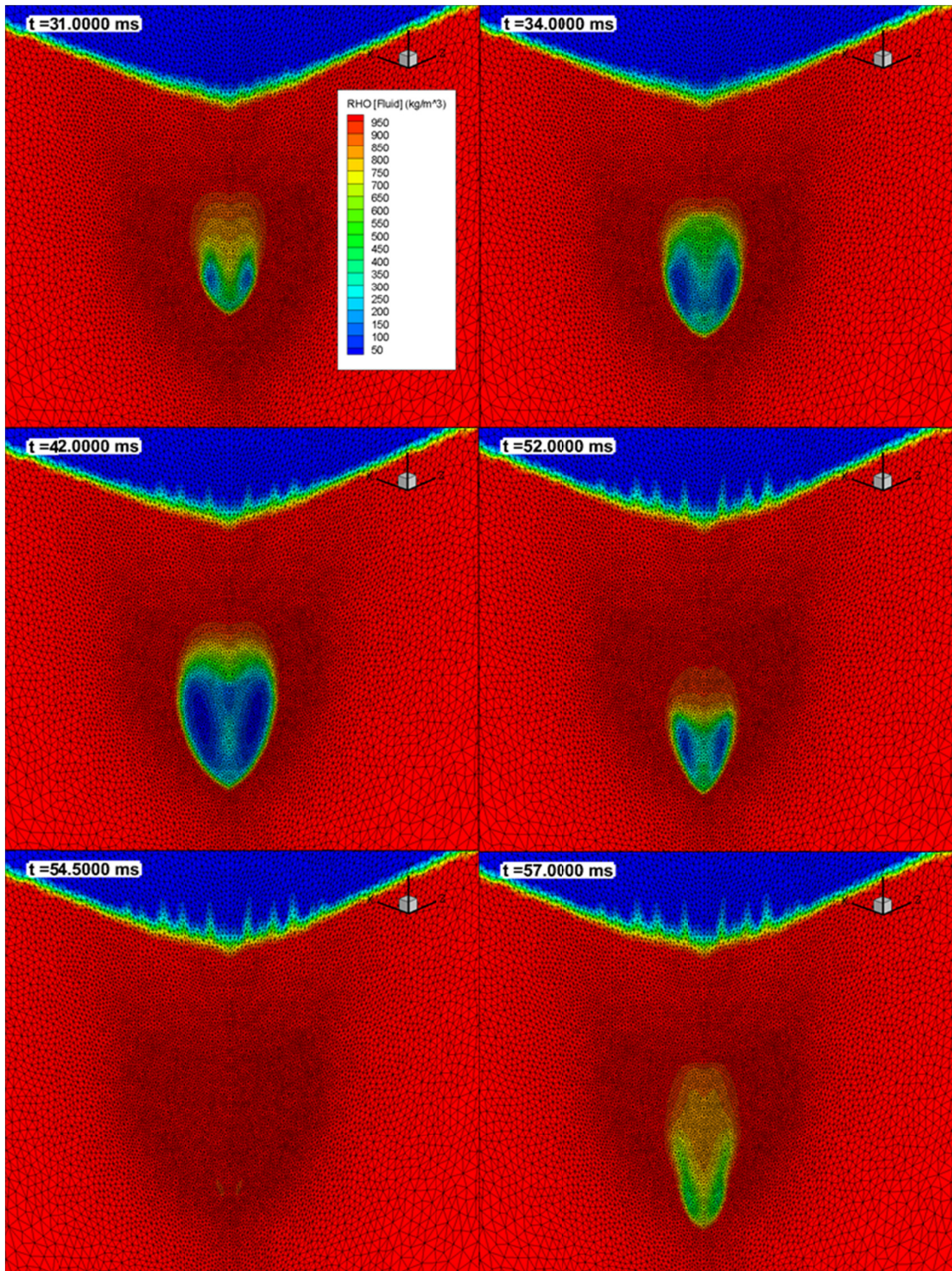
Figure 54: Progression of the gas bubble after first collapse: simulation 1.0-1. Colours are density in kg/m³.

5.3   3D FSI benchmark cases

For the 3D FSI benchmark cases, a 3D Chinook grid is coupled with the same target models used for the 2D FSI simulations in Section 4.3. The 3D FSI simulations are performed in restart mode, using mapping from a 2D simulation. The following limitations must be observed when using mapping in an FSI simulation.

– For a responding target, the mapping is limited according to the type of coupling used and the geometry of the target. With small deformation coupling, it is necessary to perform the mapping prior to any displacement or deformation of the target. Once the target model has displaced or deformed, the 3D analysis is restarted using the displaced or deformed position of the target model, while the field variables are mapped to the 3D model based on the undisplaced position of the target. This will create an incompatibility in the distribution of fluid and gas at the time of the mapping. To avoid this, the mapping must be done prior to the arrival of the shock wave at the target. For the 1.1 g charge at a standoff distance of 1R, this limits the mapping to occur at 0.1 ms or earlier.

– If large deformation coupling is used and the target geometry is axisymmetric, the mapping can be performed at any time, either from 2D to 3D or from 3D to 3D.

– If large deformation coupling is used and the target geometry is not axisymmetric, a 3D to 3D mapping can be performed at any time, but a 2D-to-3D mapping must be performed prior to the arrival of the shock wave at the target.

In this section, FSI simulations were performed for all four target models using small deformation coupling. For all of these simulations, the FS3-1 grid is used, in which the smallest grid cell size is 2 mm near the initial centre position of the gas bubble, and 8 mm near the outer boundary of the inner zone. The mapping is performed at 0.1 ms, just before the shock wave arrives at the target plate. The pressure contour plot in Figure 55 shows the shock wave at the time of mapping. FSI simulations were also attempted using large deformation coupling, but none of those simulations could be made to run past 4.5 ms. Some notes on this experience are recorded in Section 5.3.5.
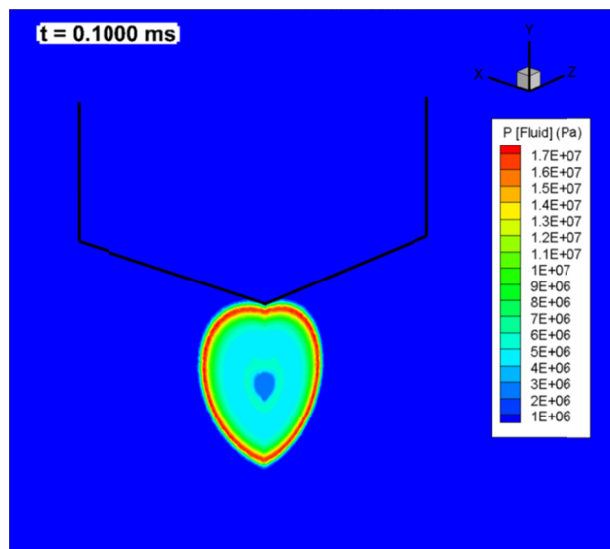
Figure 55: Pressure contours at the time of mapping to 3D with outline of target plate indicated.

5.3.1   Rigid-fixed target model

The target model is identical to the one used in Section 4.3.1. The FS3-1 grid is used with properties identical to those used in previous analyses. The mapping is performed using field variables determined with the 2D FS1 grid at the mapping time of 0.1 ms. The 3D coupled simulation (with small deformation coupling) was run for a total duration of 58 ms, which was long enough to record the first bubble collapse, but not long enough to record the second collapse. The model was run in parallel mode with 30 processors on an IBM multicore server. The simulation required nearly five days to run to completion.

The pressure and impulse time-histories at the centre of the target plate are shown in Figure 56. The shock and the bubble collapse pressure peaks have similar magnitudes, and are considerably higher than what was predicted in the corresponding 2D case (Figure 28). This is a surprising result given that some loss in resolution of the shock pressures can be expected when mapping to 3D. The impulse time-history shows that the impulse from the bubble collapse is considerably larger than that of the shock wave. The bubble collapse occurs at 34.67 ms, which compares with 34.97 ms in the 2D case. The fluid pressures at the upper and lower monitor points are shown in Figure 57. These are considerably lower than those seen on the target plate.
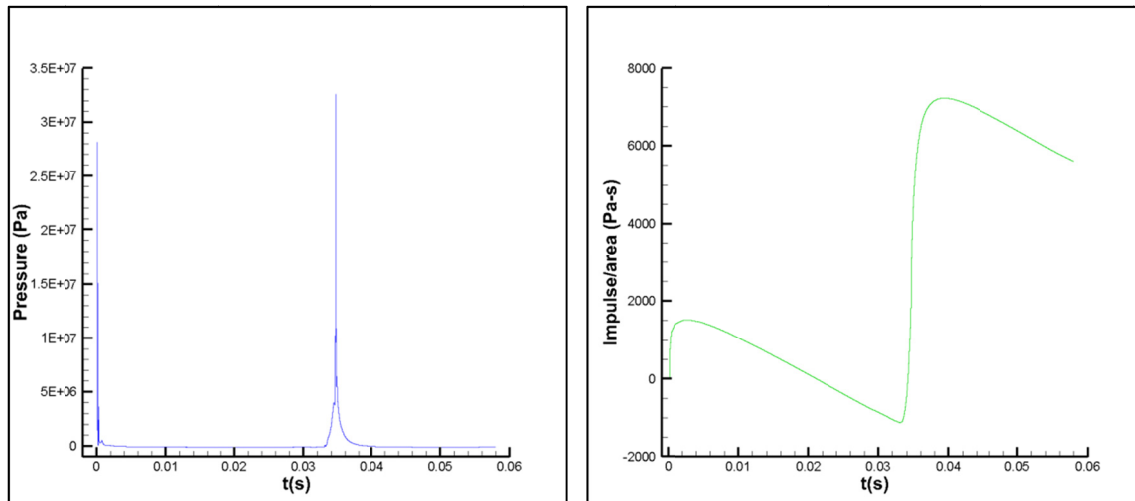
Figure 56: Time-histories at the centre of the rigid-fixed target plate:
pressure (left); impulse (right).

The sequence of contour plots in Figure 58 shows the evolution of the gas bubble up until first collapse. At maximum expansion (16.6 ms) the bubble does not reach the target plate. The average of the bubble radii on the three coordinate axes is 0.1685 m, or about 95% of the empirical value. The radius in the vertical direction is only 0.157 m, which is only 88% of the empirical value. Considerable reduction of the bubble radius is therefore seen compared to the corresponding free-surface case. Bubble collapse is towards the plate, and a bubble jet directed toward the target forms, with full penetration of the bubble occurring shortly after 34.1 ms. After the collapse, the bubble begins to re-form in a toroidal shape close to the target surface.
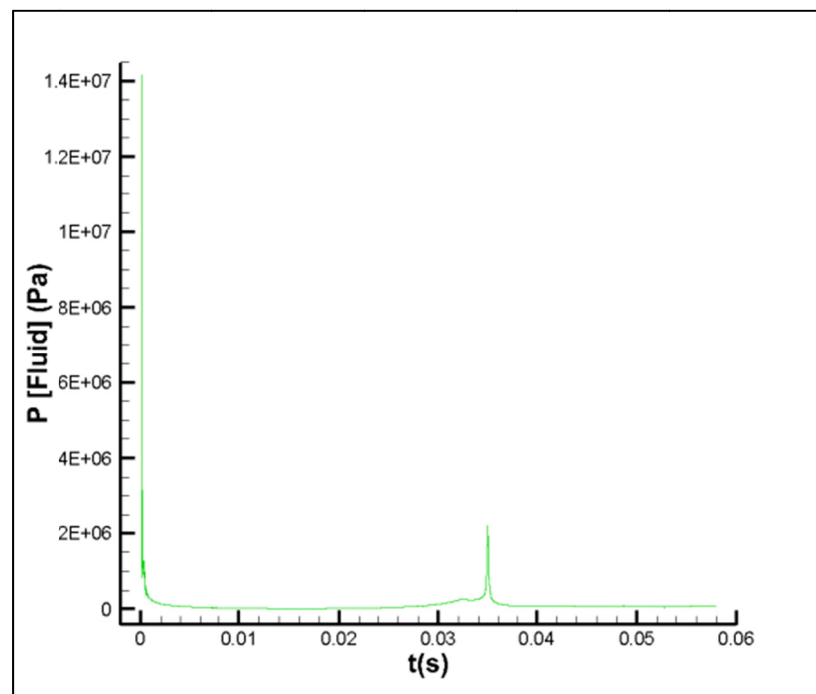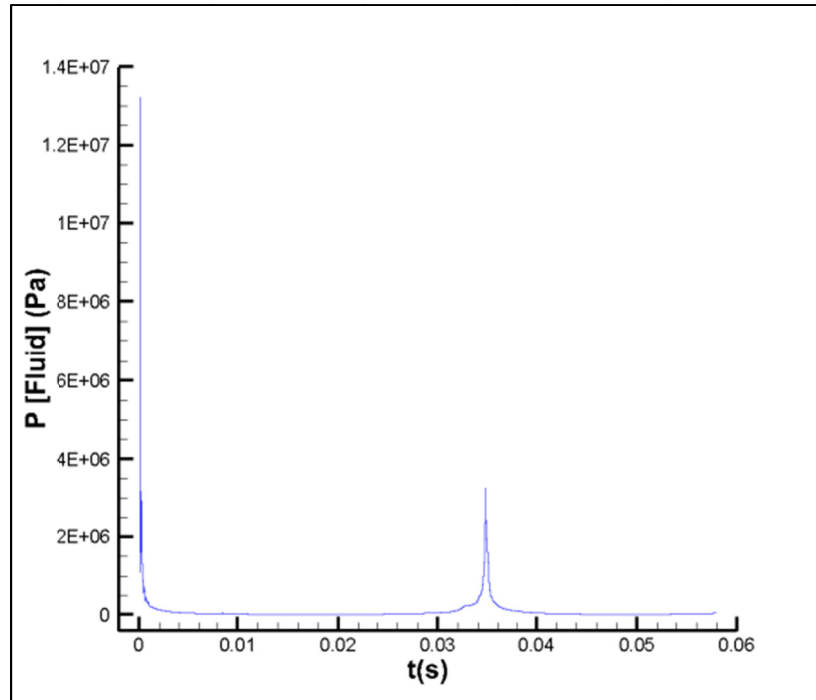
Figure 57: Pressure time-histories at the upper monitor point (top);
at the lower monitor point (bottom).
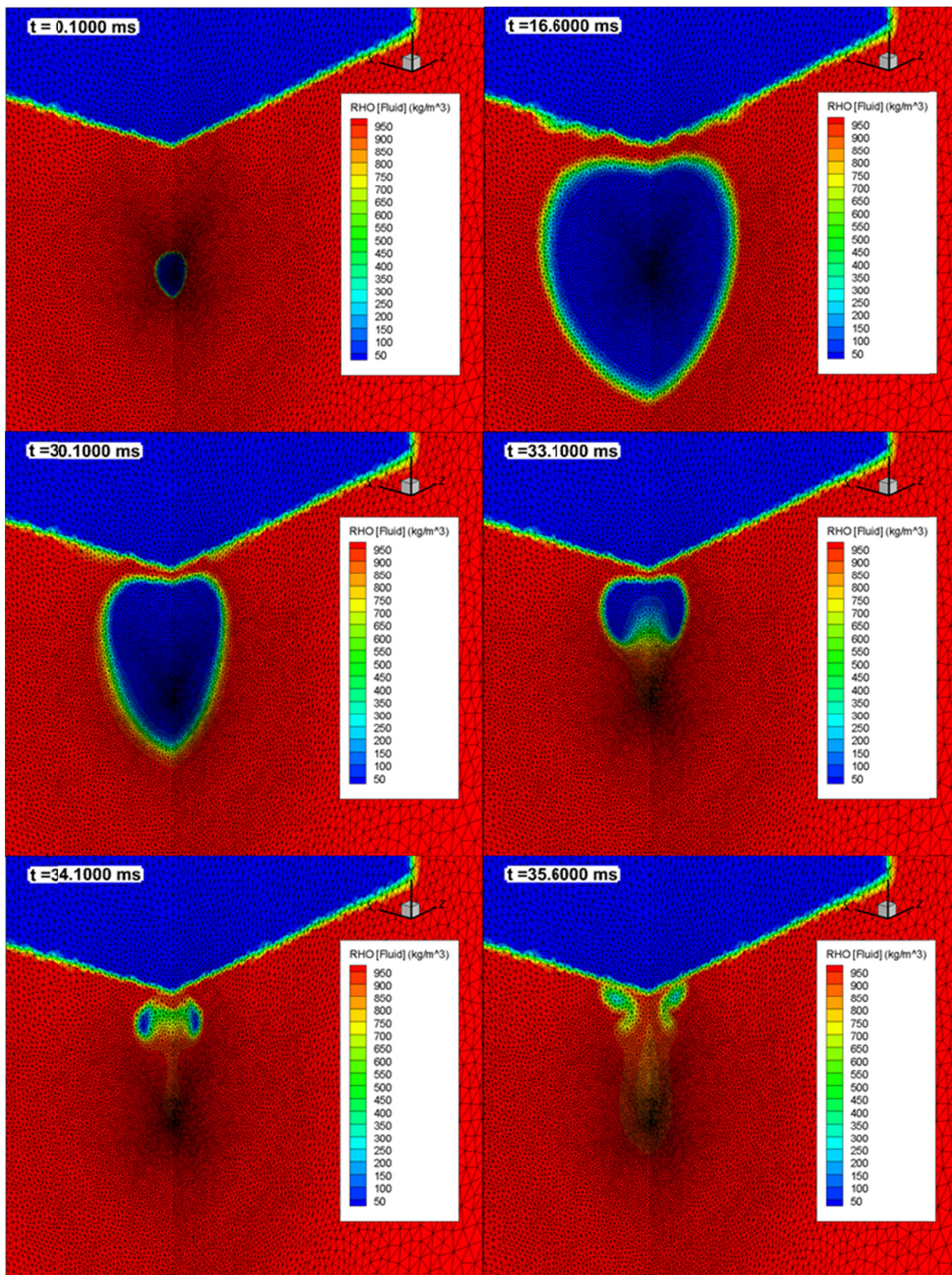
Figure 58: Progression of the gas bubble to first collapse: rigid-fixed target.

5.3.2   Rigid-free target model

The target model is identical to the one used in Section 4.3.2. The FS3-1 grid is used with properties identical to those used in previous analyses. The mapping is performed using field variables determined with the 2D FS1 grid at the mapping time of 0.1 ms. The 3D coupled simulation (with small deformation coupling) was run for a total duration of 65 ms, which was long enough to record the first and second bubble collapse.

The pressure and impulse time-histories at the centre of the target plate are shown in Figure 59. The shock and the bubble collapse pressure peaks differ somewhat from those seen in the corresponding 2D case (Figure 28). The change in impulse for the first and second bubble collapse is about 4000 Pa-s, while the total change in impulse over the two pulses is about 6500 Pa-s. This is roughly half the total change in impulse in the 2D case. The fluid pressures at the upper and lower monitor points are shown in Figure 60. The peak pressures are an order of magnitude lower than those seen on the target plate.
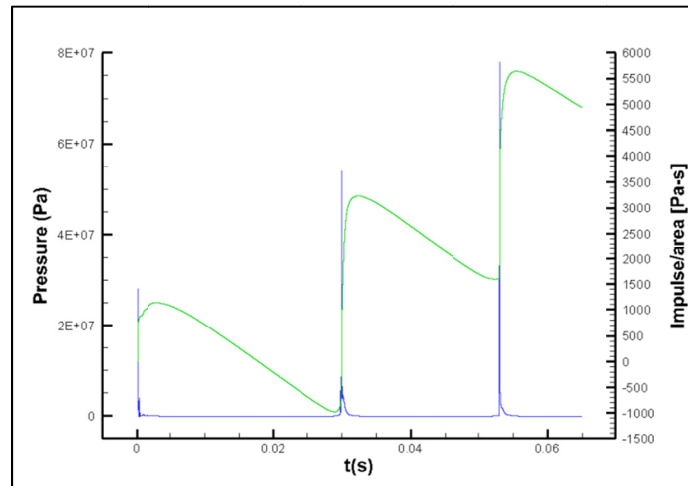
Figure 59: Pressure and impulse time histories at the centre of the rigid-free target plate.
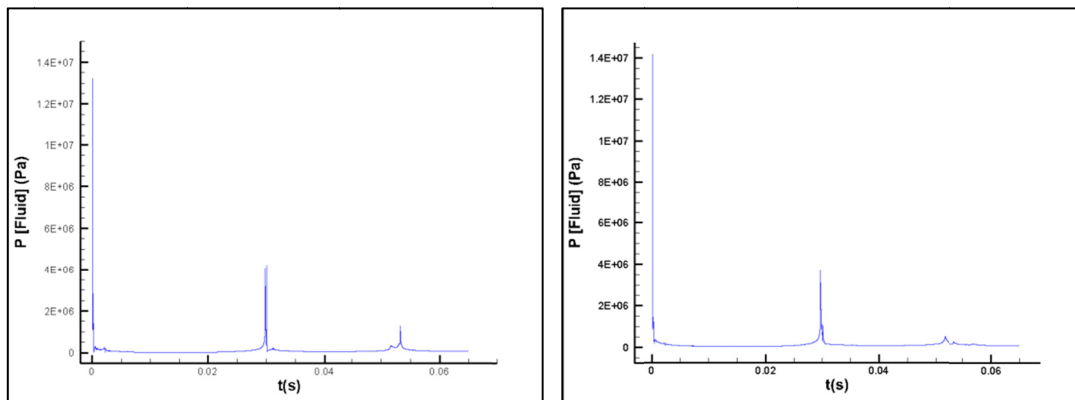
Figure 60: Field pressure time histories at monitor points for the rigid-free model:
upper (left); lower (right).

Two sequences of contours of the vertical component of the fluid velocity are given in Figure 61 and Figure 62, for the first and second bubble collapse, respectively. This shows the formation of the jets within 15 mm of the y-axis. The highest velocities occur at some distance from the plate, and diminish as the jet approaches the target plate. The sequence of contour plots in Figure 63 and Figure 64 shows the evolution of the gas bubble up to and beyond second collapse. It reaches maximum expansion at 15.6 ms, at which time the average of the bubble radii on the three coordinate axes is 0.173 m, or 96.7% of the empirical value; and the radius in the vertical direction is 0.166 m, or 92.6% of the empirical value. The bubble is therefore somewhat larger than what is predicted in the 3D rigid-fixed case; and it is only slightly less than what was predicted in the corresponding 2D case. During the first collapse, the bubble becomes highly elongated along the y-axis, and it maintains this form to some degree during the second pulse.
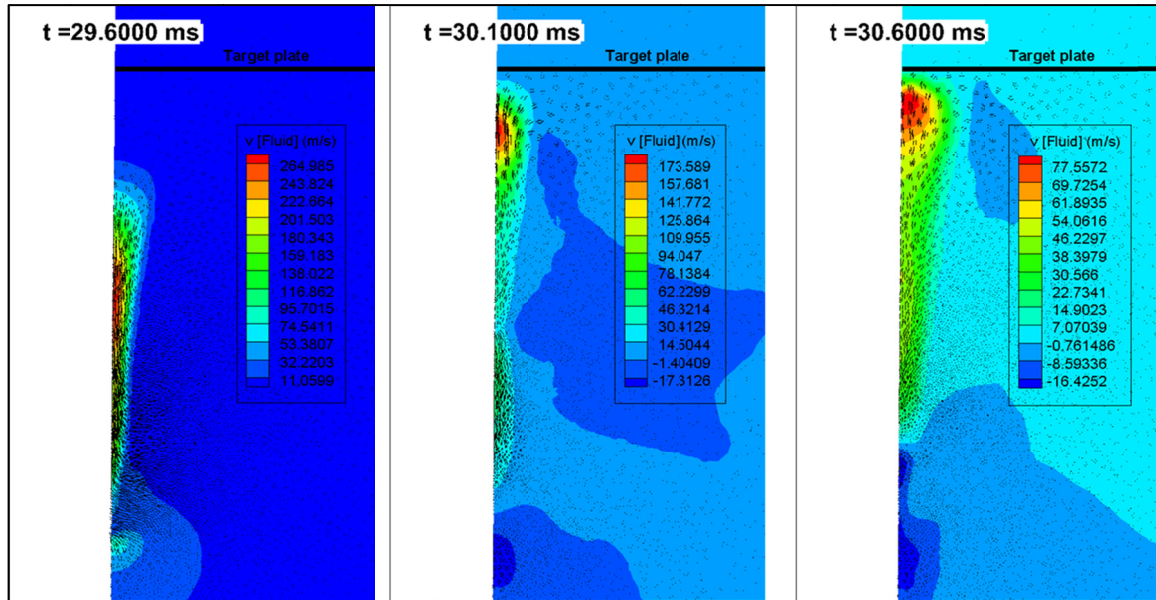
Figure 61: Formation of the water jet at first bubble collapse: rigid-free target.
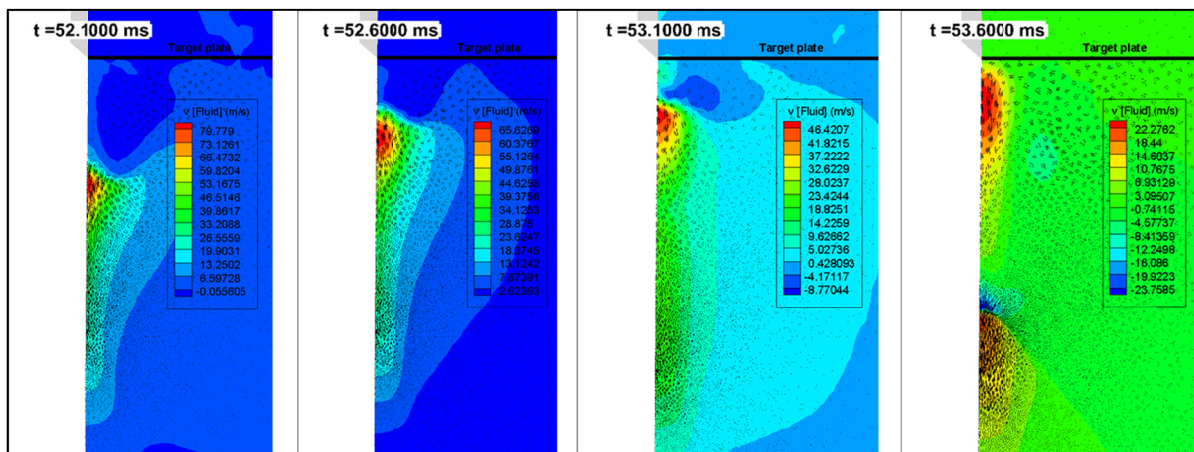
Figure 62: Formation of the water jet at second bubble collapse: rigid-free target.
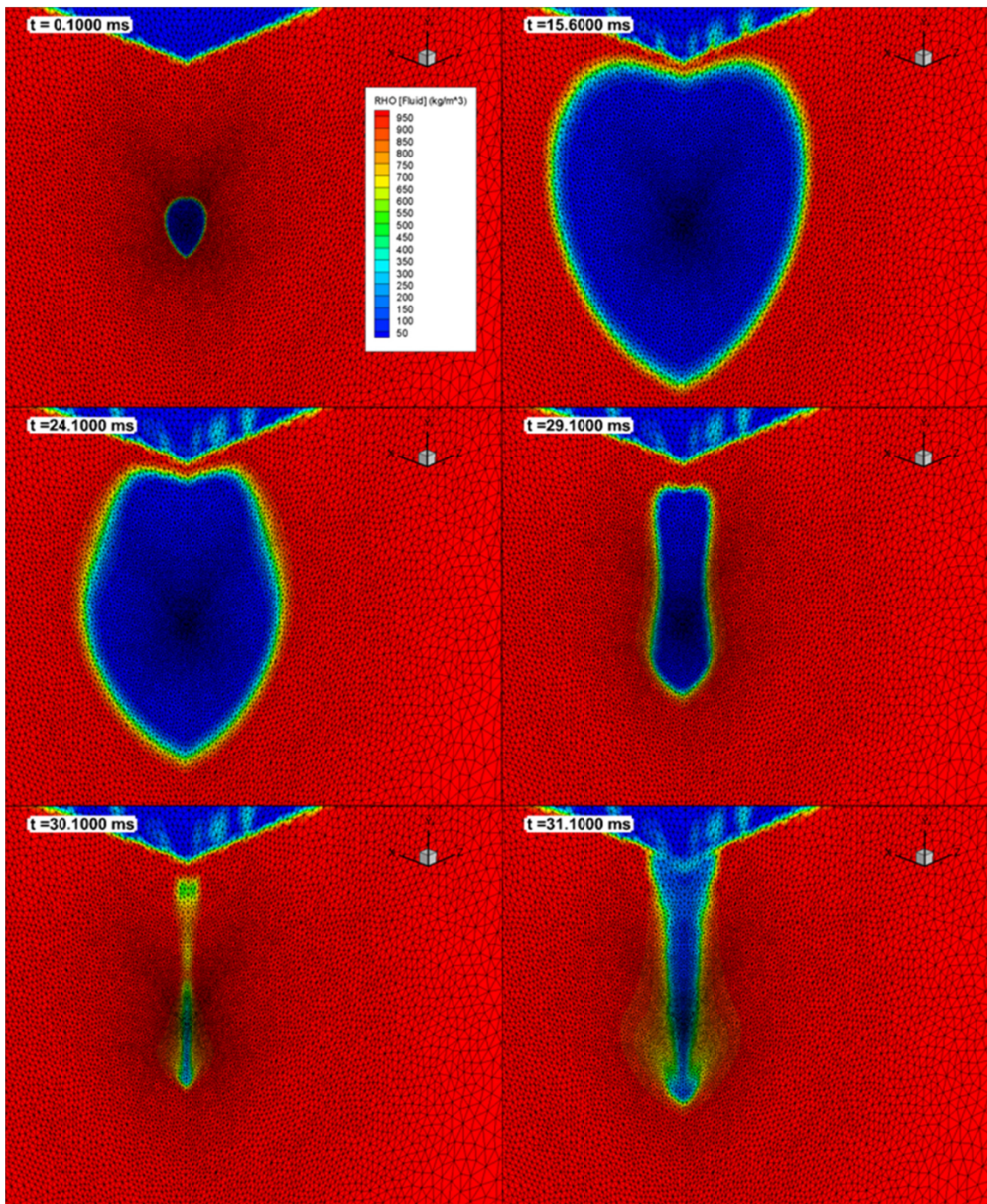
Figure 63: Progression of the gas bubble to first collapse: rigid-free target.
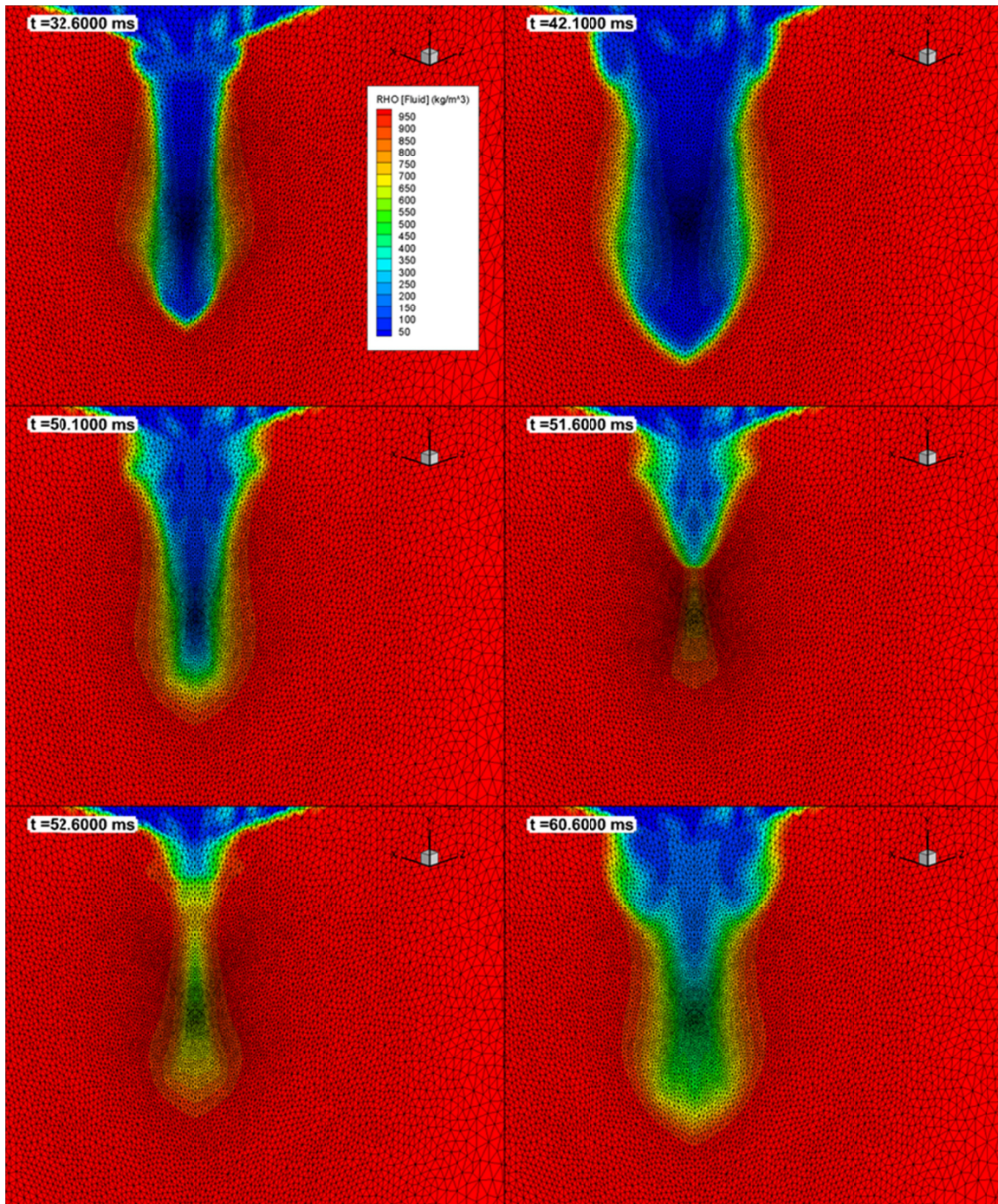
Figure 64: Progression of the gas bubble to second collapse and beyond: rigid-free target.

The displacement of the rigid-free target model is shown in Figure 65, in comparison to the target displacements in the 2D case. The differences between the 3D and 2D small deformation coupling cases are comparable to the differences between the two different coupling methods in 2D.
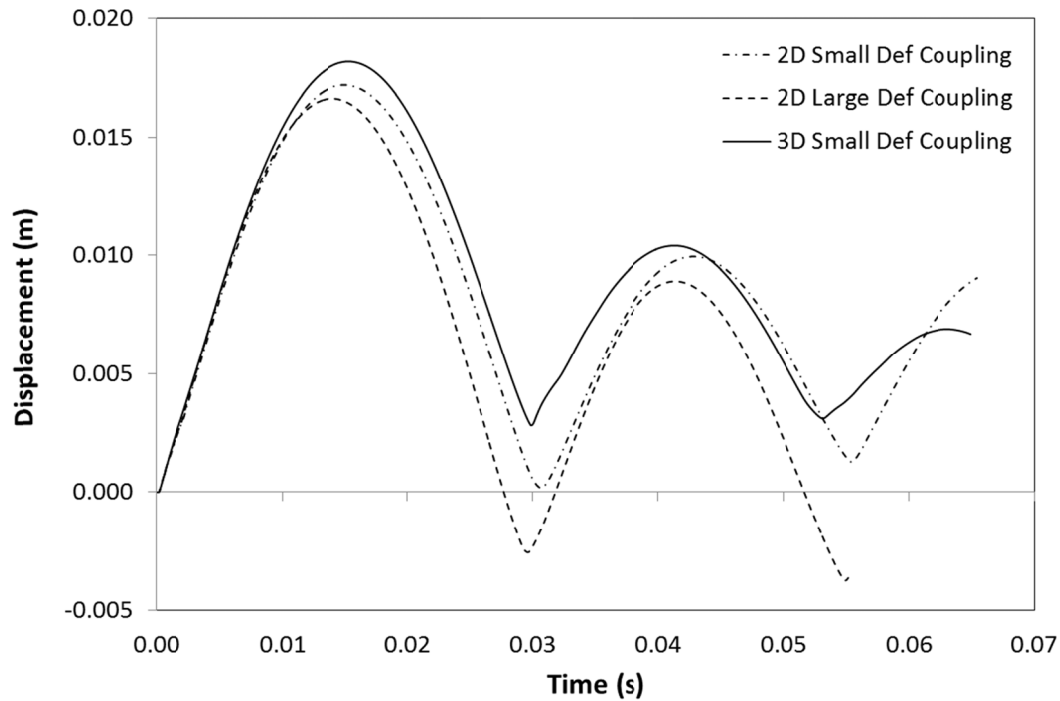
Figure 65: Displacement response rigid free target plates.

5.3.3 Fixed target model

The target model is identical to the one used in Section 4.3.3. The FS3-1 grid is used with properties identical to those used in previous analyses. The mapping is performed using field variables determined with the 2D FS1 grid at the mapping time of 0.1 ms. The 3D coupled simulation (with small deformation coupling) halted prematurely at 17.54 ms. The error message produced by Chinook was:

```
NAN for variable 0, at cell 23695 (6.563410e-03, 1.783827e-01, 5.398819e-02) on proc 11
```

The simulation ran long enough to determine the maximum bubble radius and its direction of collapse. The sequence of density contours in Figure 66 shows the bubble beginning to collapse downward, away from the target plate. The bubble reaches maximum expansion at about 9.6 ms, considerably earlier than in the rigid target cases, with an average radius of 0.156 m, or 88% of the empirical value.
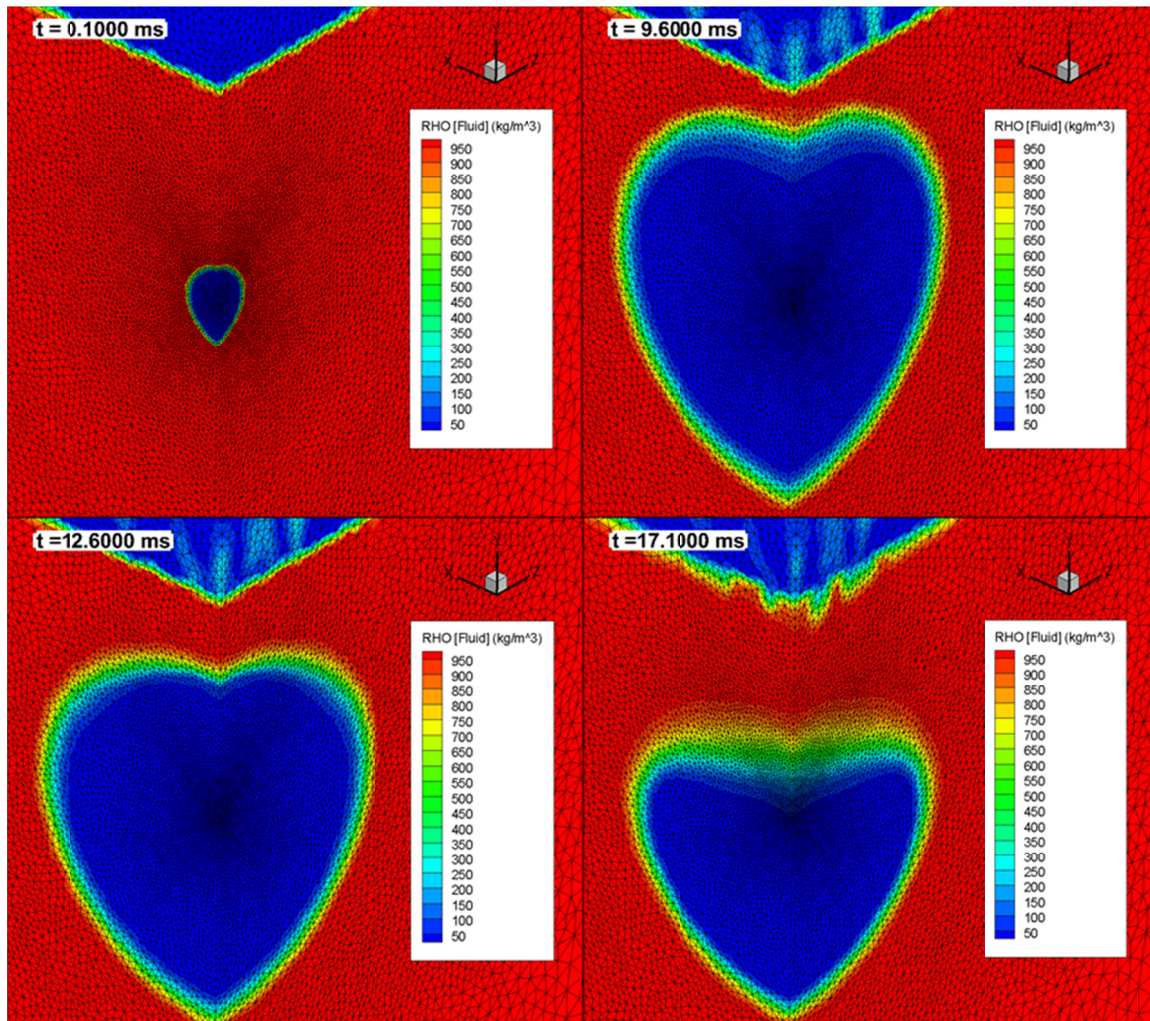
Figure 66: Progression of the gas bubble: fixed target.

The displacement at the centre of the plate is shown in Figure 67. During the initial shock response, the plate deforms upwards a maximum of 19 mm. As the gas bubble begins to collapse downward, after 10 ms, the plate deforms downward to a maximum of -20.6 mm. Shortly after reaching maximum downward deflection, the simulation fails. The displacement time history is very similar to that predicted with the 2D model up to about 10 ms; after this time, the rebound of the 3D model is delayed by about 1 ms in comparison to the 2D model.
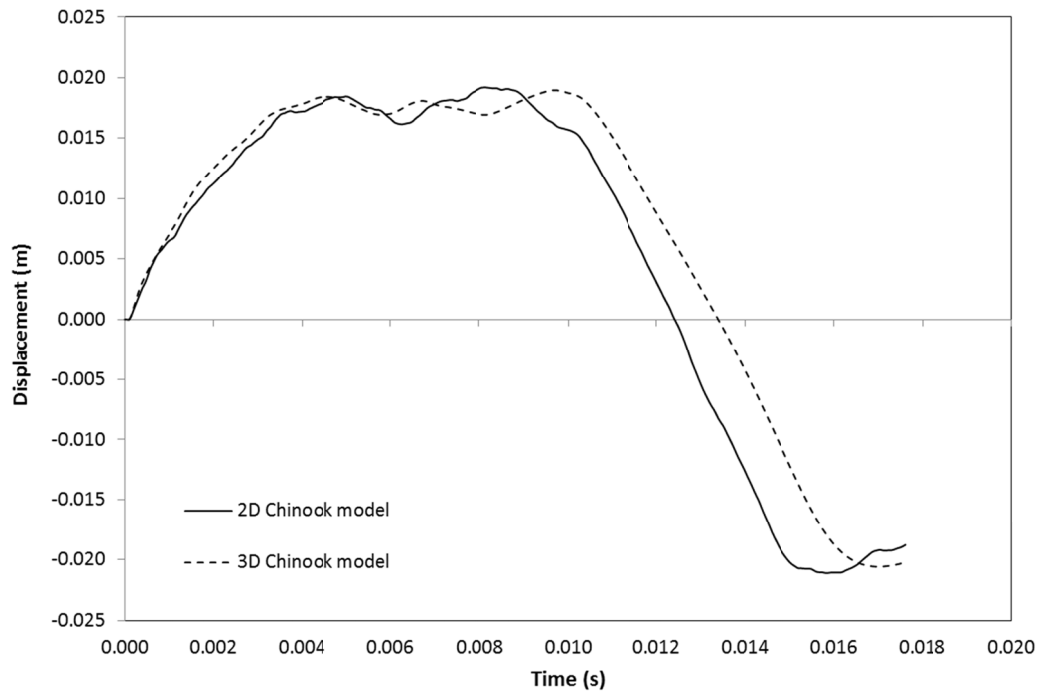
Figure 67: Comparison of displacement responses of the centre of the fixed target plate.

5.3.4   Free target model

The target model is identical to the one used in Section 4.3.4. The FS3-1 grid is used with properties identical to those used in previous analyses. The mapping is performed using field variables determined with the 2D FS1 grid at the mapping time of 0.1 ms. The 3D coupled simulation (with small deformation coupling) halted prematurely at 14.06 ms. The error message produced by Chinook was:

```
NAN for variable 0, at cell 12794 (7.489067e-03, 1.788903e-01, 1.405198e-02) on proc 11
```

The simulation ran long enough to determine the maximum bubble radius, and its direction of collapse. The progress of the bubble is similar to that which was seen in Figure 66 for the fixed target case. The bubble reaches maximum expansion at about 9.6 ms and begins to collapse downward, away from the target plate. The average radius at maximum expansion is 0.158 m, or 88% of the empirical value.

The displacement at the centre of the plate is shown in Figure 68. During the initial shock response, the plate deforms upwards a maximum of 18.3 mm, slightly more than that was is predicted with the 2D model. As the gas bubble begins to collapse downward, after 10 ms, the plate rebounds to nearly its original position, and then begins to increase again. The simulation fails about 2 ms after reaching its minimum displacement. The displacement time history is everywhere within 2 mm of that predicted with the 2D model.
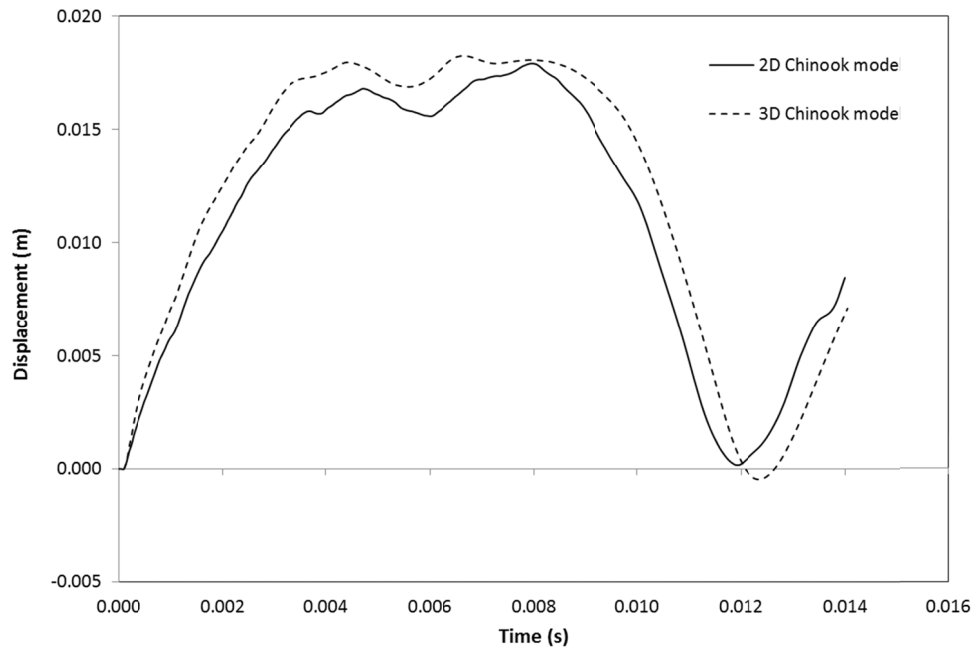
Figure 68: Comparison of displacement responses of the centre of the free target plate.

5.3.5 Large deformation coupling

The above 3D FSI simulations were all calculated using small deformation coupling between Chinook and LS-Dyna. Several attempts were made to perform the same simulations with large deformation coupling, but none were successful. In the three cases attempted, the simulations failed in the early stages (between 3 and 5 ms). Table 25 summarizes the run time and the error reported by Chinook for the rigid-free, fixed and free targets. These simulations were run on a Dell multicore server with 200 cores. The rigid-fixed case with large deformation coupling is numerically identical to the small deformation case, and therefore produces the same results as those shown in Section 5.3.1.

Table 25: Summary of 3D FSI simulations with large deformation coupling.

Case	Termination time (ms)	Chinook error message
Rigid-free	4.700	NAN for variable 0, at cell 738 (2.904874e-01, 1.961450e-01, 4.047117e-03) on proc 45
Fixed	3.165	NAN for variable 0, at cell 2747 (1.670993e-01, 1.935781e-01, 3.184154e-01) on proc 42
Free	3.173	NAN for variable 0, at cell 3118 (1.721734e-01, 1.842400e-01, 3.105358e-01) on proc 42

5.3.6   Summary

Table 26 summarizes the first bubble pulse radius and period results in four 3D FSI simulations. As in the 2D FSI simulations, there is a marked degradation in the quality of the bubble radius predictions in comparison to what was predicted in the free-field and free-surface simulations. Variability in the bubble period was also seen in the FSI simulations, but results could only be obtained for the rigid-fixed and rigid-free cases. As in the 2D FSI simulations, the behaviour of the gas bubble overall seems to be very sensitive to the amount of restraint and rigidity of the target, since other modelling parameters among the various FSI simulations are identical.

Table 26: Summary of the properties of the first bubble pulse in 3D FSI simulations.

Case	Coupling	A_{1x} (m)	A_{1y} (m)	A_{1z} (m)	A_1/A_1^*	T_1 (ms)	T_1/T_1^*
Rigid-fixed	Small	0.1743	0.1576	0.1737	0.952	34.67	1.197
Rigid-free	Small	0.1769	0.1658	0.1764	0.977	29.87	1.036
Fixed	Small	0.1596	0.1498	0.1596	0.883	-	-
Free	Small	0.1690	0.1344	0.1695	0.890	-	-

6   Discussion

The benchmark simulations described in this report revealed a number of strengths and weaknesses of Chinook in application to underwater explosion simulations. Most of these have previously been observed in other simulations but have not been widely reported on.

In the 1D benchmark problems, it was noted that Chinook is very slow to converge as the cell size and grid expansion factor are reduced. Even with highly refined grids, the maximum bubble radius and bubble periods differ from empirical values by 3%. Much better convergence was observed with 2D and 3D free-field simulations, which suggests a more fundamental deficiency in the 1D modelling. This could be related to the internal, structured gridding method used in Chinook (only used in this study for 1D simulations), or it could be related to the way spherical symmetry is implemented in Chinook.

The 2D free field simulations gave bubble radius and period predictions for the first bubble pulse that agree well with empirical values, and which show that these fundamental characteristics of the bubble are relatively insensitive to coarsening of the grid. Even quite coarse grids produced acceptable results, which was not the case in the 1D simulations. Coarse grids, such as the FF4 grid, are not suitable for predicting shock wave propagation, and much finer grids may be needed in simulations when shock and bubble effects are of interest.

The 2D free surface simulations showed similar bubble radius predictions, and bubble periods agreed very well with Snay's empirical formula including the surface correction factor. In these simulations, bubble jetting consistently occurred in a downward direction, which is consistent with numerous experimental observations.

Results for the second pulse showed much more significant discrepancies between predicted and empirical values. This is to be expected given that Chinook is based on an inviscid formulation of the Navier-Stokes equations. The only mechanisms for energy losses in Chinook are therefore the acoustic pulse emitted at the moment of collapse, and numerical losses due to the coarseness of the grid. Additional dissipative energy losses associated with the high fluid velocities and turbulence and heat transfer to the fluid during each collapse are not accounted for the Eulerian formulation used in Chinook.

In the 2D FSI simulations, some numerical problems were encountered with Chinook. With small deformation coupling, the simulations could in all cases be run until well passed the first bubble collapse. However, with large deformation coupling, only the simulations with rigid targets ran for sufficiently long duration to determine the bubble behaviour. With flexible targets, the simulations failed due to numerical overflow shortly after the target plate rebounds from its initial shock deflection. With small deformation coupling, the gas bubble was predicted to collapse and jet toward the target when the target is rigid; however, the bubble is predicted to jet downward, away from the target when the target is flexible.

Contrary to the flexible target predictions, experiments involving flexible targets of similar size and with similar charge size and standoff, exhibit bubble jetting toward the target. It is as though with a flexible target, the target acts on the bubble more as a free surface than as a rigid body. The

influence of the flexibility of the target on the predicted bubble behaviour is a question that needs to be explored further.

The 3D free field and free surface simulations gave similar results to the 2D axisymmetric cases. Most of the 3D simulations were performed by mapping the results from a 2D simulation in the early stages of the simulation, and this was found to give good results. Overall, some degradation in the bubble radius and period was seen when mapping is performed very early in the development of the bubble (0.1 ms).

In the 3D FSI simulations, only small deformation coupling cases could run successfully. Of these, only the two rigid target cases ran to completion; the simulations of the flexible target cases failed after the target plates has recovered from the initial deflection response due to the shock wave. Significant degradation in the bubble size was noted in all of the 3D FSI cases. These simulations all involved mapping from 2D to 3D at 0.1 ms.

Overall, it is recommended that 1D modelling methods not be used for UNDEX simulations, because of the poor convergence seen in these benchmark cases. It is recommended that 2D axisymmetric simulations with unstructured grids be used wherever practicable (i.e., when targets are axisymmetric), and that these simulations be run from time of detonation (i.e., without mapping from 1D). When targets are not axisymmetric, it is necessary to use 3D simulations. But at this point, Chinook coupled with LS-Dyna does not appear to be a reliable tool for 3D FSI simulations.

7   Conclusion

The results of a series of benchmark simulations of simplified underwater explosion scenarios have been presented with attention focussed on the behaviour of the explosion gas bubble. Simulations were conducted using the Chinook software (version 195) using one, two and three dimensional models. Fluid-structure interaction simulations were conducted for underwater explosions near a circular target plate using Chinook coupled with the LS-Dyna FEM software. The overall intent of the simulations was to (1) determine grid cell sizes needed to give accurate radius and period data for the explosion gas bubble; (2) identify modelling deficiencies in Chinook through comparison of results over a range of similar problems with identical material and modelling parameters; and (3) to establish a series of standard problems for benchmarking future versions of Chinook.

The results revealed that very fine grids are needed in 1D simulations to get acceptable gas bubble radius and period data, and that a 3% error is the best agreement that can be achieved with extremely refined 1D grids. The 2D and 3D free-field and free-surface simulations showed that a grid cell size of 8 mm was usually sufficient to give results for the first-pulse radius and period that are within 2% of the empirical values. Although some of this discrepancy may be attributable to inaccuracy in the empirical constants, the better agreement and faster convergence achieved in the 2D and 3D simulations strongly suggests that some underlying deficiency in the 1D modelling. Further work is needed to determine the accuracy of the empirical constants for he RP-83 detonators.

An 8 mm cell size may not be sufficient when a shock wave must be propagated across some part of the grid. Finer grids will likely have to be used in this case. Also, when mapping is used in 3D models, it may be necessary to use smaller cell sizes to ensure that the initial energy in the gas bubble is modelled with sufficient resolution at the time of mapping.

The FSI simulations revealed some numerical issues with Chinook that will have to be resolved in future releases. Many of the premature terminations of Chinook are believed to be caused by the non-convergence of an iterative method for determining the material density fractions in mixed material cells. A possible solution to this problem is to implement a more deterministic scheme better suited to UNDEX problems.

Furthermore, the gas bubble behaviour predicted by Chinook appears to be highly sensitive to the degree of restraint and flexibility of the target structure. In particular, the predicted gas bubble jetting behaviour was very different for rigid and flexible models. For flexible models, the gas bubble appears to behave like a gas bubble next to a free surface. This may be caused by Chinook overestimating or incorrectly predicting the cavitation that occurs next to a responding plate. This question requires further exploration.

References

[1] Webster, K. (2007), *Investigation of Close Proximity Underwater Explosion Effects on a Ship-Like Structure Using the Multi-Material Arbitrary Lagrangian Eulerian Finite Element Method*. Master of Science thesis. Virginia Polytechnic Institute and State University, Blacksburg, VA.

[2] Yoon, D., Park, J., Eccles, T., Powell, A., Manley, D. and Widholm, A. (2010), *Joint Investigation Report On the Attack Against ROK Ship Cheonan*, Ministry of National Defence. Republic of Korea.

[3] Mader, C. (1972), Detonations near the Water Surface. Report LA-4958, Los Alamos Scientific Laboratory, Los Alamos, NM.

[4] Mair, H. (1995), Hydrocode Methodologies for Underwater Explosion Structure/Medium Interaction, *Proceedings of the 66th Shock and Vibration Symposium*, Vol II, SAVIAC, 227–248.

[5] Blake, J., Taib, B., Doherty, G. (1986), Transient Cavities Near Boundaries. Part I. Rigid Boundary, *Journal of Fluid Mechanics*, 170, 479–497.

[6] Best, J. (1993), The formation of toroidal bubbles upon the collapse of transient cavities, *Journal of Fluid Mechanics*, 251, 79–107.

[7] Link, R., Lin, F., Whitehouse, D. and Slater, J. (2002), CFD Modeling of Close Proximity Underwater Explosions, *Proceedings of the 73rd Shock and Vibration Symposium*, Newport, USA.

[8] Dunbar, T. (2009). Modelling of Close-Proximity Underwater Explosion Loads and Structural Response – Phase 1. DRDC Atlantic CR 2008-272, Martec Limited, Halifax, Canada.

[9] Riley, M. (2010), Modeling Gas Bubble Behaviour and Loading on a Rigid Target due to Close-Proximity Underwater Explosions. DRDC Atlantic TM 2010-238, Defence R&D Canada – Atlantic.

[10] Riley, M., Smith, M., van Aanhold, J. and Alin, N. (2012), Loading on a Rigid Target from Close Proximity Underwater Explosions. *Shock and Vibration*, 19 (4), 555–571.

[11] Link, R., Ripley, R., Norwood, M., Josey, T., Donahue, L. and Slater, J., (2003), Analysis of the Loading and Response of Flat Plate Targets Subjected to Close-Proximity Underwater Explosions, *Proceedings of the 74th Shock and Vibration Symposium*, San Diego, CA.

[12] Gregson, J., Link, R. and Lee, J. (2006), Coupled Simulation of the Response of Targets to Close Proximity Underwater Explosions in Two and Three Dimensions, *Proceedings of the 77th Shock and Vibration Symposium*, Monterey, USA.

[13] Dunbar, T. (2009). Modelling of Close-Proximity Underwater Explosion Loads and Structural Response – Phase 2. DRDC Atlantic CR 2008-272, Martec Limited, Halifax, Canada.

[14] Lee, J., Smith, M., Huang, J. and Paulgaard, G. (2008), Deformation and Rupture of Thin Steel Plates Due to Cumulative Loading from Underwater Shock and Bubble Collapse, *Proceedings of the 79th Shock and Vibration Symposium*, Orlando, USA.

[15] Lee, J., Smith, M., Roseveare, D. and Paulgaard, G. (2014). 3D Image Correlation Measurements on a Floating Panel Loaded by an Underwater Explosion, *Presented at the 85th Shock & Vibration Symposium*, Reston, USA.

[16] Smith, M. and Lee, J. (2016), Coupled Eulerian-Lagrangian simulations of an underwater explosion near a floating target. In *Military Aspects of Blast and Shock (MABS24)*, 18–23 September 2016, Halifax, Canada

[17] Martec Limited (2015), ChinookEXP Input Manual, Martec software Manual #SM-13-04 Rev 11, ChinookEXP v195, Martec Limited, Halifax NS, Canada, 10 Feb 2015.

[18] Livermore Software Technology Corporation, (2012), LS-DYNA Keyword User's Manual, Version 971 R6.1.0, Livermore Software Technology Corporation, Livermore CA, August 2012.

[19] Keil, A.H. (1961), The Response of Ships to Underwater Explosions, David Taylor Model Basin Report 1576. Presented at the Annual Meeting of the Society of Naval Architects and Marine Engineers, New York, USA. ADA 268905.

[20] Menon, S. (1996), Experimental and Numerical Studies of Underwater Explosions, Georgia Institute of Technology report. ADA 317378.

[21] Snay, H.G. (1962), Underwater Explosion Phenomena: The Parameters of Migrating Bubbles, NAVORD Report 4185. US Naval Ordnance Laboratory, White Oak MD.

[22] Lee, E., Horning, H. and Kury, J. (1968), Adiabatic expansion of high explosives detonation products, Lawrence Livermore National Laboratory, University of California, Livermore, TID 4500-UCRL 50422.

[23] Jones, H. and Miller, A. (1948), The detonation of solid explosives, *Proceedings of the Royal Society of London*, A-194, 480.

[24] Wilkins, M. (1964), The equation of state of PBX 9404 and LX04-01, Report UCRL-7797, Lawrence Radiation Laboratory, Livermore.

[25] Li, Y. (1967), Equation of State of Water and Sea Water, *Journal of Geophysical Research*, 72(10), 2665–2678.

[26] Fried, L., Howard, W., Souers, P. and Vitello, P. Cheetah 3.0 User's Manual. Lawrence Livermore National Laboratory Report (2001).

[27] Pointwise (2015), Pointwise User Manual, Pointwise V17.3 Release 2, Pointwise Inc., Fort Worth, USA.

List of symbols/abbreviations/acronyms/initialisms

A, B, C	JWL coefficients
atm	Atmospheres
A_{nx}, A_{ny}, A_{nz}	Radius of the nth bubble pulse as measured along the x, y, z axis
A_n	Maximum radius of explosion gas bubble in the nth period or pulse
A_n^*	Maximum radius gas bubble radius (empirical value)
a_M	Dimensionless reduced radius
CFD	Computational fluid dynamics
c	Speed of sound in water
d	Charge depth
d_n	Depth of gas bubble during n^{th} period or pulse
DRDC	Defence Research and Development Canada
E	Elastic modulus
FEM	Finite element method
FSI	Fluid-structure interaction
g	gram
g	Acceleration of gravity
GPa	Gigapascals
h_1, h_2, h_3, h_4	Grid cell size parameters
HLLC	Harten-Lax-van Leer-Contact (solver)
J	Joules
JWL	Jones-Wilkins-Lee (equation of state)
K	Kelvin
K_5, K_6	Empirical constants
kg	kilograms
m	Metres
mm	Millimetres
MOU	Memorandum of Understanding
ms	Milliseconds
N	Number of grid cells in regular grid
N_E	Number of cells in extended grid

P	Pressure
P_{atm}	Atmospheric pressure
P_h	Hydrostatic pressure
P_{tot}	Total pressure
P_0	Peak pressure
Pa	Pascal
Q	Explosive energy per unit mass
R	Radial distance
R_m	Distance to monitor point location
r_n	Fraction of explosive energy in the nth bubble pulse
R_1, R_2	JWL equation coefficients
RDX	Research Department explosive (nitroamine)
ROKS	Republic of Korea Ship
R&D	Research & Development
s	Seconds
SI	Système International
t	time
T_c	Time to peak pressure
T_n	Bubble period of the nth period or pulse
T_n^*	Bubble period of the nth period or pulse (empirical value)
UNDEX	Underwater explosion
v	Specific volume
W	Charge weight
x, y, z	Cartesian coordinates
X, Y, Z	Cartesian coordinates
X_E	Extended grid dimension
X_R	Regular grid dimension
Z_n	Hydrostatic water head in the nth bubble period
1D	One-dimensional
2D	Two-dimensional
3D	Three-dimensional
α	Surface correction factor

α_c	Cavitation pressure fraction
ΔX_E	Extended grid cell size
ΔX_R	Regular grid cell size
ξ	Cell size expansion factor
µs	Micro-seconds
ν	Poisson ratio
ρ	Density
τ	Reduced time
ω	JWL equation coefficient

This page intentionally left blank.

DOCUMENT CONTROL DATA

(Security markings for the title, abstract and indexing annotation must be entered when the document is Classified or Designated)

1. ORIGINATOR (The name and address of the organization preparing the document. Organizations for whom the document was prepared, e.g., Centre sponsoring a contractor's report, or tasking agency, are entered in Section 8.) DRDC – Atlantic Research Centre Defence Research and Development Canada 9 Grove Street P.O. Box 1012 Dartmouth, Nova Scotia B2Y 3Z7 Canada	2a. SECURITY MARKING (Overall security marking of the document including special supplemental markings if applicable.) UNCLASSIFIED
	2b. CONTROLLED GOODS (NON-CONTROLLED GOODS) DMC A REVIEW: GCEC DECEMBER 2013

3. TITLE (The complete document title as indicated on the title page. Its classification should be indicated by the appropriate abbreviation (S, C or U) in parentheses after the title.)

Benchmark simulations of underwater explosion gas bubble dynamics and interactions

4. AUTHORS (last name, followed by initials – ranks, titles, etc., not to be used)

Smith, M.J.

5. DATE OF PUBLICATION (Month and year of publication of document.) September 2016	6a. NO. OF PAGES (Total containing information, including Annexes, Appendices, etc.) 88	6b. NO. OF REFS (Total cited in document.) 27

7. DESCRIPTIVE NOTES (The category of the document, e.g., technical report, technical note or memorandum. If appropriate, enter the type of report, e.g., interim, progress, summary, annual or final. Give the inclusive dates when a specific reporting period is covered.)

Scientific Report

8. SPONSORING ACTIVITY (The name of the department project office or laboratory sponsoring the research and development – include address.)

DRDC – Atlantic Research Centre
Defence Research and Development Canada
9 Grove Street
P.O. Box 1012
Dartmouth, Nova Scotia B2Y 3Z7
Canada

9a. PROJECT OR GRANT NO. (If appropriate, the applicable research and development project or grant number under which the document was written. Please specify whether project or grant.) 01EA (Fleet Transformation)	9b. CONTRACT NO. (If appropriate, the applicable number under which the document was written.)
10a. ORIGINATOR'S DOCUMENT NUMBER (The official document number by which the document is identified by the originating activity. This number must be unique to this document.) DRDC-RDDC-2016-R171	10b. OTHER DOCUMENT NO(s). (Any other numbers which may be assigned this document either by the originator or by the sponsor.)

11. DOCUMENT AVAILABILITY (Any limitations on further dissemination of the document, other than those imposed by security classification.)

Unlimited

12. DOCUMENT ANNOUNCEMENT (Any limitation to the bibliographic announcement of this document. This will normally correspond to the Document Availability (11). However, where further distribution (beyond the audience specified in (11) is possible, a wider announcement audience may be selected.))

Unlimited

13. ABSTRACT (A brief and factual summary of the document. It may also appear elsewhere in the body of the document itself. It is highly desirable that the abstract of classified documents be unclassified. Each paragraph of the abstract shall begin with an indication of the security classification of the information in the paragraph (unless the document itself is unclassified) represented as (S), (C), (R), or (U). It is not necessary to include here abstracts in both official languages unless the text is bilingual.)

The results of a series of benchmark simulations in one, two and three dimensions are presented to illustrate the capabilities of the Eulerian blast code Chinook (version 195) in simplified underwater explosion (UNDEX) scenarios. Attention in this study is focussed on the behaviour of the underwater explosion gas bubble. 2D and 3D simulation results for a 1.1 g charge detonated in the free field agree well with empirical formulas for gas bubble radius and period for the first bubble pulse, whereas 1D simulation results fall short of the expected accuracy. Results for UNDEX near a free surface also agree well with empirical formulas in 2D and 3D, and realistic gas bubble jetting behaviour is predicted. Fluid-structure interaction simulations with a circular-plate target structure were simulated using Chinook coupled with the finite element program LS-Dyna. The predicted gas bubble behaviour is realistic for rigid target models, but unrealistic when the target plate is flexible. Of the two different coupling schemes used, Chinook's small deformation coupling scheme was more reliable; the large deformation coupling scheme worked consistently with rigid target models in 2D, but is prone to numerical problems in 3D.

On présente les résultats d'une série de simulations de référence unidimensionnelles (1D), bidimensionnelles (2D) et tridimensionnelles (3D) afin d'illustrer les capacités du logiciel eulérien Chinook pour la simulation d'explosions (version 195) dans des scénarios simplifiés d'explosions sous-marines (UNDEX). Dans la présente étude, on accorde une attention particulière au comportement de la bulle de gaz créée par une explosion sous-marine. Les résultats des simulations 2D et 3D pour une charge de 1,1 g qui explose en champ libre concordent avec les formules empiriques pour le rayon de la bulle de gaz et la période de la première impulsion de la bulle. Les résultats des simulations 1D sont toutefois inférieurs à l'exactitude prévue. Les résultats des UNDEX près d'une surface libre concordent également avec les formules empiriques en 2D et 3D, ce qui permet de prévoir le comportement réaliste de jets de bulles de gaz. Pour les simulations d'interaction fluide-structure à l'aide d'une structure cible, laquelle consiste en une plaque circulaire, le logiciel Chinook a été utilisé et jumelé au programme de calcul par éléments finis LS-Dyna. Le comportement prévu des bulles de gaz est réaliste pour les modèles de cibles rigides, mais irréaliste quand la plaque cible est flexible. De ces deux méthodes, le couplage des déformations légères de Chinook a offert la plus grande fiabilité; le couplage des déformations importantes a fonctionné de façon constante avec les modèles de cibles rigides en 2D, mais avait tendance à éprouver des problèmes numériques en 3D

14. KEYWORDS, DESCRIPTORS or IDENTIFIERS (Technically meaningful terms or short phrases that characterize a document and could be helpful in cataloguing the document. They should be selected so that no security classification is required. Identifiers, such as equipment model designation, trade name, military project code name, geographic location may also be included. If possible keywords should be selected from a published thesaurus, e.g., Thesaurus of Engineering and Scientific Terms (TEST) and that thesaurus identified. If it is not possible to select indexing terms which are Unclassified, the classification of each should be indicated as with the title.)

Underwater explosion; fluid-structure interaction; gas bubble; bubble collapse; water jet; computational fluid dynamics